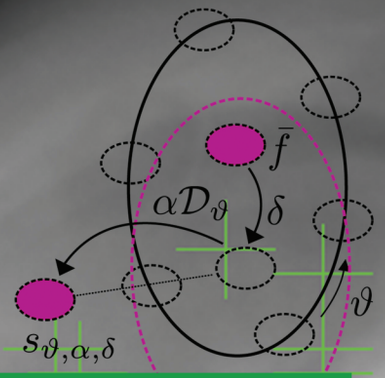

Lung cancer is the most common cause of cancer death in the world, and radiation therapy is the primary treatment modality for patients with inoperable lung cancer. Organs in the thoracic and abdominal region can move considerably due to breathing, influencing the accuracy of imaging, treatment planning, and treatment delivery. Recent developments have made respiratory-correlated and in-room imaging available for planning and image-guidance. These techniques can provide timely, patient-specific information on the motion of organs and tumours, and reduce the geometric uncertainties associated with the treatment.

The goal of this work was to improve the characterization, quantification and representation of lung motion and facilitate its inclusion into the radiation therapy treatment process. Using respiratory-correlated planning images, a patient-specific motion model was constructed in which variations taking place at different time-scales were accounted for separately. A low-dimensional parametrization was pursued by tuning both the spatial and temporal representation of the occurring deformations, and by considering the physiology of the motion. By fitting the obtained motion model to in-room images, intrafraction motion estimation can be accomplished.

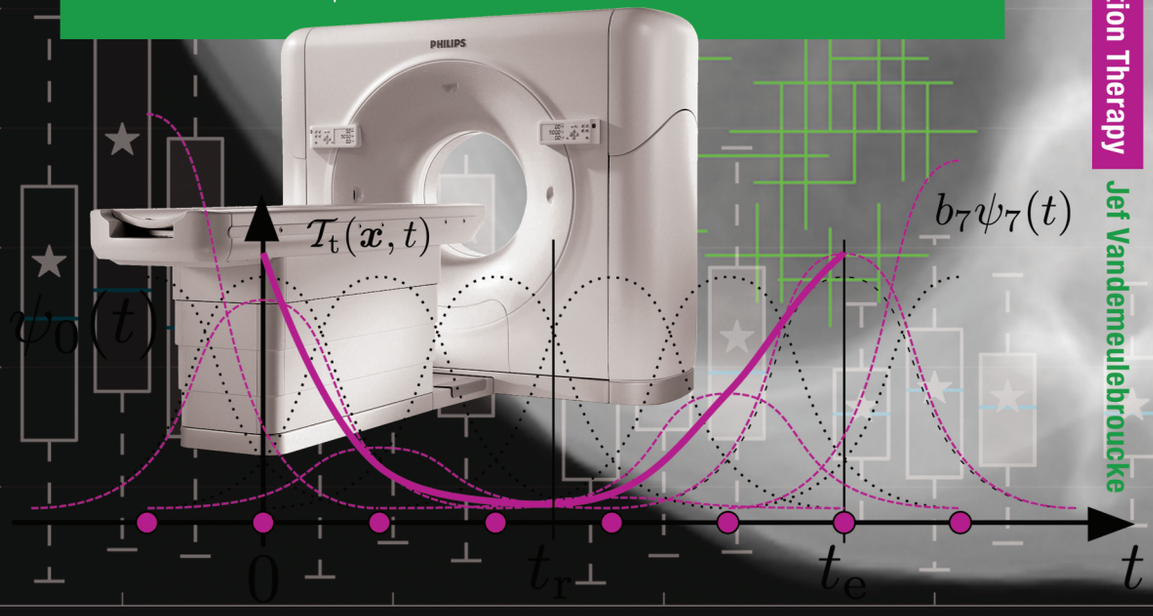

Lung Motion Modelling and Estimation afor Image Guided Radiation Therapy

Jef Vandemeulebroucke

Jef Vandemeulebroucke

Lung Motion Modelling and Estimation for Image Guided Radiation Therapy

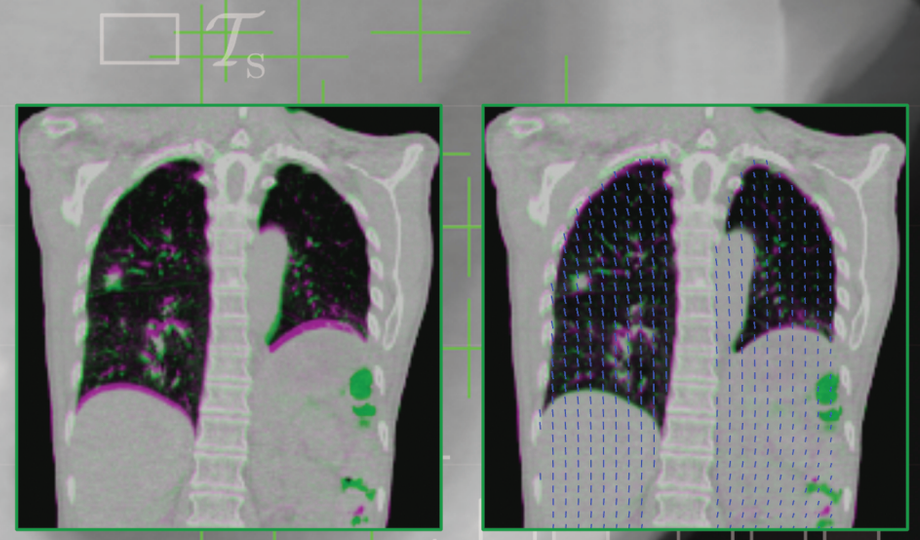

Numéro d'ordre : 2010-ISAL-0051 Année 2010

THÈSE

présentée devant

L'Institut National des Sciences Appliquées de Lyon

pour obtenir

LE GRADE DE DOCTEUR

ÉCOLE DOCTORALE : ÉLECTRONIQUE, ÉLECTROTECHNIQUE, AUTOMATIQUE
FORMATION DOCTORALE : IMAGES ET SYSTÈMES

par

Jef Vandemeulebroucke
Ingénieur de l'Université de Gand

Lung Motion Modelling and Estimation for Image Guided Radiation Therapy

Modélisation et Estimation du Mouvement Pulmonaire pour la Radiothérapie Guidée par l'Image

soutenue le

16 Juillet 2010

Jury

David Hawkes	Professeur, UCL, Londres	*Rapporteur*
Dirk Vandermeulen	Professeur, KUL, Louvain	*Rapporteur*
Grégoire Malandain	Directeur de Recherche, INRIA	*Examinateur*
Denis Friboulet	Professeur, INSA, Lyon	*Examinateur*
Jan Kybic	Chargé de Recherche, CVUT, Prague	*Co-directeur de thèse*
David Sarrut	Chargé de Recherche, CNRS	*Co-directeur de thèse*
Patrick Clarysse	Chargé de Recherche, CNRS	*Co-directeur de thèse*

Invité

Claude Malet Physicien Médical, CLB, Lyon

Acknowledgements

Even though I probably never spent quite as much time alone behind my computer as I did during the last three years, it would be wrong to consider this book the work of an individual. I found that research, especially in medical image processing, greatly benefits from strong interaction with a multidisciplinary research team, and I would not be exaggerating in stating that this work would never have been realized without the help of numerous others.

I would like to thank *David Sarrut*, my closest supervisor and mentor, for giving me the opportunity to work on this exciting subject. His energy and enthusiasm were a constant motivation over the years and an inspiration for my future career. He provided me with an exceptional multidisciplinary research environment at the Centre Léon Bérard (CLB) in which informaticians, engineers, physicists and physicians cooperate, and which I considered an advantage and a privilege to work in. Thank you for giving me the freedom to explore the area and pursue my own objectives–but also, for helping me prioritize and focus when necessary, which was often the case. Our many pleasant and fruitful brainstorming sessions are amongst the things I will miss most about my time in Lyon.

I was fortunate to spend several months at the Center for Machine Perception (CMP) in Prague, where I worked under the supervision of *Jan Kybic*. I appreciated his alternative, methodological point of view on things and strong scientific rigour, and feel it strongly influenced my work. From a distance, he helped me enormously by thoroughly proofreading my papers and structuring my experiments with concise scientific wordings.

The ideal person to complete my supervision team was *Patrick Clarysse*, head of the Dynamic Imaging Group at Creatis, and my principal supervisor. Through his group meetings and presentations he provided me with a broader view of the medical imaging area in which to place my own ideas. His vast knowledge and experience of the field proved valuable

assets, often allowing him to point me to interesting related concepts.

I would like to express my gratitude to *Jean-Louis Sourouille*, coordinator of the EU Marie Curie WARTHE project in which I was granted a fellowship, for the enormous effort he put into organizing meetings, workshops and summer schools. These events, and the interaction that followed from it, added an international and privileged feeling to the project, and made it so much more pleasant. I would also like to acknowledge *Vaclav Hlavac*, head of CMP, for welcoming me at CMP as one of his own and making me feel right at home.

When starting my research, I was fortunate to have predecessors who had laid the ground in my topic. *Vlad Boldea* and *Bertrand Delhay* helped me tremendously by sharing their findings on motion modelling and image registration, and were excellent tutors during my first experiments.

I am particularly grateful to *Simon Rit*, colleague, collaborator and my closest coach during the last year. Our many inspiring discussions influenced my approach substantially. I value his views on lung motion modelling, and his contributions improved the quality of my work considerably. His unconditional support during the final months was invaluable for concluding this project. I am confident he will make a great researcher and supervisor.

I very much enjoyed collaborating with *Olivier Bernard*, who guided me through the world of image segmentation, and I greatly appreciated his patience and creative input during our meetings. The person I could always turn to for help was *Joel Schaerer*, whether it concerned mathematical derivations, Linux, C++ programming or even fundamental physics. Coffee break discussions wouldn't have been the same without him. In addition, I would like to thank all my colleagues at the CLB for their contributions, and for making my days so enjoyable, in particular *Louise Grezes-Besset*, *Nabil Zahra*, *Thibault Frisson* and *Gauthier Bouilhol*.

Thank you also *Jamie McClelland*, from the UCL in London, for sharing your experiences with motion modelling and Vision RT. Similarly, thank you *Jochem Wolthaus* from the NKI in Amsterdam for your openness and for your much valued feedback on my projects.

I am very grateful to *Chantal Ginestet*, head of medical physics at the CLB, for welcoming me in the department, and to all physicists for their help and for kindly adapting their activities to accommodate mine. A special thanks goes to *Myriam Ayadi* for enlightening me about the current practice in radiotherapy during initial collaborations, but especially, for being my contact inside the clinic and rapidly responding to my numerous demands. In addition, the contributions of *Line Claude* and *Bertrand*

Fleury, radiotherapists at CLB, were very much appreciated.

To conclude, I would like to thank my amazing family, my parents *Pol* and *Annemie* and sisters *Martje* and *An*, for their continuous support over the years. Your faith in my abilities strengthened me when needed, and made the difference at important moments.

But my final words go to my girlfriend, *Marie-Odette*, who agreed to undertake this adventure with me. Thank you for providing me with much appreciated distraction when required and for giving me the confidence to push through when necessary. Most of all, thank you for putting up with me during all this time, much of which I imagine was...challenging. I simply couldn't have done this without you.

July 2010
Jef

Summary

Respiratory motion introduces uncertainties in radiation therapy for lung cancer treatment. The principal aim of this work is to provide methodological contributions for the quantification, characterization and representation of lung motion, in order to facilitate its inclusion in the radiotherapy treatment process.

Recent developments have led to the routine acquisition of four-dimensional computed tomography (4D CT) and cone-beam computed tomography (CBCT) for the planning and delivery of certain treatment strategies. The availability of these images over the course of treatment make them particularly suited for providing patient-specific motion information and deriving motion models. B-splines were chosen for representing the motion, because of their flexibility and computational efficiency.

A first part of our contributions concerns the quantification of lung motion from 4D CT through deformable registration. We describe a method for automatically extracting a motion mask, which divides the thorax into moving and less-moving regions. By providing an interface where sliding motion occurs, the discontinuity in the motion fields is preserved and registration is facilitated. Stronger smoothness constraints can be applied for each region separately while maintaining matching accuracy.

Next, a spatio-temporal registration framework for respiratory-correlated imaging of the lungs is developed. A spatial transformation based on B-splines is extended to the temporal domain by coupling it to a cyclic trajectory model with suitable smoothness constraints. The obtained deformation model is shown to be capable of accurately representing respiratory motion while using a more compact and restrictive parametrization. By enforcing the temporal coherence of the deformation across the breathing cycle, robustness to artifacts of subsequent deformable registration is improved.

As an application, we investigated the feasibility of performing respiratory motion estimation from a cone-beam projection sequence. A strong prior about the patient's breathing pattern is introduced in the form of a patient-specific model built from a previously acquired 4D CT image. Motion estimation is accomplished by comparing the cone-beam projection sequence to projection views of the patient model. A semi-global optimization approach is utilized, considering the entire breathing cycle and providing smooth motion estimates per cycle.

Finally, we describe our initial efforts to provide an intrafractional estimate of an average lung deformation for monitoring baseline variations during treatment delivery. The method consists in comparing a prior patient image to multiple projections acquired in the treatment room. Similarity is measured in the projection space and an efficient algorithm is proposed to integrate the information obtained from the different projection views. By introducing physiological priors, the dimensionality of the deformable registration problem is greatly reduced.

Sommaire

Cette thèse aborde la problématique du mouvement respiratoire dans le contexte du traitement du cancer du poumon par radiothérapie. Notre travail vise à fournir des contributions méthodologiques pour la quantification, charactérisation et la représentation du mouvement du poumon par imagerie, afin de faciliter son intégration dans le processus de traitement.

Les récentes avancées technologiques ont conduit à l'utilisation régulières d'images tomodensitométriques 4D (4D CT) et issues de tomographes à géométrie conique (CBCT) pour la planification et la réalisation de certaines modalités de traitements. La disponibilité de ces images les rends particulièrement adaptées pour fournir des information de mouvement spécifique à chaque patient. Nous les avons choisies comme base pour la construction de modèles de mouvement respiratoire.

Nos premières contributions concernent la quantification du mouvement sur des images 4D CT par recalage déformable. Nous décrivons une méthode originale permettant l'extraction automatique d'un masque de mouvement qui sépare le thorax en régions mobiles et moins mobiles. En fournissant une interface oú des mouvements glissants ont lieux, notre approche permet de préserver les discontinuités dans les champs de mouvement, ce qui facilite le recalage. Des contraintes plus fortes peuvent ainsi être imposées pour chaque région, tout en maintenant la précision de l'appariement.

Ensuite, nous développons une méthodologie de recalage spatio-temporel pour l'imagerie corrélée à la respiration. Un modèle de déformation spatiale basée sur des B-splines est étendu au domaine temporel en le couplant à une modèle de trajectoire cyclique avec des contraintes de lissage approprié. Nous montrons que la transformation obtenue est capable de représenter fidèlement les mouvements du poumon tout en utilisant une paramétrisation plus compacte. En renforant la cohérence temporelle de la déformation à travers le cycle respiration, nous améliorons la robustesse du recalage aux artéfacts.

Comme application, nous avons également étudié la possibilité d'effectuer l'estimation de mouvement respiratoire à partir d'une séquence de projection CBCT. Un fort a priori sur la respiration du patient est introduit sous la forme d'un modèle spécifique au patient construit à partir d'une acquisition 4D CT préalable. L'estimation de mouvement est réalisée en comparant les projections avec une séquence simulée à l'aide du modèle. Nous proposons une approche d'optimisation semi-globale, considérant le cycle respiratoire dans son ensemble et fournissant des estimations lisses du mouvement.

Enfin, nous décrivons une approche préliminaire permettant de fournir une estimation per-opératoire d'une déformation moyenne du poumon. La méthode consiste à comparer une image patient à de multiples images projectives acquises dans la salle de traitement à partir de points de vue différents. En utilisant un a priori physiologique, nous montrons comment réduire fortement la complexité du recalage déformable. La similarité est ainsi mesurée dans l'espace des projections et un algorithme efficace est proposé permettant d'intégrer les informations obtenues des différentes vues. Les experiences initiales sont prometteuses et illustrent la faisabilité de cette approche.

Contents

List of Figures

List of Tables

1 Introduction

Abstract We address the issue of breathing motion for radiation therapy of lung cancer. First an introduction of the topic is given from the medical point of view and we present the imaging modalities used throughout this work. Next, the problem that arises from lung motion is illustrated and the need for motion modelling justified. The basic characteristics of respiratory motion are introduced starting with the physiology of breathing, followed by an overview of the most important studies providing respiratory motion data. The overview continues by discussing the different motion modelling approaches reported in literature. Finally, the approach chosen in this work is presented and choices on motion data and parametrization are motivated. We conclude by giving a conceptual overview of the contributions described in the following chapters.

Contents

1.1 Medical Context

1.1.1 Lung Cancer

Lung cancer is the most common cause of cancer death worldwide. It is the most common cause of cancer-related death for men and the second most common for women, behind breast cancer (Parkin et al., 2005). It accounts for an estimated 960 thousand new cases and 850 thousand deaths each year among men, and 390 thousand cases and 330 thousand deaths among woman. The survival rate is poor: 5-10% after five years (Boyle and Levin, 2008).

In most populations, tobacco smoking accounts for 80% or more lung cancers. Other causes include occupational and environmental exposures (e.g. asbestos, heavy metals, second-hand smoke). The risk of lung cancer among smokers relative to the risk among never-smokers is of the order of tenfold or more and tobacco control is the main tool in lung cancer prevention (Boyle and Levin, 2008). In the United Kingdom, the cumulative risk of lung cancer of a continuous smoker is 16%, and is reduced to 10%, 6%, 3% and 2% among those who stopped smoking at age 60, 50, 40 and 30, respectively.

In this work we are interested in radiotherapy, which is one of three currently available treatment modalities for lung cancer, along with chemotherapy and surgery. More often than not, radiotherapy is given in combination with either surgery or chemotherapy, or both. A little over 40% of all patients who develop lung cancer will require radiotherapy at some time during their illness (Boyle and Levin, 2008).

1.1.2 Radiotherapy

Radiotherapy consists of locally exposing target tumour cells to ionizing radiation with the aim of causing irreparable damage to their DNA. It has been prescribed since the early days of the X-ray era in medicine, going back as far as 1900. The 1950s marked a turning point, when major developments lead to improved effectiveness and reduced morbidity. The introduction then, of machines capable of delivering high-energy rays was critical to the further development of modern radiotherapy. From then on treatment involved Megavoltage (MV) X-rays (rather than kilovoltage beams, kV) or gamma-rays; the former from linear accelerators (linac for short) and the latter from high activity radioactive sources such as cobalt.

Here we will focus on external radiotherapy, delivered using a beam of MV X-rays produced by a linear accelerator. As beam sources are external

to the patient, all of the tissue along the path of the beam will receive some radiation dose. Regions of high dose in and around the target are created by spatially distributing the incidence and angle of treatment beams. In conformal radiotherapy, the beam is shaped to conform to the shape of the target, while limiting the dose delivered to organs at risk (OAR, e.g. the lungs, the heart and the spinal cord). Intensity modulated radiation therapy (IMRT) goes further by dynamically reshaping the outlines and intensity of the radiation field during treatment, and improving the fit of the high dose region to the tumorous region.

The amount of radiation delivered is measured in gray (Gy), and varies depending on the type and stage of cancer being treated. For curative cases, the typical dose ranges from 60 to 80 Gy. The total dose is fractionated (spread out over time), for several reasons. The primary being that fractionation allows normal cells time to recover, while tumour cells are generally less efficient in repair between fractions. Numerous fractionation schedules exist. Conventional treatments for adults involve typically delivering about 2 Gy per day, five days a week, for seven weeks. Hypofractionation schemes (involving fewer fractions with larger dose) have recently received considerable attention, including for lung cancer treatment (see section 1.1.5).

Before illustrating the problem that arises from respiratory motion, it is important to understand how radiotherapy is administered. The radiation therapy treatment process consists of two steps: treatment planning and treatment delivery. Planning starts by acquiring a computed tomography (CT, figure 1.1a) image of the patient onto which a radiation oncologist will delineate the visible target, called the *gross tumour volume* (GTV, figure 1.1b). Usually a margin is added to the latter to account for microscopic extension, thus obtaining the *clinical target volume* (CTV).

To account for geometric uncertainties associated with treatment planning and delivery, the CTV is extended to the *planning target volume* (PTV), for which the radiation oncologist prescribes the dose to be delivered. A medical physicist will then optimize the ballistics of the treatment (by influencing the number, angle and shape of the treatment beams), using a treatment planning system to simulate the dose deposition (figure 1.1c).

The second step is the treatment delivery. The patient is repositioned on the table in the treatment room by aligning skin marks to room lasers, by using a custom fitted body frame, or by using in-room imaging. In case of the latter, it is common to refer to image guided radiotherapy (IGRT). In-room imaging can consist of 2D kV or MV X-

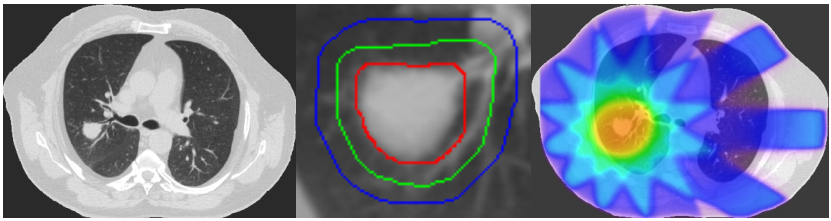

(a) (b) (c)

Figure 1.1: The process of treatment planning: (*a*) a CT image is acquired to serve as a reference for the planning, (*b*) the target is delineated (*red line*) and extended to account for biological and geometric uncertainties; (*c*) the treatment delivery is planned using a treatment planning system to simulate the dose deposition.

ray projections, conventional or cone-beam CT acquisition or even optical surface acquisition.

1.1.3 Imaging and Guidance

Radiotherapy has seen a technological avalanche in the last twenty years that has offered the same level of exciting prospects that the quantum leap from kV to MV equipment encouraged sixty years ago. Rapid advances in treatment delivery technology, imaging devices and computing capabilities have changed radiotherapy beyond recognition. A key advancement is the availability of imaging in the treatment room, allowing to improve accuracy of the treatment delivery. Another concerns the development of respiratory-correlated imaging, providing patient-specific respiratory motion for treatment planning.

Four-Dimensional CT Several groups proposed four-dimensional CT (4D CT) (Ford et al., 2003; Vedam et al., 2003; Low et al., 2003; Pan et al., 2004; Keall et al., 2004), allowing to image the patient at different stages of the breathing cycle. The technique consists of the simultaneous acquisition of CT data and a respiratory surrogate signal. The surrogate signal is used to sort the acquired data into bins according to the breathing state, and defines the fourth dimension of the obtained image. Three-dimensional (3D) reconstruction on each of the bins separately yields a respiratory-correlated image sequence, representing one breathing cycle.

Current CT technology does not allow to image the entire region of

interest (in case of lung cancer treatment, the entire lung) simultaneously. It is therefore necessary to acquire data from different parts of the anatomy at different times, and then combine this data to form coherent volumes. Different methods for acquiring the required data exist, including ciné and helical acquisition. In ciné mode, the CT scanner acquires the desired amount of data at each couch (table) position, before pausing and moving to the next position. In contrast, helical or spiral acquisition involves a slow, constant table motion during which CT data is acquired continuously. Popular respiratory surrogates for 4D CT include spirometry (Low et al., 2003), abdominal height (Vedam et al., 2003) or internal anatomical match (Pan et al., 2004).

Current 4D CT is based on the assumption that the respiratory cycle is periodical, and that the respiratory surrogate signal can be used to uniquely determine the respiratory state of the acquired data. The data sorting is usually based on the phase of the derived signal, but can also be the amplitude or combinations of both (Lu et al., 2006; Wink et al., 2006; Abdelnour et al., 2007; Olsen et al., 2008). However, breathing is not a periodic process, and the sorted data can contain inconsistent views of the patient anatomy. As a result, images can be blurred and motion-induced artifacts have been observed for about 80% of 4D CT acquisitions (Yamamoto et al., 2008).

Figure 1.2a depicts the CT scanner from which all CT images in this work were acquired, the Phillips Brilliance CT Big Bore 16-slice scanner (Phillips Medical Solution, Cleveland, OH). The surrogate signal required for respiratory-correlated imaging is provided by a pressure belt placed around the chest, the Pneumo Chest Bellows (Layafette Instrument, Lafayatte, IN). The scanner is operated in helical mode for the 4D CT acquisitions.

Cone-Beam CT Cone-beam CT (CBCT) (Jaffray and Siewerdsen, 2000; Jaffray et al., 2002) uses on-board imaging equipment mounted on the linear accelerator. This enables the patient to be imaged in position, just prior to treatment. The acquisition consists of a slowly rotating X-ray tube acquiring X-ray views of the patient on a large area, rectangular flat panel. Reconstruction yields a 3D CBCT image, though methods for respiratory-correlated CBCT have also been proposed (Sonke et al., 2005) and will soon become commercially available.

Different types of CBCT imaging systems exist. Some use the high-energy beam of the linac itself to acquire the the X-ray views (MV CBCT), while others use a separate kV X-ray source. The latter is

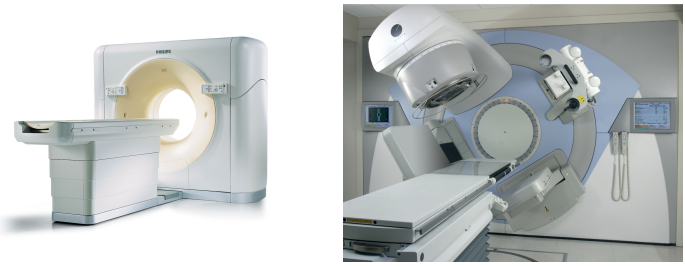

(a) (b)

Figure 1.2: The imaging devices from which all images in the work originate: (*a*) the Phillips Brilliance CT Big Bore Phillips (Medical Solution, Cleveland, OH) with 4D capabilities ; (b) the Elekta Synergy System (Elekta, Crawley, UK) with on-board kV Cone-Beam CT imaging.

usually mounted perpendicularly to the linear accelerator (kV CBCT). Both systems operate in a fairly similar fashion, although the quality of the images produced and the radiation dose required for the imaging can differ.

Figure 1.2b shows the first commercially available, linac-mounted cone-beam system, the Elekta Synergy (Elekta, Crawley, UK). The large X-ray source in the top left corner delivers the treatment beam, while the perpendicularly mounted kV source and flat panel is used for the image acquisition. All cone-beam data used in this work, was acquired on this type of imager.

1.1.4 Respiratory Motion in Radiotherapy

Respiratory motion introduces uncertainties in radiotherapy, influencing the accuracy of imaging, treatment planning and treatment delivery (Balter et al., 1996; Shimizu et al., 2000). Respiratory motion causes significant artifacts during three-dimensional (3D) CT imaging (van Herk, 2004; Chen et al., 2004) due to the interference of the scanning process and respiration. Treatment planning is essentially assuming a static anatomy, and organ motion will result in a deviation of the delivered dose from the treatment plan (Lujan et al., 1999; Guerrero et al., 2005). If not accounted for, organ motion due to breathing can lead to underdosage of the tumour, or overdosage of the surrounding tissue (Keall et al., 2006).

Properly accounting for breathing motion in the treatment plan, involves carefully evaluating the uncertainties of each step of the treatment

process, and is thus closely related to the imaging and treatment strategy (Wolthaus et al., 2008a). Imaging in the presence of breathing motion is preferably done by using slow, breath-hold or respiratory-correlated imaging. To avoid geographic miss of the target, the safety margins added to the target volume should reflect the patient-specific tumour motion. Margin reduction can be obtained by in-room imaging or through specifically designed treatment methods.

In particular, some treatment strategies aim at reducing the tumour motion during delivery, thereby limiting the margin required to account for the motion. For instance, treatment can be performed at *breath-hold*, effectively stopping the respiratory motion (although there may still be some residual motion due to limited reproducibility of the breath-hold (Sarrut et al., 2005)). Alternatively, the patient can be breathing freely but treatment is delivered only during certain breathing phases, in which case we refer to it as *gating*. The most ambitious method of treatment is called *tracking*, and involves following the tumour motion with the treatment beam during treatment.

1.1.5 Hypofractionated Treatment of the Lung at CLB

Hypofractionated treatment of the lungs has received considerable attention in literature recently. Remarkably high tumour control rates (which can be defined as the local disappearance of tumor cells) have been reported (Timmerman et al., 2007; Lagerwaard et al., 2008), making this a very promising treatment strategy for lung tumours. The low number of fractions and the high dose per fraction require high-precision treatment delivery, and justify the additional dose induced as a consequence of extensive image guidance.

We conclude this section by given an example of a particular treatment planning and delivery strategy, which is the hypofractionated lung cancer treatment as currently performed at the Léon Bérard Cancer Center, in Lyon, France. Medical indications to be considered for this treatment modality include non-small cell lung cancer without metastasis. In addition, the treatment is reserved for small targets (< 50 mm), which are not within 20 mm of the primary bronchi and characterized by relatively small motion under respiration.

Treatment planning is initiated by acquisition of a 4D CT image. Immobilization and localization is facilitated by placing the patient in a stereotactic body frame (SBF). Depending on the motion observed on

4D CT, abdominal compression is applied to reduce tumour motion to below 10 mm. Treatment margins are defined on a patient-specific basis, and chosen to encompass the total extent of the tumour motion as observed on 4D CT.

Treatment commences usually within ten days of the 4D CT acquisition and consists of four fractions of 12 to 15 Gy. At each treatment fraction, the patient is repositioned using the SBF and CBCT is performed to allow imaging the target just before treatment. Based on the CBCT image, the patient is repositioned by moving the table to align the target with the treatment plan, and treatment is started. The fractions are delivered twice a week.

1.2 Respiratory Motion Modelling

1.2.1 The Role of Motion Modelling in Radiotherapy

Modelling is in this work interpreted as

the mathematical description and characterization of a system, intended to provide an approximation of the physical reality

A respiratory motion model is meant to describe the motion of the anatomy of interest due to respiration. For some, respiratory motion models predict the internal organ motion, based on respiratory surrogate signals. We pursue a more general interpretation, by stating that the motion models can facilitate motion estimation, in situations where motion is difficult to quantify directly.

Besides the area of motion estimation, the mathematical description of the motion also enables computer simulation, which is a powerful tool for research. Most importantly, the process of motion modelling itself will bring about increased knowledge about respiration and improved insight into its effect on the radiotherapy treatment process. This in turn, can lead to new imaging and treatment strategies and modify the way breathing is handled in radiotherapy. Motion modelling is therefore first of all a tool to reduce the uncertainties introduced by respiratory motion, by improving its inclusion in the treatment process.

In terms of direct clinical applications, motion models could allow to reduce motion-induced artifacts and improve image quality by compensating the motion in images acquired for diagnosis (Lamare et al., 2007), treatment planning (Wolthaus et al., 2008b) or image guidance (Rit et al., 2009a). Treatment strategies can be evaluated by simulating the effect

of administering them during free breathing (Guerrero et al., 2005; Ayadi et al., 2007; Mexner et al., 2009; Seco et al., 2008; Colgan et al., 2008) and motion models are required for the prediction of tumour motion (Sharp et al., 2004; Seppenwoolde et al., 2007), required for gating and tracking.

An example is given by means of some of our initial work in this area, which consisted in making a simple motion model publicly available to the research community. The POPI-model [1] (Vandemeulebroucke et al., 2007)–in which POPI stands for point-validated pixel-based–consisted of a patient 4D CT acquisition for which we estimated the respiratory motion through deformable registration. The registration results were validated using anatomical correspondences throughout the image data provided by experts, resulting in a total of 400 landmarks. Validation data was also made publicly available. The initiative received good response and despite its simplicity, the POPI-model has since then been applied in varying applications including 4D dose simulation, motion compensated cone-beam reconstruction and validation of deformable registration (Ayadi et al., 2007; Wolthaus et al., 2008b; Noe et al., 2008; Rit et al., 2009a; Vaman et al., 2009; Kabus et al., 2009; Su et al., 2009a; Schmidt-Richberg et al., 2009b; Su et al., 2009b; Ruppertshofen et al., 2009, 2010).

1.2.2 Physiology and Mechanics of Respiration

Breathing is the process that allows to take oxygen in and let carbon dioxide out of the body. It plays a vital role in delivering oxygen to where it is needed. The actual process of gas exchange occurs in the lungs by passive diffusion of gases between the alveoli and the blood passing by in the lung capillaries. Once these dissolved gases are in the blood, the heart powers their flow around the body via the circulatory system.

Inspiration primarily requires contraction of the diaphragm and the intercostal muscles located between the ribs. Contraction of the diaphragm causes it to move downward and pushes the abdomen outwards and anteriorly. It increases the vertical dimension of the thoracic cavity, and results in an expansion of the lungs. The external intercostals contract to elevate the lower ribs and push the sternum outward, increasing the antero-posterior dimension of the thoracic cavity. Expiration is normally passive because of the elastic recoil. There is hysteresis in the relationship between pressure and lung volume; the lung volume is different between inspiration and expiration at the same pressure (Shirato et al., 2004).

1. http://www.creatis.insa-lyon.fr/rio/popi-model

Breathing is one of the few bodily functions which, within limits, can be controlled both consciously and unconsciously. Depending on the contribution of each of the breathing muscles, we can distinguish between diaphragmatic or thoracic breathing, though usually both are involved. For supine posture, diaphragmatic respiration is most common. The motion caused by the contraction of the respiratory muscles results in a complex deformation which differs from patient to patient, but also from cycle to cycle. It is influenced by the specifics of the patient anatomy, pathology, pose but also by physical condition and state of mind.

1.2.3 Obtaining Respiratory Motion Data

The access to valid motion data is a precondition for motion modelling. Unfortunately, obtaining accurate measurements is a difficult, laborious and time-consuming task for both patient and practitioner. Technical limitations apply to the accuracy, dimensionality and resolution of the measured motion. In addition, the measurements often induce an imaging dose to the patient, limiting the duration and repetition of the measurements. This explains why, despite the considerable interest in the topic, accurate motion data is still relatively scarce.

Respiratory motion is different from individual to individual. It occurs in three-dimensions, is non-rigid and non-periodic of nature, and is characterized by variations on short, middle and long term. Ideally, we would acquire 3D+time (T) signals for a dense spatial grid of tissues, at a high temporal resolution, for a large patient group and over a clinically relevant duration (e.g. over the course of a treatment duration). In practice, a compromise must be found in which one or several of the previous conditions are relaxed.

Breathing motion has been measured in a number of ways, including using ultrafast CT (Ross et al., 1990), ultrasound (Davies et al., 1994), fluoroscopy (Kubo and Hill, 1996), Optical sensors (Vedam et al., 2001), 4D CT (Mageras et al., 2004), 4D MRI (Plathow et al., 2004), CBCT (Purdie et al., 2007b), 4D CBCT (Sonke et al., 2008) and CB projections (Rit et al., 2009a). Studies have focused on the diaphragm (Balter et al., 1998), implanted markers (Seppenwoolde et al., 2002), abdominal height (George et al., 2005b) or on the whole thorax (Boldea et al., 2008). The dimensionality and the spatial and temporal resolution of the measurements vary and depend on the modality on which they were acquired and the method used to analyze the motion. Table 1.1 list some key studies providing measurements on respiratory motion. view focusses on lung motion during

free breathing, though some studies include measurements for the liver and with use of abdominal compression.

Several studies provided 1D+T measurements at high temporal resolution, but for isolated structures such as markers or the diaphragm. Very few approaches actually led to 3D+T motion and none of them provide them for a dense grid of points covering the entire thorax. Dedicated equipment has been used to provide 3D+T motion over long durations and at high temporal frequency. Ciné CT imaging can provide 3D images from which dense motion can be estimated, but cover only about 20 mm of the thorax. Dense motion estimates for larger regions were mainly obtained for modalities that rely on a periodicity assumption (indicated by T°), namely 4D CT and 4D MRI. However, this assumption excludes studying intercycle variability as the acquired data is binned to similar breathing stages and reconstruction yields one cycle. In addition, they are usually characterized with a reduced temporal resolution.

That being said, 4D CT and (4D) CBCT have been the preferred modality for recent studies on respiratory motion in recent years, mainly because of the wide availability of this data. Treatment strategies such as the hypofractionated treatment of the lungs described in section 1.1.5, have led to the routine acquisition of 4D CT and CB CT for treatment planning and image guidance, respectively. Finally, we bring the attention to approaches based on MRI. Fast 3D MRI hasn't yet allowed to extract dense spatial estimates (Blackall et al., 2006), due to the reduced image quality. However, the non-invasive character of the modality allows long acquisition times, enabling more elaborate binning procedures that produce high quality respiratory-correlated MRI (von Siebenthal et al., 2007). The availability of dynamic MRI data is currently limited, because it is not part of standard clinical protocols. Its properties could cause MRI to play an increasingly important in respiratory motion modelling in the future.

Study	Modality	Method	Motion	RIO	Frequency	#P	#M / P	Characteristics
Seppenwoolde et al. (2002)	Fluoroscopy	RTRT	3D+T	Markers	30 Hz	20	16×300 s	IR and IA var.
Gierga et al. (2004)	Fluoroscopy	BM	1D+T	Clips	30 Hz	7	2×30 s	Amplitude
Plathow et al. (2004)	2D MRI	Manual	2D+T	Tumor	3 Hz	20	30 s	Amplitude
Mageras et al. (2004)	4D CT	Manual	3D+T°	Tumor	5/cycle	12	1	Ampltude
George et al. (2005a)	Fluoroscopy	ADDE	1D+T	diaphragm	10 Hz	5	12×30 s	Amplitude
George et al. (2005b)	Optical	RPM	1D+T	Abdomen	30 Hz	24	14×240 s	Baseline, phase, ampl.
McClelland et al. (2006)	3D ciné CT	DIR	3D+T	Dense VF	1.5 Hz	5	20 s	Average cycle
Blackall et al. (2006)	3D MRI	AIR	3D+T	Dense SL	3 Hz	15	2×52	Amplitude
von Siebenthal et al. (2007)	4D MRI	DIR	3D+T°	Dense VF	10/cycle	11	1	Intercycle var.
	2D MRI	DIR	2D+T	Dense VF	2.7Hz	11	210	IA drift
Guckenberger et al. (2007)	4D CT	Manual	3D+T°	Tumor	10/cycle	10	4	IR amplitude var.
Purdie et al. (2007a)	4D CT	Manual	3D+T°	Tumor	10/cycle	28	1	Amplitude
	4D CT, CBCT	LRIR	3D	Tumor	/	28	4	IR baseline shift
	CBCT	LRIR	3D	Tumor	/	8	3	IA baseline drift
Boldea et al. (2008)	4D CT	DIR	3D+T°	Dense VF	10/cycle	5	1	Intracycle var.
Sonke et al. (2008)	CT, 4D CBCT	LRIR	3D+T°	Tumor	10/cycle	56	9	IR var.
Bissonnette et al. (2009)	4D CT, 4D CBCT	LRIR	3D+T°	Tumor	10/cycle	18	12	IA, IR amplitude var.
Rit et al. (2010)	CB projections	ADDE	1D+T	diaphragm	5.5 Hz	33	8×120 s	IA, IR amplitude var.
Ding et al. (2010)	4D CT	DIR	3D+T°	Dense VF	10/cycle	5	2	IR var. in ventilation

Table 1.1: Overview of some key studies providing respiratory motion measurements. For each study we mention: the main acquisition modality (*Modality*), the method used to extract the motion (*Method*), the dimensionality of the measured motion (*Motion*), the structure(s) for which the motion was studied (*RIO*), the frequency of the measurements (*Frequency*), the number of subjects (patients and or volunteers) included (*#P*), the average number of measurement and/or the duration per patient (*#M / P*) and the characteristics of the motion that were reported (*Characteristics*). Abbreviations: RTRT=Real-Time Tudor Tracking Radiotherapy system; ADDE=Automated Diaphragm Dome Extraction; RPM=Real-Time Position Manager; AIR=Affine Image Registration; DIR=Deformable Image Registration; LRIR=Local Rigid Image Registration; SL=Surface Landmarks; VF=Vector Fields; IA=Intrafraction; IR=Interfraction; var.=variability. The symbol T° indicates, the measurement was obtained by assuming motion periodicity.

1.2.3.1 Characteristics of Respiratory Motion

In the interest of furhter analysis, the high-dimensional motion data is decomposed and certain aspects of it are reported in an attempt to characterize the motion due to respiration. Often, this analysis involves fitting a motion model to the data, and reporting the best matching values for the model parameters. In other words, analysis of breathing motion has contributed to motion modelling. The distinction made between studies mentioned in the current section, said to provide measurements on respiratory motion, and the work reviewed in the next section on motion modelling is therefore somewhat arbitrary and arguable for some.

Breathing occurs predominantly in the superior-inferior (SI) direction. The extent of the motion tends to be larger for the lower lobes and for structures near the diaphragm where it can easily reach 30 mm (Keall et al., 2006). Breathing periods range from 2 to 10 s with an average just below 4 s, though the measure is characterized by large interpatient variability (George et al., 2005b; Rit et al., 2010). The path followed by moving structures during inhalation can be different from exhalation, leading to hysteresis (Seppenwoolde et al., 2002; Boldea et al., 2008). Several authors reported variable speed over the cycle, spending more time near exhale than inhale (Kubo and Hill, 1996; Seppenwoolde et al., 2002; Rit et al., 2010).

The average motion amplitude is of the order of 15 mm at the diaphragm, but also varies greatly from patient to patient (Rit et al., 2010). The amplitude has been reported to be relatively stable between fractions (about 2 mm standard deviation at the diaphragm), but larger intercycle variability has been observed intrafractionally (Sonke et al., 2008; Rit et al., 2010). This variability is mostly attributed to the variability of the end-inhale position (about 3 mm standard deviation at the diaphragm) which is about twice as high as the end-exhale position (Seppenwoolde et al., 2002; Sonke et al., 2008; Rit et al., 2010). The trajectory shape was found to be stable interfractionally, and its variability is relatively small (Seppenwoolde et al., 2002; Sonke et al., 2008).

Changes in the mean position of moving structures, generally referred to as variations of the baseline, have also been observed. They can occur both intra- and interfractionnally, and in all three dimensions. The baseline can be subject to progressive trends over time or sudden shifts, and both have been observed during and between treatment fractions (Seppenwoolde et al., 2002; Purdie et al., 2007b; Sonke et al., 2008; Bissonnette et al., 2009)

1.2.4 Models For Respiratory Motion

Numerous respiratory motion models have been proposed in literature. Depending on the application, they aim at describing the average motion, or tend to characterize the intercycle variability. Some focus on the motion of single points or structures, while others provide a description for the whole thorax. Note that most models provide the internal motion based on a surrogate respiratory signal. In practice, this surrogate is based on a measurement that can be performed during imaging or treatment delivery, such that it would allow intrafraction motion estimation, during these processes. Surrogates range from spirometry, optical abdominal height tracking, X-ray diaphragm tracking, but can also be derived from fan-beam or cone-beam projections.

1.2.4.1 Biomechanical Modelling

Biomechanical approaches aim at physically simulating processes using the laws of physics and based on physiological and anatomical observations. These can be formulated as a boundary value problem and solved, for instance, using finite element methods (FEM). Biomechanical modelling of the lung goes back as far as the 1970's, with the work of Mead et al. (1970) and announced the start of an increased interest in lung mechanics (Fung, 1974; Vawter et al., 1979; Wilde et al., 1981). The first finite element models of the lungs quickly followed (West and Matthews, 1972; Matthews and West, 1972; Vawter, 1980), initially developed to determine the macroscopic stress, strain and deformation of the lung parenchyma.

Related to this, is the work of Segars (2001) in the development of the dynamic NURBS-based cardiac-torso phantom (NCAT): a geometric model of the thorax which was attributed realistic respiratory mechanics and cardiac motion based on CT and MRI observations. The phantom proved to be a powerful simulation tool and was used in many studies, including dynamic imaging (Segars and Tsui, 2002; Segars et al., 2003; Lamare et al., 2007) and 4D dose estimation (Guerrero et al., 2005).

More recent biomechanical studies used CT (Villard et al., 2005) and MR images (Brock et al., 2005) to obtain a patient-specific topology for the 3D FEM models, mainly in the interest of motion estimation. Despite the increasingly detailed models, current biomechanical approaches still greatly reduce the available image information. The lung parenchyma is generally assumed to be linear-elastic, homogeneous and isotropic and inner-organ information like bronchial or vessel trees are dismissed.

This results in less accurate registration of those structures compared to intensity-based deformable registration (Sarrut et al., 2007; Werner et al., 2009b).

Advantages of biomechanical modelling lie in the fact that they allow to explicitly account for physical properties and physiological processes. An example is given by the sliding motion of the lung with respect to the chest wall, known to cause locally reduced matching accuracy for most deformable registration algorithms (Wu et al., 2008; Schmidt-Richberg et al., 2009a; Vandemeulebroucke et al., 2010). This behaviour has previously been successfully modelled as a contact problem of elasticity theory (Zhang et al., 2004; Villard et al., 2005; Al-Mayah et al., 2008; Werner et al., 2009a), providing an advantage over conventional registration approaches.

1.2.4.2 Signal Models

We use the term signal models to refer to models describing the motion of a single point or structure, or of a respiratory trace or surrogate. This type of respiratory motion models has received considerable attention in literature. Their development was mainly motivated by the increasing interest in gated or tracked treatment delivery, and their development benefitted from the comparatively easy access to large sets of motion data. As such, they played an important role in characterizing the different aspects of respiratory motion.

Lujan et al. (1999) described organ motion due to breathing using a modified cosine model

$$\boldsymbol{x}(t) = \boldsymbol{x}_0 - \boldsymbol{b}\cos^{2n}(\pi t/\tau - \phi)\,. \tag{1.1}$$

In this equation, $\boldsymbol{x}_0$ is the position at exhale, $\boldsymbol{b}$ is the extent of the motion and τ is the period of the breathing cycle. The parameter n controls the shape of the model, allowing to describe asymmetric trajectories that spend more time at exhale than at inhale, as observed using fluoroscopy (Kubo and Hill, 1996; Balter et al., 1998). The model parameters were assumed fixed and meant to represent an average breathing cycle, allowing to simulate the impact of respiratory motion on dose distributions using dose-convolution techniques (Lujan et al., 1999; Chetty et al., 2003). The representation became widely adopted and has since been applied for a variety of applications (Seppenwoolde et al., 2002; van Herk et al., 2003).

Neicu et al. (2003) described how to capture a more detailed waveform model using a concept called the average tumour trajectory. In their work,

the minima and maxima in the superior-inferior direction are matched, and the waveform is normalized and averaged to better describe the characteristic motion.

Wu et al. (2004) proposed a finite state motion model in which regular breathing cycles are represented by a piecewise linear model, while abnormal breathing is represented by an irregular breathing state. The regular cycle consists of line segments for inhale, exhale and end-exhale. An advantage of the proposed formalism is that it provided a convenient base for statistical analysis (Wu et al., 2007).

Low et al. (2005) proposed a linear relationship between the position of a point $\boldsymbol{x}$ and the instantaneous air volume v and air flow f (its derivative), as measured through spirometry

$$\boldsymbol{x}(t) = \boldsymbol{x}_0 + c_1 v(t)\boldsymbol{e}_v + c_2 f(t)\boldsymbol{e}_f. \tag{1.2}$$

The constants c_1 and c_2, and the directions of the unit vectors $\boldsymbol{e}_v$ and $\boldsymbol{e}_f$ were obtained by fitting (1.2) to measurements obtained from ciné CT data and simultaneously acquired spirometry (over 11 seconds, corresponding to 15 CT volumes and 2-3 cycles). Motion is constrained to a plane and changes in each of the surrogates resulted in displacements in different directions on the plane. The airflow component was accounted for the hysteresis and different combinations of volume and flow allowed to model intercycle variability.

Seppenwoolde et al. (2007) studied the prediction capabilities of a commercially available robotic respiratory tracking system (the Synchrony Respiratory Tracking System used with the Cyberknife system, Accuray, Sunnyvale, CA). Internal motion data was obtained from X-ray imaging of implanted markers, and is correlated to external skin markers during a pre-treatment training period. Quadratic correspondence models were found to be superior to linear in the presence of motion hysteresis, but the use of a single surrogate model (center of mass of the external markers), limited the capabilities of modelling intercycle variations.

Ruan et al. (2009) described a method for real-time profiling of respiratory motion, by decomposing it into baseline, frequency and fundamental pattern variations. The approach was motivated by the fact that changes to each can have different clinical consequences, depending on the application. Each of the motion components was assumed to evolve smoothly in their own space. This allowed additional filtering of the decomposed signal which augmented robustness to noise. By decomposing, filtering and then reassembling the components in the original signal space, a stable predictor was provided that incorporated most physical priors for

respiratory motion.

In summary, signal models have benefited from the comparatively easy access to motion data. This has allowed several authors to propose direct relationships between the target motion and specific characteristics of respiration. Whether it concerned establishing a link between the motion and the breathing state (Wu et al., 2004), external surrogate (Low et al., 2005) or a certain aspect of breathing (Ruan et al., 2009), the approaches allowed for a spatial or temporal decomposition of the breathing motion and simplified motion characterization in subsequent analysis. A drawback of this modelling approach is that their use is mainly limited to respiratory-synchronized treatment delivery as they describe the motion of a single point.

1.2.4.3 Registration-based models

Recently, several models have been proposed that describe the internal motion of an entire region, in contrast to just considering a specific point. Their popularity can be explained by the recent developments in imaging technologies, improving accessibility to rapid or respiratory-correlated CT images. The method for obtaining dense motion estimates from the motion data is primarily intensity-based deformable registration, which is why we refer to these models as registration-based.

McClelland et al. (2006) proposed a method for obtaining an average breathing cycle from CT data covering multiple cycles. The models are constructed from small slabs of ciné CT data, acquired during free breathing over a period of about 20 s. A respiratory surrogate signal was simultaneously recorded in the form of abdominal height measurements. Each of the free-breathing ciné volumes was registered to a reference breath-hold CT scan of the same patient. The actual motion model was obtained by temporally fitting each of the registration parameters with respect to the breathing phase derived from the surrogate signal using a one-dimensional cycle B-spline. As the data covers several respiratory cycles, the obtained function should model a cycle which can be considered average in deformation space. By composing the 4D models obtained at each couch position, a description covering the entire region of interest was obtained.

Validation included predicting the registration results by using *leave-one-out* experiments: the temporal fit was performed using all ciné volumes except for one, and the obtained model was evaluated by comparing it to the target left out, at the same phase value. Even though no intercycle

variability was modelled, the motion models predicted the individual free-breathing volumes surprisingly well. This illustrates the clinical advantage of using an average cycle as a motion predictor, compared to conventional 4D CT which effectively represents an arbitrary respiratory cycle at each table position. Another advantage of the method, lies in the fact that composing the average models at each couch position reduces the artifacts with respect to simply composing the free-breathing cinv́olumes corresponding to the same phase bin. On the downside we should mention that the acquisition of the ciné CT data generally induces more imaging dose to the patient, compared to shorter 4D CT acquisition schemes.

Later work included extending the motion models to more respiratory parameters, with the aim of modelling intercycle variability (McClelland, 2008). The procedure followed was similar with the main difference being that now a 2D function was fitted to establish the relationship between two model parameters (a combination of amplitude, phase and gradient of the surrogate signal) and the registration parameters. A number of functions were evaluated, for a varying amount of degrees of freedom. The results however, when evaluated using the leave-one-out experiments, showed little or no improvement over the single parameter models. Some of the evaluated functions with high degrees of freedom, clearly resulted in an over-fitting of the registration results. Although the concept showed potential for modelling intercycle variability, the limited amount of data was suspected to limit the potential.

Zhang et al. (2007) proposed a method for obtaining a motion model from a single 4D CT acquisition. Their approach aimed at predicting the motion based on two respiratory surrogates, the current height of the diaphragm and its height 1.5 s earlier. The motion in the 4D CT was analyzed by non-rigidly registering all the frames to the reference end-exhale frame. The relation between the deformation and the model parameters was obtained through principal components analysis (PCA). Each of the frames of the 4D CT was considered as an independent breathing state. The first two principal modes were retained, and shown to account for the majority of the variation of the included patient data. A fundamental breathing pattern was obtained as a linear combination of the two principal modes of the PCA. The removal of the remaining modes was interpreted as a filtering operation for the deformation fields. This was supported by examples in which the model predictions, consisting of the transformed reference exhale CT volume, were compared to the original frames of the 4D CT. A reduction of the image artifacts was observed, indicating the models were actually more representative of the

true respiratory motion.

Since more than one surrogate was used, the approach can potentially also describe intercycle variation. However, the method was based on only one 4D CT, not providing any data on variation. Nonetheless, their performance was assessed when used to predict 4D CT data of the same patient acquired about a week later. The predictions were still acceptable, even in the presence of a considerable baseline shift between the two sessions. This robustness is mostly attributed to a good choice of respiratory surrogate, capable of accounting for such interfractional differences.

In (Yang et al., 2008), and extension to the signal model described in (Low et al., 2005) was presented. Motion was analyzed from the ciné CT volumes using deformable registration with respect to a reference volume, similar to (McClelland et al., 2006). For each of the voxels, a model equation similar to (1.2) was fitted to the obtained deformation vectors. Since the model was now evaluated over the entire lung regions, 3D maps of the obtained parameter values were reported that showed fairly smooth variations throughout the lungs, as would be expected. Zhao et al. (2009) performed a similar analysis to a large patient group, to analyze interpatient motion characteristics.

Several authors have proposed to provide motion estimation based on X-ray projections taken from rotating views (Blondel et al., 2004; Zeng et al., 2005, 2007; Li et al., 2007; Rit et al., 2009a; Long et al., 2010). This highly interesting line of research could provide intrafraction respiratory motion estimation from cone-beam projections, and enable exploiting the large amounts of projection data acquired in clinical routine. The projection images can be seen as a high-dimensional respiratory surrogate signal, which in combination with some kind of patient model can facilitate motion estimation.

Zeng et al. (2007) used a general deformation model based on free-form deformations (Rueckert et al., 1999) to deform a reference patient CT image to match the respiratory motion in a cone-beam projection sequence. The procedure comes down to a 2D+T-3D+T registration, driven by an intensity-based similarity measure calculated between the projection sequence and the projection views of model. To facilitate the optimization, temporal regularization was introduced in the form of a pseudo-periodicity penalty. The method was later applied to motion-compensated CBCT reconstruction (Li et al., 2006). Long et al. (2010) proposed a similar approach, to estimate 3D motion from a series of projections. In this case the patient motion over the duration of the projection sequence was

considered negligible.

Rit et al. (2009a) proposed to introduce a prior about the patient's breathing motion in the process. The prior was obtained from a previously acquired 4D CT acquisition, and the 2D-3D motion estimation was reduced to establishing a correspondence between the 4D model and the projection sequence in phase space. By extracting the breathing phase from the projection sequence using a fast, feature-based method (Zijp et al., 2004), on-the-fly motion-compensated CBCT reconstruction was demonstrated (Rit et al., 2009b), making insertion of the method into clinic feasible.

In conclusion, registration-based modelling can address a wider range of applications, as motion is described for a larger region. Compared to the previously discussed signal models, substantially less patient-specific data is usually available, limiting the potential of the methods to model the motion variability. With respect to other respiratory surrogates, 2D rotational X-ray projections contain detailed (internal) motion information with the potential of complementing CT data, and efforts have been made towards exploiting this type of data for intrafactional motion estimation. Without prior knowledge, establishing the relation between the CT images and X-ray projections sequences is challenging, due to high dimensionality of the resulting 2D-3D motion estimation problem.

1.2.4.4 Statistical Models

Instead of trying to predict deformation for a specific patient at a specific time, several studies been dedicated to the statistical analysis of patient breathing motion. The aim in this case is mainly to report general characteristics of a patient breathing pattern, or even to extract interpatient breathing generalities, even though some attempts at interpatient motion estimation have been reported as well.

George et al. (2005b) analyzed a great number of respiratory traces, obtained from abdominal height measurements. Rather than considering the modified cosine motion model (1.1) as an average trajectory with constant parameters, the equation was fitted to individually extracted cycles. This allowed to quantify average parameter values and their variations for a statistically important patient sample. The study also estimated the probability density functions for each of the model parameters can be used to generate more realistic respiratory traces.

Wu et al. (2007) applied a finite-state (inhale, exhale and end-exhale) motion model (Wu et al., 2004), to a large data set of tumour trajectories

described in (Seppenwoolde et al., 2002). They applied statistical analysis and correlation discovery methods to extract intra- and interpatient breathing characteristics useful for treatment planning, online tumour motion prediction and real-time radiation dose delivery. Conclusions of the analysis included that the most time of the trajectory is spent in the end-exhale state (1.46 s with respect to 1.33 s for inhale and 0.99 s for exhale), which is also the state during which the tumour travels the least distance (2.04 mm with respect 10.42 s for inhale and 8.64 s for exhale).

Ehrhardt et al. (2009) used 4D CT acquisitions obtained from 18 patients to compute a statistical mean interpatient motion model. Deformable registration was applied to analyze the intrapatient motion, but also to establish an interpatient anatomical correspondence. Using an approach inspired from the construction of anatomical atlases (Ehrhardt et al., 2008), an average shape and intensity reference anatomy was computed onto which the individual patient breathing motions were mapped. By normalizing the motion with respect to the change in air content and spatially averaging the patient motion models, a mean respiratory motion model was obtained.

The prediction capabilities of the mean model were evaluated by providing a patient-specific scaling for the mean model (using the required change in air content), and comparing it to the patient images in a leave-one-out fashion. Results were surprisingly good, considering the limited patient-specific information provided. By calculating the difference between the scaled mean motion model and a patient-specific motion estimate, deviating respiratory behaviour could be identified, illustrating a possible application of an interpatient model.

While probably less suitable for patient-specific motion estimation, statistical and interpatient models have been shown very helpful to establish general properties about breathing motion. This knowledge is useful for conducting realistic simulation studies, or to tune treatment strategies by testing them on an *average* patient population. In addition, thorough analysis of motion data, obtained from a large patient group, has the power to on one hand confirm seemingly obvious aspects of breathing motion, and on the other hand reveal underlying motion characteristics.

1.3 Our Approach: Formalization of Breathing Motion and Reduction of the Degrees of Freedom

The purpose of this section is to motivate the choices made regarding the modelling approach. This concerns the used motion data and priorities considered for the different aspects of breathing motion. A second motive of this section is to give a conceptual outline of the methodological contributions described in the chapters to follow.

1.3.1 Objective and Problem Statement

The objective of this work can be stated generally as:

To provide methodological contributions that improve the quantification, representation and characterization of lung motion and facilitate its inclusion into radiation therapy treatment planning and delivery for lung cancer.

In particular, the main treatment strategy in mind concerns stereotactic hypofractionated radiotherapy of the lungs described in section 1.1.5. This procedure involves continuous photon radiation during free breathing (in contrast to using, breath-hold, gated or tracked treatment delivery). In addition, only patients treated without abdominal compression were considered. It goes without saying that the use of some of the methods proposed extends beyond this context. The specifics of the problem description however, allows to make several assumptions about the motion modelling problem at hand.

For the aimed application, patients are in supine position. Even though in-room imaging is performed at each treatment session, it can be assumed that careful patient setup on the treatment table is performed before imaging at the beginning of each treatment fraction. About 3 to 4 weeks go by between the beginning of treatment planning to the end of treatment delivery. Attention should therefore be paid to modelling motion variability in short as well as longer term. On the other hand, this duration is short enough to assume a certain stability of the patient anatomy. Breathing motion is known to change from one patient to another. In addition, the studied patient group suffers from lung pathologies (tumours in varying places, atelectasis, pleural effusions, etc.). For this patient group even stronger deviating motion behaviour can be expected (Plathow et al.,

2004; Ehrhardt et al., 2009). The emphasis in this work is on exploring the individualization of the treatment by modelling the patient-specific motion.

1.3.2 Motion Data

1.3.2.1 Four-Dimensional CT

4D CT was chosen as the main source of patient-specific motion data. The advantages are mostly of practical nature. It is routinely acquired in our institute for the treatment planning of the considered patient group, thus not requiring additional acquisitions outside the treatment protocol. Its acquisition is fast, and the patient is carefully set up allowing assumptions to be made on the geometry. With respect to other modalities there are also some technical advantages. The obtained images are of comparatively high resolution and are characterized by excellent contrast in the lungs, allowing methods such as deformable registration to be applied. In addition, the modality basically provides an electron density map of the imaged object, which is required to simulate the treatment delivery using a treatment planning system.

The main drawbacks of the modality is that its acquisition involves an imaging radiation dose, which explains the low dose levels per image compared to diagnostic CT, and limits the number of acquisitions. Advanced binning algorithms described for 4D MRI (von Siebenthal et al., 2007), requiring long acquisition times and large quantities of data are not applicable to 4D CT. Intermediate approaches, based on ciné-CT images (Low et al., 2005; McClelland et al., 2006) providing limited statistics and sampling some intercycle variability, were not pursued either. Instead, little over a cycle is acquired at each table position and data corresponding to similar breathing phases is combined using the slice stacking principle and assuming motion periodicity, without any further selection of the data being applied. A first consequence of this procedure, is that there is no way of knowing if the reconstructed cycle is representative of the patient's breathing pattern, since at each position an arbitrary cycle was acquired. A second effect is that irregular breathing will lead to inconsistent projection views that cause artifacts in the reconstructed images. In addition, by itself 4D CT does not allow to account for intercycle variability.

1.3.2.2 Cone-Beam CT

Cone-beam CT acquisitions are also routinely acquired for the patient group of interest, at the start of each treatment fraction. Their main advantage from the perspective of motion modelling is that they are acquired just moments before treatment, with the patient in treatment position. 3D CT provides little useful motion information, as motion is averaged over the acquisition time. 4D CBCT (Sonke et al., 2005) assumes motion periodicity, similar to 4D CT, but has the advantage that several acquisitions are available over the course of treatment, allowing to study interfractional variability (Sonke et al., 2008). The image quality is significantly lower than 4D CT, rendering the analysis using deformable registration more challenging.

Cone-beam projections consist of large angle X-ray projections, acquired on a planar flat-panel (425 mm length) and covering a large part of the thorax (276.7 mm at the isocenter). The images are of high resolution (0.8×0.8 mm^2, corresponding to 0.52×0.52mm^2 at the isocenter) and have good temporal frequency (5.5 frames/s). Motion-induced artifacts are limited due to the fast acquisition times of the projections (20-40 ms) and the projection sequences are available over relatively long durations (2-4 min).

Before being able to benefit from the interesting properties of this type of data, several challenges have to be faced to enable their exploitation. The most obvious one being that the modality is inherently a 2D+T representation of 3D+T motion, making it difficult to quantify the motion. Equipment, such as the treatment table or the stereotactic body frame, overlap with the structures of interest and further compromise respiratory motion estimation.

Cone-beam projections were used in this work to complement the 4D CT motion data, and served several purposes. To circumvent the difficulty of extracting the full 3D+T motion, different strategies were applied. In some cases the sequence was reduced to a 1D+T motion signal of a single, clearly identifiable structure, enabling statistical modelling due to the size of the available data. The projections also served as a high-dimensional respiratory surrogate, to facilitate 3D+T motion estimation in the treatment room. Alternatively, particular projections were selected and combined to provide a 3D update of the patient model.

1.3.3 Motion Formalization

In brief, lung motion is characterized by variations occurring at different time-scales, which may occur for different physical and physiological reasons. Each of them may have a different effect on the treatment process. As such, there may be a clinical advantage in detecting and quantifying each of them separately. We propose to explicitly decompose respiratory motion, and to let the model parametrization reflect this, similar to some of the signal modelling approaches mentioned in section 1.2.4.2. In addition, we propose to account for each aspect of breathing motion separately, with the required spatial accuracy and at an adequate temporal frequency. We use the term *formalization* to refer to the process of decomposing the motion, and attributing fixed spatial and temporal representations to compensate for each of the events.

Figure 1.3 shows a schematic representation of a respiratory trace, influenced by different types of motion variability. At the top, a distinction is made for clinically relevant time spans, ranging from seconds (intracycle) to weeks (interfraction). At the bottom, the types of motion variability that can be expected are summarized briefly. In bold, the specific mechanism considered to account for the type of motion. Each of the latter corresponds to a model parameter and should be characterized with its own spatial and temporal parametrization. Note that this decomposition is a simplification of reality, and reflects an explicit choice that remains to be validated.

Over the course of a breathing cycle, the breathing muscles contract causing the chest volume to increase, and air flows in as a consequence of the disequilibrium in pressure. At the point of maximum inhalation, the muscles suddenly relax and organs move back to their resting position due to the elastic recoil. All of this occurs in a time-span of 2-10 s. And the process is repeated, possibly at a different speed. Intracycle variability is mainly accounted for by variations in *phase*. It encodes the patient-specific breathing pattern that describes the complex deformations that occur when passing from one phase to another. It also allows to represent some variability, by producing changes in breath rate. The phase parameter associated with it is periodic, implicitly enabling the representation of hysteresis. The phase to phase deformations will be estimated from a patient-specific 4D CT acquisition using deformable registration.

The breathing level can change irregularly from one cycle to another, but it can also vary from a sequence of cycles to another due to change in metabolism or state of mind. It will mainly cause the final end-inhale

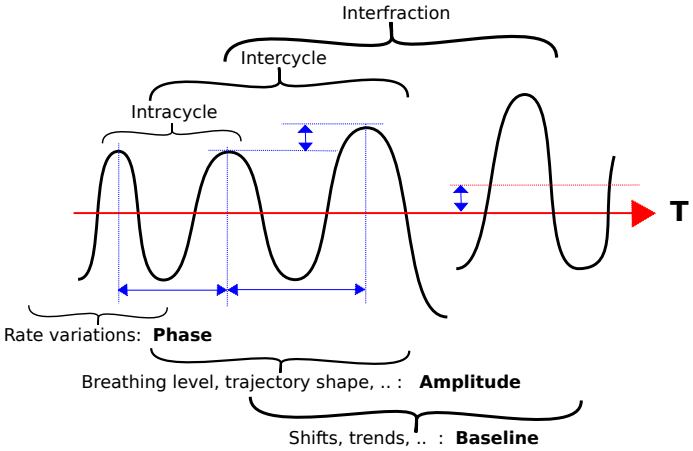

Figure 1.3: Illustration of the different aspects of breathing motion (*bottom*), occurring at different time spans (*top*). For each, the mechanism considered in the motion model is mentioned in bold.

position of the diaphragm to vary from one cycle to another and potentially also the path followed during inhale and exhale. Intercycle, intrafraction and interfraction variability might therefore require a modification of the breathing pattern and breathing level, which is taken into account in the motion model through variations in *amplitude*. A simple mechanism is provided to allow for limited variation of the patient's breathing pattern. A proper value for the amplitude parameter should be selected by fitting the motion model to timely motion data, for instance a cone-beam projection sequence.

The baseline of motion has been known to vary as well. Systematic shifts or progressive time trends between beams and/or fractions can occur. The time trend could be attributed to gradual patient relaxation throughout the treatment or to gravity action on compliant lung tissue shortly after having assumed the supine position (Shirato et al., 2004). A systematic shift could be caused by changes in muscle tone, stomach filling, patient position or pose. These longer term intrafraction and interfraction changes in mean position are accounted for through variations in *baseline*. As baseline variations have been reported to occur randomly and in all three dimensions, no specific prior about their spatial representation can be deduced from the 4D CT acquisition. They should therefore be monitored at periodic interval and on a patient-specific basis. This can be done for

instance by updating the model using (4D) CBCT. We explored a method providing an update based on selected cone-beam projections.

1.3.4 Model Parametrization

The actual parametrization of the motion plays an important role because it is directly related to the number of parameters required to characterize the model and determines the number of degrees of freedom considered when estimating the model. Ideally, the chosen parametrization is flexible enough to accurately represent a large variety of breathing patterns and account for its variability. From the point of view of optimization however, it is desirable to dispose of a compact and efficient representation. In the interest of robustness, explicit parametric restrictions should limit the representable space to *plausible* deformations, from a physical or physiological point of view.

B-splines were selected as the basis for the spatial and temporal parametrization of the motion model. The main argument in favour of B-splines is their flexibility to represent a large variety of deformations. The scale and order of the spline model controls the smoothness of the displacement field, providing a convenient framework for tuning the complexity of the model to match the yet unknown physical reality. B-splines are characterized by implicit smoothness and computational efficiency. They also allow an easy extension to higher dimensions, which was exploited to enforce smoothness in all spatial dimensions and across time.

Three specific aspects of the representation were investigated more in depth, to increase the efficiency of the B-spline parametrization of breathing motion. The first concerns the conversion of B-spline coefficients to the encoded values, required frequently for image registration and intensity interpolation. We contributed in developing a more efficient algorithm for performing these basic steps. A second aspect, concerns the spatial representation of sliding motion, known to occur during respiration. The use of uniform B-splines for representing the deformation field in areas where the field changes discontinuously, is inefficient because it would require a high number of parameters, to obtain an acceptable accuracy. We therefore explore alternative representations. The last aspect involves exploiting the smoothness of the respiratory movement over time. A suitable, temporal representation is developed, by enforcing the temporal smoothness where the breathing motion allows for it.

1.3.5 Conclusion

The approach chosen for modelling respiratory motion is based on deformable registration and relies on patient-specific motion data. A 4D CT acquired for treatment planning is used as the basis of the model, and provides the patient-specific anatomy and breathing pattern. Cone-beam projections are used to complement the 4D CT data, to take into account motion variability and provide intrafraction respiratory motion estimation. The use of cone-beam projection data inherently involves 2D-3D deformable registration techniques and several measures were taken to facilitate this challenging motion estimation problem. Respiratory motion is formalized; that is, motion is decomposed and different aspects of respiration are accounted for with adapted spatial and temporal response. B-splines were used for representing the model, due to their flexibility. The degrees of freedom of the motion model are further reduced, by tuning the B-spline representation of respiratory motion.

1.4 Outline of this work

In the following chapters we will provide our contributions to lung motion modelling for radiotherapy. Chapters 2-6 were the subject of submitted articles. These submissions have been included unmodified, but were reformatted to match this work and allow cross-referencing. As a consequence, each of these chapters can be considered independently. While their topics are related, each addresses a specific issue and is accompanied by its own introduction and conclusions. The downside of this approach is that each of the chapters will introduce its own notation and abbreviations, of which some may not be consistent across chapters.

The individual contributions were of course conceived to fulfil the general objectives of this work. We therefore discuss their role in a larger context and clarify the interaction between them in chapter 7. In addition we discuss the limitations of the work and outline some potentially interesting axes of research for the future.

The next chapter describes a contribution of technical nature concerning B-spline interpolation. This computationally expensive process involves the repetition of a large number of basic arithmetic operations. An alternative, more efficient algorithm is presented based on an approximative calculation using a look-up table. Our main contribution to this work, was to extend the technique to free-form deformations based on B-splines. The resulting B-LUT transformations were used throughout this

work.

In chapter 3, the issue of sliding motion during respiration motion is addressed, in the context of deformable registration of lung CT images. The approach presented is a pragmatic one and consists in extracting a mask, dividing the thorax where sliding occurs. Use of the resulting motion masks, renders motion estimation and representation more accurate and efficient. The method for computing the mask was designed to be practical and robust, which should allow its inclusion into clinical practice.

Chapter 4 describes a method for spatio-temporal motion estimation from respiratory-correlated imaging of the thorax. Our principal aim is to improve the robustness of deformable registration for 4D CT, by using a global problem formulation and pursuing a more restrictive parametrization of the 4D transformation. A spatio-temporal deformation model is developed using B-splines, capable of accurately representing breathing motion, and improving robustness to artifacts of subsequent registration.

Chapter 5 is the subject of intrafraction respiratory motion estimation from cone-beam projections. To facilitate the problem, we introduce a patient-specific model built from a previously acquired 4D CT acquisition. The optimization process is rendered more stable, by extracting individual respiratory cycles and motion estimation is performed for the subset of the projections simultaneously. The resulting method comes down to a cycle-by-cycle 3D+T motion estimation from a 2D+T projection sequence.

A limitation of the method described in chapter 5, concerns the inability to correct for large baseline variations that may occur during or between fractions. In response, chapter 6 describes a method for obtaining a static comparison between a reference image of the patient and selected cone-beam projections acquired in the treatment room. The dimensionality of the 2D-3D registration problem is greatly reduced by introducing physiological priors about the type of motion we aim at estimating.

References

A. F. Abdelnour, S. A. Nehmeh, T. Pan, J. L. Humm, P. Vernon, H. Schöder, K. E. Rosenzweig, G. S. Mageras, E. Yorke, S. M. Larson, and Y. E. Erdi. Phase and amplitude binning for 4D-CT imaging. *Phys Med Biol*, 52(12): 3515–3529, Jun 2007.

A. Al-Mayah, J. Moseley, and K. K. Brock. Contact surface and material nonlinearity modeling of human lungs. *Phys Med Biol*, 53(1):305–317, Jan 2008.

M. Ayadi, J. Vandemeulebroucke, S. Hlavacek, V. Boldea, C. Ginestet, and D. Sarrut. Dosimetry on moving organs: static and dynamic dose distributions computed from 4DCT for lung cancer treatment. In *9th Biennial ESTRO Meeting on Physics and Radiation Technology For Clinical Radiotherapy*, volume 84, page S77, 2007.

J. M. Balter, R. K. T. Haken, T. S. Lawrence, K. L. Lam, and J. M. Robertson. Uncertainties in CT-based radiation therapy treatment planning associated with patient breathing. *Int J Radiat Oncol Biol Phys*, 36(1):167–174, Aug 1996.

J. M. Balter, K. L. Lam, C. J. McGinn, T. S. Lawrence, and R. K. T. Haken. Improvement of CT-based treatment-planning models of abdominal targets using static exhale imaging. *Int J Radiat Oncol Biol Phys*, 41(4):939–943, Jul 1998.

J.-P. Bissonnette, K. N. Franks, T. G. Purdie, D. J. Moseley, J.-J. Sonke, D. A. Jaffray, L. A. Dawson, and A. Bezjak. Quantifying interfraction and intrafraction tumor motion in lung stereotactic body radiotherapy using respiration-correlated cone beam computed tomography. *Int J Radiat Oncol Biol Phys*, 75(3):688–695, Nov 2009.

J. M. Blackall, S. Ahmad, M. E. Miquel, J. R. McClelland, D. B. Landau, and D. J. Hawkes. MRI-based measurements of respiratory motion variability and assessment of imaging strategies for radiotherapy planning. *Phys Med Biol*, 51(17):4147–4169, Sep 2006.

C. Blondel, R. Vaillant, G. Malandain, and N. Ayache. 3D tomographic reconstruction of coronary arteries using a precomputed 4D motion field. *Phys Med Biol*, 49(11):2197–2208, Jun 2004.

V. Boldea, G. Sharp, S. B. Jiang, and D. Sarrut. 4D-CT lung motion estimation with deformable registration: Quantification of motion nonlinearity and hysteresis. *Med Phys*, 35, Issue 3:1008–1018, 2008.

P. Boyle and B. Levin. World cancer report 2008. Technical report, World Health OrganIzatIon, International agency for research on Cancer, 2008.

K. K. Brock, M. B. Sharpe, L. A. Dawson, S. M. Kim, and D. A. Jaffray. Accuracy of finite element model-based multi-organ deformable image registration. *Med Phys*, 32(6):1647–1659, Jun 2005.

G. T. Y. Chen, J. H. Kung, and K. P. Beaudette. Artifacts in computed tomography scanning of moving objects. *Semin Radiat Oncol*, 14(1):19–26, Jan 2004.

I. J. Chetty, M. Rosu, N. Tyagi, L. H. Marsh, D. L. McShan, J. M. Balter, B. A. Fraass, and R. K. T. Haken. A fluence convolution method to account for respiratory motion in three-dimensional dose calculations of the liver: a monte carlo study. *Med Phys*, 30(7):1776–1780, Jul 2003.

R. Colgan, J. McClelland, D. McQuaid, P. M. Evans, D. Hawkes, J. Brock, D. Landau, and S. Webb. Planning lung radiotherapy using 4D CT data and a motion model. *Phys Med Biol*, 53(20):5815–5830, Oct 2008.

S. C. Davies, A. L. Hill, R. B. Holmes, M. Halliwell, and P. C. Jackson. Ultrasound quantitation of respiratory organ motion in the upper abdomen. *Br J Radiol*, 67(803):1096–1102, Nov 1994.

K. Ding, J. E. Bayouth, J. M. Buatti, G. E. Christensen, and J. M. Reinhardt. 4DCT-based measurement of changes in pulmonary function following a course of radiation therapy. *Med Phys*, 37(3):1261–1272, Mar 2010.

J. Ehrhardt, R. Werner, A. SchmidtRichberg, B. Schulz, and H. Handels. Generation of a mean motion model of the lung using 4DCT image data. In *Eurographics Workshop on Visual Computing for Biomedicine (2008)*, pages 69–76, 2008.

J. Ehrhardt, A. S. Réne Werner, and H. Handels. Prediction of respiratory motion using a statistical 4D mean motion model. In , *Second International Workshop on Pulmonary Image Analysis*, London, 2009.

E. C. Ford, G. S. Mageras, E. Yorke, and C. C. Ling. Respiration-correlated spiral CT: a method of measuring respiratory-induced anatomic motion for radiation treatment planning. *Med Phys*, 30(1):88–97, Jan 2003.

Y. Fung. A theory of elasticity of the lung. *J. appl. Mech*, 41:814, 1974.

R. George, P. J. Keall, V. R. Kini, S. S. Vedam, V. Ramakrishnan, and R. Mohan. Is the diaphragm motion probability density function normally distributed? *Med Phys*, 32(2):396–404, Feb 2005a.

R. George, S. S. Vedam, T. D. Chung, V. Ramakrishnan, and P. J. Keall. The application of the sinusoidal model to lung cancer patient respiratory motion. *Med Phys*, 32(9):2850–2861, Sep 2005b.

D. P. Gierga, G. T. Y. Chen, J. H. Kung, M. Betke, J. Lombardi, and C. G. Willett. Quantification of respiration-induced abdominal tumor motion and its impact on IMRT dose distributions. *Int J Radiat Oncol Biol Phys*, 58(5): 1584–1595, Apr 2004.

M. Guckenberger, J. Wilbert, J. Meyer, K. Baier, A. Richter, and M. Flentje. Is a single respiratory correlated 4D-CT study sufficient for evaluation of breathing motion? *Int J Radiat Oncol Biol Phys*, 67(5):1352–1359, Apr 2007.

T. Guerrero, G. Zhang, W. Segars, T. Huang, S. Bilton, G. Ibbott, L. Dong, K. Forster, and K. Ping Lin. Elastic image mapping for 4-D dose estimation in thoracic radiotherapy. *Radiat Prot Dosimetry*, 115(1-4):497–502, 2005.

D. A. Jaffray and J. H. Siewerdsen. Cone-beam computed tomography with a flat-panel imager: initial performance characterization. *Med Phys*, 27(6): 1311–1323, Jun 2000.

D. A. Jaffray, J. H. Siewerdsen, J. W. Wong, and A. A. Martinez. Flat-panel cone-beam computed tomography for image-guided radiation therapy. *Int J Radiat Oncol Biol Phys*, 53(5):1337–1349, Aug 2002.

S. Kabus, T. Klinder, K. Murphy, B. van Ginneken, C. Lorenz, and J. P. W. Pluim. Evaluation of 4D-CT lung registration. In *Medical Image Computing and Computer-Assisted Intervention MICCAI 2009*, pages 747–754, 2009.

P. J. Keall, G. Starkschall, H. Shukla, K. M. Forster, V. Ortiz, C. W. Stevens, S. S. Vedam, R. George, T. Guerrero, and R. Mohan. Acquiring 4D thoracic CT scans using a multislice helical method. *Phys Med Biol*, 49(10):2053–2067, May 2004.

P. J. Keall, G. S. Mageras, J. M. Balter, R. S. Emery, K. M. Forster, S. B. Jiang, J. M. Kapatoes, D. A. Low, M. J. Murphy, B. R. Murray, C. R. Ramsey, M. B. V. Herk, S. S. Vedam, J. W. Wong, and E. Yorke. The management of respiratory motion in radiation oncology report of AAPM task group 76. *Med Phys*, 33(10):3874–3900, Oct 2006.

H. D. Kubo and B. C. Hill. Respiration gated radiotherapy treatment: a technical study. *Phys Med Biol*, 41(1):83–91, Jan 1996.

F. J. Lagerwaard, C. J. A. Haasbeek, E. F. Smit, B. J. Slotman, and S. Senan. Outcomes of risk-adapted fractionated stereotactic radiotherapy for stage I non-small-cell lung cancer. *Int J Radiat Oncol Biol Phys*, 70(3):685–692, Mar 2008.

F. Lamare, M. J. L. Carbayo, T. Cresson, G. Kontaxakis, A. Santos, C. C. L. Rest, A. J. Reader, and D. Visvikis. List-mode-based reconstruction for respiratory motion correction in PET using non-rigid body transformations. *Physics in Medicine and Biology*, 52(17):5187, 2007.

T. Li, E. Schreibmann, Y. Yang, and L. Xing. Motion correction for improved target localization with on-board cone-beam computed tomography. *Phys Med Biol*, 51(2):253–267, Jan 2006.

T. Li, A. Koong, and L. Xing. Enhanced 4D cone-beam CT with inter-phase motion model. *Med Phys*, 34(9):3688–3695, Sep 2007.

Y. Long, J. A. Fessler, and J. M. Balter. Accuracy estimation for projection-to-volume targeting during rotational therapy: A feasibility study. *Medical Physics*, 37(6):2480–2490, 2010.

D. A. Low, M. Nystrom, E. Kalinin, P. Parikh, J. F. Dempsey, J. D. Bradley, S. Mutic, S. H. Wahab, T. Islam, G. Christensen, D. G. Politte, and B. R. Whiting. A method for the reconstruction of four-dimensional synchronized CT scans acquired during free breathing. *Med Phys*, 30(6):1254–1263, Jun 2003.

D. A. Low, P. J. Parikh, W. Lu, J. F. Dempsey, S. H. Wahab, J. P. Hubenschmidt, M. M. Nystrom, M. Handoko, and J. D. Bradley. Novel breathing motion model for radiotherapy. *Int J Radiat Oncol Biol Phys*, 63 (3):921–929, Nov 2005.

W. Lu, G. H. Olivera, Q. Chen, M.-L. Chen, and K. J. Ruchala. Automatic re-contouring in 4D radiotherapy. *Phys Med Biol*, 51(5):1077–1099, Mar 2006.

A. E. Lujan, E. W. Larsen, J. M. Balter, and R. K. T. Haken. A method for incorporating organ motion due to breathing into 3D dose calculations. *Med Phys*, 26(5):715–720, May 1999.

G. S. Mageras, A. Pevsner, E. D. Yorke, K. E. Rosenzweig, E. C. Ford, A. Hertanto, S. M. Larson, D. M. Lovelock, Y. E. Erdi, S. A. Nehmeh, J. L. Humm, and C. C. Ling. Measurement of lung tumor motion using respiration-correlated CT. *Int J Radiat Oncol Biol Phys*, 60(3):933–941, Nov 2004.

F. Matthews and J. West. Finite element displacement analysis of a lung. *Journal of Biomechanics*, 5(6):591 – 594, IN7, 595–600, 1972. ISSN 0021-9290.

J. McClelland. *Registration Based Respiratory Motion Models for use in Lung Radiotherapy*. PhD thesis, Centre for Medical Image Computing, University College London, 2008.

J. R. McClelland, J. M. Blackall, S. Tarte, A. C. Chandler, S. Hughes, S. Ahmad, D. B. Landau, and D. J. Hawkes. A continuous 4D motion model from multiple respiratory cycles for use in lung radiotherapy. *Med Phys*, 33(9):3348–3358, Sep 2006.

J. Mead, T. Takishima, and D. Leith. Stress distribution in lungs: a model of pulmonary elasticity. *J Appl Physiol*, 28(5):596–608, May 1970.

V. Mexner, J. W. H. Wolthaus, M. van Herk, E. M. F. Damen, and J.-J. Sonke. Effects of respiration-induced density variations on dose distributions in radiotherapy of lung cancer. *Int J Radiat Oncol Biol Phys*, 74(4):1266–1275, Jul 2009.

T. Neicu, H. Shirato, Y. Seppenwoolde, and S. B. Jiang. Synchronized moving aperture radiation therapy (smart): average tumour trajectory for lung patients. *Phys Med Biol*, 48(5):587–598, Mar 2003.

K. Ø. Noe, B. D. D. Senneville, U. V. Elstrøm, K. Tanderup, and T. S. Sørensen. Acceleration and validation of optical flow based deformable registration for image-guided radiotherapy. *Acta Oncol*, 47(7):1286–1293, 2008.

J. R. Olsen, W. Lu, J. P. Hubenschmidt, M. M. Nystrom, P. Klahr, J. D. Bradley, D. A. Low, and P. J. Parikh. Effect of novel amplitude/phase binning algorithm on commercial four-dimensional computed tomography quality. *Int J Radiat Oncol Biol Phys*, 70(1):243–252, Jan 2008.

T. Pan, T.-Y. Lee, E. Rietzel, and G. T. Y. Chen. 4D-CT imaging of a volume influenced by respiratory motion on multi-slice CT. *Med Phys*, 31(2):333–340, Feb 2004.

D. M. Parkin, F. Bray, J. Ferlay, and P. Pisani. Global cancer statistics, 2002. *CA Cancer J Clin*, 55(2):74–108, 2005.

C. Plathow, S. Ley, C. Fink, M. Puderbach, W. Hosch, A. Schmhl, J. Debus, and H.-U. Kauczor. Analysis of intrathoracic tumor mobility during whole breathing cycle by dynamic MRI. *Int J Radiat Oncol Biol Phys*, 59(4):952–959, Jul 2004.

T. G. Purdie, J.-P. Bissonnette, K. Franks, A. Bezjak, D. Payne, F. Sie, M. B. Sharpe, and D. A. Jaffray. Cone-beam computed tomography for on-line image guidance of lung stereotactic radiotherapy: localization, verification, and intrafraction tumor position. *Int J Radiat Oncol Biol Phys*, 68(1):243–252, May 2007a.

T. G. Purdie, K. N. Franks, A. Bezjak, J. Higgins, D. A. Jaffray, and J. P. Bissonnette. Inter and intra-fraction target localization using volumetric imaging in stereotactic body radiation therapy (SBRT) in the lung. In *Proceedings of the 49th Annual ASTRO Meeting*, 2007b.

S. Rit, D. Sarrut, and L. Desbat. Comparison of analytic and algebraic methods for motion-compensated cone-beam CT reconstruction of the thorax. *IEEE Trans Med Imaging*, Feb 2009a.

S. Rit, J. W. H. Wolthaus, M. van Herk, and J.-J. Sonke. On-the-fly motion-compensated cone-beam CT using an a priori model of the respiratory motion. *Med Phys*, 36(6):2283–2296, Jun 2009b.

S. Rit, M. van Herk, L. Zijp, and J.-J. Sonke. Quantification and impact of the variability of the respiratory motion during radiotherapy. *Submitted to Int J Radiat Oncol Biol Phys*, 2010.

C. S. Ross, D. H. Hussey, E. C. Pennington, W. Stanford, and J. F. Doornbos. Analysis of movement of intrathoracic neoplasms using ultrafast computerized tomography. *Int J Radiat Oncol Biol Phys*, 18(3):671–677, Mar 1990.

D. Ruan, J. A. Fessler, J. M. Balter, and P. J. Keall. Real-time profiling of respiratory motion: baseline drift, frequency variation and fundamental pattern change. *Phys Med Biol*, 54(15):4777–4792, Aug 2009.

D. Rueckert, L. I. Sonoda, C. Hayes, D. L. Hill, M. O. Leach, and D. J. Hawkes. Nonrigid registration using free-form deformations: application to breast MR images. *IEEE Trans Med Imaging*, 18(8):712–721, Aug 1999.

H. Ruppertshofen, S. Kabus, and B. Fischer. Image registration using tensor grids for lung ventilation studies. In *Bildverarbeitung fr die Medizin 2009*, 2009.

H. Ruppertshofen, S. Kabus, and B. Fischer. Tensor grid based image registration with application to ventilation estimation on 4D CT lung data. *Int J Comput Assist Radiol Surg*, Apr 2010.

D. Sarrut, V. Boldea, M. Ayadi, J. Badel, C. Ginestet, S. Clippe, and C. Carrie. Nonrigid registration method to assess reproducibility of breath-holding with ABC in lung cancer. *Int J Radiat Oncol Biol Phys*, 61(2):594–607, Feb 2005.

D. Sarrut, B. Delhay, P.-F. Villard, V. Boldea, M. Beuve, and P. Clarysse. A comparison framework for breathing motion estimation methods from 4-D imaging. *IEEE Trans Med Imaging*, 26(12):1636–1648, Dec 2007.

A. Schmidt-Richberg, J. Ehrhardt, R. Werner, and H. Handels. Slipping objects in image registration: improved motion field estimation with direction-dependent regularization. *Med Image Comput Comput Assist Interv*, 12(Pt 1):755–762, 2009a.

A. Schmidt-Richberg, J. Ehrhardt, R. Werner, and H. Handels. Evaluation and comparison of force terms for the estimation of lung motion by non-linear registration of 4D-CT image data. In *World Congress on Medical Physics and Biomedical Engineering*, volume 12, pages 2128– 2131, Munich, Germany, September 2009b.

J. Seco, G. C. Sharp, Z. Wu, D. Gierga, F. Buettner, and H. Paganetti. Dosimetric impact of motion in free-breathing and gated lung radiotherapy: a 4D monte carlo study of intrafraction and interfraction effects. *Med Phys*, 35(1):356–366, Jan 2008.

W. Segars. *Development and Application of the New Dynamic NURBS-based Cardiac-Torso (NCAT) Phantom.* PhD thesis, The University of North Carolina at Chapel Hill, 2001.

W. Segars and B. Tsui. Study of the efficacy of respiratory gating in myocardial SPECT using the new 4-D NCAT phantom. *Nuclear Science, IEEE Transactions on*, 49(3):675–679, June 2002.

W. Segars, B. Tsui, E. Frey, and E. Fishman. Extension of the 4D NCAT phantom to dynamic X-ray CT simulation. In *Nuclear Science Symposium Conference Record, 2003 IEEE*, volume 5, pages 3195–3199Vol.5, 19-25 Oct. 2003.

Y. Seppenwoolde, H. Shirato, K. Kitamura, S. Shimizu, M. van Herk, J. V. Lebesque, and K. Miyasaka. Precise and real-time measurement of 3D tumor motion in lung due to breathing and heartbeat, measured during radiotherapy. *Int J Radiat Oncol Biol Phys*, 53(4):822–834, Jul 2002.

Y. Seppenwoolde, R. I. Berbeco, S. Nishioka, H. Shirato, and B. Heijmen. Accuracy of tumor motion compensation algorithm from a robotic respiratory tracking system: a simulation study. *Med Phys*, 34(7):2774–2784, Jul 2007.

G. C. Sharp, S. B. Jiang, S. Shimizu, and H. Shirato. Prediction of respiratory tumour motion for real-time image-guided radiotherapy. *Phys Med Biol*, 49 (3):425–440, Feb 2004.

S. Shimizu, H. Shirato, K. Kagei, T. Nishioka, X. Bo, H. Dosaka-Akita, S. Hashimoto, H. Aoyama, K. Tsuchiya, and K. Miyasaka. Impact of respiratory movement on the computed tomographic images of small lung tumors in three-dimensional (3D) radiotherapy. *Int J Radiat Oncol Biol Phys*, 46(5):1127–1133, Mar 2000.

H. Shirato, Y. Seppenwoolde, K. Kitamura, R. Onimura, and S. Shimizu. Intrafractional tumor motion: lung and liver. *Semin Radiat Oncol*, 14(1): 10–18, Jan 2004.

J. Sonke, L. Zijp, P. Remeijer, and M. van Herk. Respiratory correlated cone beam CT. *Med Phys*, 32(4):1176–1186, Apr 2005.

J.-J. Sonke, J. Lebesque, and M. van Herk. Variability of four-dimensional computed tomography patient models. *Int J Radiat Oncol Biol Phys*, 70(2): 590–598, Feb 2008.

F.-C. Su, C. Shi, P. Mavroidis, V. Goytia, R. Crownover, P. Rassiah-Szegedi, and N. Papanikolaou. Assessing four-dimensional radiotherapy planning and respiratory motion-induced dose difference based on biologically effective uniform dose. *Technol Cancer Res Treat*, 8(3):187–200, Jun 2009a.

F.-C. Su, C. Shi, P. Mavroidis, P. Rassiah-Szegedi, and N. Papanikolaou. Evaluation on lung cancer patients' adaptive planning of tomotherapy utilising radiobiological measures and planned adaptive module. *J Radiother Pract*, 8: 185–194, Jan 2009b.

R. D. Timmerman, B. D. Kavanagh, L. C. Cho, L. Papiez, and L. Xing. Stereotactic body radiation therapy in multiple organ sites. *J Clin Oncol*, 25(8):947–952, Mar 2007.

C. Vaman, D. Staub, J. Williamson, and M. Murphy. A method to estimate 4DCT deformable registration errors via principal components analysis. In *Medical Physics suppl*, volume 36 of *6*, pages 2821–2821. AAPM, 2009.

M. van Herk. Errors and margins in radiotherapy. *Semin Radiat Oncol*, 14(1): 52–64, Jan 2004.

M. van Herk, M. Witte, J. van der Geer, C. Schneider, and J. V. Lebesque. Biologic and physical fractionation effects of random geometric errors. *Int J Radiat Oncol Biol Phys*, 57(5):1460–1471, Dec 2003.

J. Vandemeulebroucke, D. Sarrut, and P. Clarysse. The POPI-model, a point-validated pixel-based breathing thorax model. In *XVth International Conference on the Use of Computers in Radiation Therapy, ICCR*, 2007.

J. Vandemeulebroucke, O. Bernard, J. Kybic, P. Clarysse, and D. Sarrut. Automatic motion mask extraction for deformable registration of the lungs. In *XVIth International Conference on the Use of Computers in Radiation Therapy*, Amsterdam, June 2010.

D. Vawter, Y. Fung, and J. West. Constitutive equation of lung tissue elasticity. *J. Biomech. Eng*, 101:3845, 1979.

D. L. Vawter. A finite element model for macroscopic deformation of the lung. *J Biomech Eng*, 102(1):1–7, Feb 1980.

S. S. Vedam, P. J. Keall, V. R. Kini, and R. Mohan. Determining parameters for respiration-gated radiotherapy. *Med Phys*, 28(10):2139–2146, Oct 2001.

S. S. Vedam, P. J. Keall, V. R. Kini, H. Mostafavi, H. P. Shukla, and R. Mohan. Acquiring a four-dimensional computed tomography dataset using an external respiratory signal. *Phys Med Biol*, 48(1):45–62, Jan 2003.

P.-F. Villard, M. Beuve, B. Shariat, V. Baudet, and F. Jaillet. Simulation of lung behaviour with finite elements: Influence of bio-mechanical parameters. In *Proceedings of the Third International Conference on Medical Information VisualisationBiomedical Visualisation, MediVis*, page 914, 2005.

M. von Siebenthal, G. Székely, U. Gamper, P. Boesiger, A. Lomax, and P. Cattin. 4D MR imaging of respiratory organ motion and its variability. *Phys Med Biol*, 52(6):1547–1564, Mar 2007.

R. Werner, J. Ehrhardt, R. Schmidt, and H. Handels. Patient-specific finite element modeling of respiratory lung motion using 4D CT image data. *Med Phys*, 36(5):1500–1511, May 2009a.

R. Werner, J. Ehrhardt, A. Schmidt-Richberg, and H. Handels. Validation and comparison of a biophysical modeling approach and non- linear registration for estimation of lung motion fields in thoracic 4D CT data. In *Proceedings of SPIE- The International Society for Optical Engineering*, volume 7259, Februari 2009b.

J. B. West and F. L. Matthews. Stresses, strains, and surface pressures in the lung caused by its weight. *J Appl Physiol*, 32(3):332–345, Mar 1972.

R. D. Wilde, J. Clment, J. M. Hellemans, M. Decramer, M. Demedts, R. Boving, and K. P. V. de Woestijne. Model of elasticity of the human lung. *J Appl Physiol*, 51(2):254–261, Aug 1981.

N. Wink, C. Panknin, and T. D. Solberg. Phase versus amplitude sorting of 4D-CT data. *J Appl Clin Med Phys*, 7(1):77–85, 2006.

J. W. Wolthaus, J.-J. Sonke, M. van Herk, J. S. Belderbos, M. M. Rossi, J. V. Lebesque, and E. M. Damen. Comparison of different strategies to use four-dimensional computed tomography in treatment planning for lung cancer patients. *Int J Radiat Oncol Biol Phys*, Volume 70(Issue 4, 15):Pages 1229–1238, March 2008a.

J. W. H. Wolthaus, J. J. Sonke, M. van Herk, and E. M. F. Damen. Reconstruction of a time-averaged midposition CT scan for radiotherapy planning of lung cancer patients using deformable registration. *Med Phys*, 35(9):3998–4011, Sep 2008b.

H. Wu, G. C. Sharp, B. Salzberg, D. Kaeli, H. Shirato, and S. B. Jiang. A finite state model for respiratory motion analysis in image guided radiation therapy. *Phys Med Biol*, 49(23):5357–5372, Dec 2004.

H. Wu, G. C. Sharp, Q. Zhao, H. Shirato, and S. B. Jiang. Statistical analysis and correlation discovery of tumor respiratory motion. *Phys Med Biol*, 52(16): 4761–4774, Aug 2007.

Z. Wu, E. Rietzel, V. Boldea, D. Sarrut, and G. C. Sharp. Evaluation of deformable registration of patient lung 4DCT with subanatomical region segmentations. *Med Phys*, 35(2):775–781, Feb 2008.

T. Yamamoto, U. Langner, B. W. Loo, J. Shen, and P. J. Keall. Retrospective analysis of artifacts in four-dimensional CT images of 50 abdominal and thoracic radiotherapy patients. *Int J Radiat Oncol Biol Phys*, 72(4):1250–1258, Nov 2008.

D. Yang, W. Lu, D. A. Low, J. O. Deasy, A. J. Hope, and I. E. Naqa. 4D-CT motion estimation using deformable image registration and 5D respiratory motion modeling. *Med Phys*, 35(10):4577–4590, Oct 2008.

R. Zeng, J. A. Fessler, and J. M. Balter. Respiratory motion estimation from slowly rotating X-ray projections: theory and simulation. *Med Phys*, 32(4): 984–991, Apr 2005.

R. Zeng, J. A. Fessler, and J. M. Balter. Estimating 3-D respiratory motion from orbiting views by tomographic image registration. *IEEE Trans Med Imaging*, 26(2):153–163, Feb 2007.

Q. Zhang, A. Pevsner, A. Hertanto, Y.-C. Hu, K. E. Rosenzweig, C. C. Ling, and G. S. Mageras. A patient-specific respiratory model of anatomical motion for radiation treatment planning. *Med Phys*, 34(12):4772–4781, Dec 2007.

T. Zhang, N. P. Orton, T. R. Mackie, and B. R. Paliwal. Technical note: A novel boundary condition using contact elements for finite element based deformable image registration. *Med Phys*, 31(9):2412–2415, Sep 2004.

T. Zhao, W. Lu, D. Yang, S. Mutic, C. E. Noel, P. J. Parikh, J. D. Bradley, and D. A. Low. Characterization of free breathing patterns with 5D lung motion model. *Med Phys*, 36:5183–5189, November 2009.

L. Zijp, J. Sonke, and M. van Herk. Extraction of the respiratory signal from sequential thorax cone-beam X-ray images. In *14th International Conference on the Use of Computers in Radiation Therapy, Seoul, Korea*, May 2004.

2

B-LUT: Fast and Low Memory B-spline Image Interpolation

David Sarrut[1,2], **Jef Vandemeulebroucke**[1,2,3]

[1]CREATIS, CNRS UMR5220, INSA-Lyon, University of Lyon, France

[2]Léon Bérard Cancer Center, University of Lyon, Lyon, France

[3]Center for Machine Perception, Czech Technical University in Prague, Czech Republic

Published in Computer Methods and Programs in Biomedicine in August 2010

Abstract We propose a fast alternative to B-splines in image processing based on an approximate calculation using precomputed B-spline weights. During B-spline indirect transformation, these weights are efficiently retrieved in a nearest-neighbour fashion from a look-up table, greatly reducing overall computation time. Depending on the application, calculating a B-spline using a look-up table, called B-LUT, will result in an exact or approximate B-spline calculation. In case of the latter the obtained accuracy can be controlled by the user. The method is applicable to a wide range of B-spline applications and has very low memory requirements compared to other proposed accelerations. The performance of the proposed B-LUTs was compared to conventional B-splines as implemented in the popular ITK toolkit for the general case of image intensity interpolation. Experiments illustrated that highly accurate B-spline approximation can be obtained all while computation time is reduced with a factor of 5 to 6. The B-LUT source code, compatible with the ITK toolkit, has been made freely available

Contents

2.1 Introduction

B-splines are widely used in image processing for manipulating a continuous version of a discrete image (Unser, 1999). Using B-splines, an n-dimensional (nD) image (or signal) can be represented through a set of nD coefficients. Obtaining the image value at any continuous coordinate involves a linear combination of coefficients and basis function (B-spline) weights. Thanks to its compact support, this involves only a finite and usually small number of coefficients.

Considering the case of B-spline interpolation, two processes can be distinguished. The first one is referred to as the *direct transformation* and consists in computing a set of B-spline coefficients from the initial image. Very efficient digital filtering schemes have been proposed (Unser et al., 1993a,b) to solve this issue. The second process, called *indirect transformation* consists in combining the found coefficients and weights for a given position. This latter process remains relatively slow. For example, performing a rotation of a three dimensional (3D) image with size $512 \times 512 \times 200$ (≈ 50 million voxels) using cubic B-spline interpolation takes about 200s. The computation of coefficients (the direct transformation) only takes about 10s (both performed on a 2GHz PC, using the ITK toolkit (Ibanez et al., 2005), see section 2.3).

To our knowledge, few studies directly address the indirect computational time issue. Acceleration of processes which include B-spline interpolation, such as deformable image registration, are generally addressed in a parallel framework with hardware based methods: with clusters of workstations (Inoa et al., 2005,), with multi-processors shared-memory systems (Aylward et al., 2007), or with graphical processing units or GPU's (Sharp et al., 2007; Modat et al., 2009). Some authors (Meijering et al., 2001) mentioned the use of precomputed weights, but we do not find any publication describing such work.

The computational cost of the indirect transformation is caused by the high number of operations performed for each interpolated value. For simplicity we will assume in the following that the same spline degree was chosen along all dimensions. Observations can however easily be extended to the general case.

During the first step of the indirect transformation we compute the tensor products of the B-spline basis function values according to the distance between the current position and each contributing control point

in the support region (Equation 2.1).

$$\text{Step 1} \qquad \boldsymbol{\beta}_i^r(x) = \prod_j^d \beta^r(p_{ij} - x_j)\,. \tag{2.1}$$

β^r is the B-spline basis function of degree r, d is the image dimension, i is the index of a control point with coordinates p_{ij}, x is the position at which we want to evaluate the function and x_j are its coordinates. For a given position x, $(r+1)^d$ different tensor products are computed, one for each control point with non-zero weight at x.

The second step required to compute the interpolated value $v(x)$ involves the linear combination of the tensor products ($\boldsymbol{\beta}_i^r$) with the corresponding coefficients c_i, previously computed during the direct transformation (Equation 2.2). In the following the term weights will refer exclusively to the B-spline tensor products $\boldsymbol{\beta}_i^r$.

$$\text{Step 2} \qquad v(x) = \sum_i^{(r+1)^d} c_i\, \boldsymbol{\beta}_i^r(x)\,. \tag{2.2}$$

Evaluating the basis function $\beta^r(e)$ involves the computation of a polynomial of degree r. The initial definition of the B-spline functions is obtained recursively by convolving β^0 $(n+1)$ times with itself. An analytic expression can also be obtained by applying the recursive Cox-de Boor formula (Equation 2.3).

$$\boldsymbol{\beta}^r(e) = \boldsymbol{u}\boldsymbol{M} \text{ with } \begin{cases} \boldsymbol{u} = \left[e^r\ e^{r-1}\ ...\ e\ 1\right] \\ \boldsymbol{M} \text{ matrix of size } k \times k \text{ with } k = r+1 \end{cases} \tag{2.3}$$

$$\boldsymbol{M} = [M_{ij}] = \left[\frac{1}{(k-1)!} C_{k-1,i} \sum_{m=j}^{k-1} (k-(m+1))^i\, (-1)^{m-j}\, C_{k,m-j} \right] \tag{2.4}$$

$$C_{i,j} = \frac{i!}{j!(i-j)!} = \text{binomial coefficient} \tag{2.5}$$

Step 1 requires about $2 \times r$ operations (additions or multiplications) for computing one β^r, thus $2 \times r \times d$ for the tensor product $\boldsymbol{\beta}^r$. There are $(r+1)^d$ different weights. This leads to a total complexity of $O(r \times d \times (r+1)^d)$ operations for step 1, while only $O((r+1)^d)$ for step 2.

If the interpolation is performed with a regular sampling rate which is a multiple of the control point spacing, the required weights will reoccur across the image region due to symmetry. In this case they can be precomputed, stored and reused, allowing to avoid most of the computational part of step 1, without any loss of accuracy. However, as generally this is not the case (e.g. when performing an image rotation or during image warping), the exact weights cannot be precomputed.

We propose to extend the range of applications for which splines can be efficiently calculated using precomputed weights. For applications where no exact calculation can be achieved the approximation error is controlled by oversampling the control point grid. Through efficient design of the weights look-up table (LUT), memory requirements are kept to a minimum further extending the use of the method to large scale problems. As we will show in section 2.4, the proposed B-LUT framework can obtain high interpolation accuracy while offering considerable reduction in computation time.

2.2 Method

The method consists in approximating the tensor product (Equation 2.1) by a precomputed one. At interpolation time, step 1 is replaced by finding the closest precomputed weights in the LUT. Step 2 can then be applied in a conventional way by looping over the coefficients and their corresponding weights.

2.2.1 LUT Computation

The computation of the weights is made only once before the interpolation. By choosing the (*over*)sampling rate of the precomputed weights with respect to the control point grid, it is possible to control the trade-off between LUT size and approximation accuracy. Note that the whole image region does not need to be sampled. Since we are assuming uniform B-splines, it suffices to sample one n-dimensional B-spline support.

Let $\lambda_j \in \mathbb{N}$ be the LUT sampling rate for the dimension j. The size of the LUT is the size of the B-spline support, $(r+1)^d$, multiplied by the sampling rate in each dimension $\prod_j^d \lambda_j$. The overall computation time of interpolating an entire image once can only be reduced if the number of weights to precompute is less than $(r+1)^d$ times the number of pixels to interpolate. In practice however, this is often the case. For example, to interpolate a 256^3 3D image having about 1.6×10^7 pixels, the number

of weights to precompute for a sampling rate equal to 20 is 5.12×10^5 ($20^3 \times (3+1)^3$)), in comparison to 1.024×10^9 ($16 \times 10^6 \times (3+1)^3$) weights in total. Assuming single precision, the LUT memory size requirement is $4\,bytes \times (r+1)^d \times \prod_j^d \lambda_j$, which leads to 2MB in this case.

2.2.2 LUT Look-Up

After computing the weights, step 1 in Equation 2.1 is replaced by finding the optimal precomputed weight in the LUT. The interpolation position x is then transformed to its corresponding position x' relative to the sampled B-spline support region.

For efficiency, the LUT is indexed such that a single rounding operation, denoted $\lfloor a \rceil$, on each of the coordinates of x' leads to the index in the LUT l of the first element of the list of all $(r+1)^d$ weights corresponding to the current position, see Equation 2.6. This implies that for each evaluation position a single look-up replaces step 1, providing all the weights required for the calculation in step 2 (Equation 2.2).

$$l = \sum_{j=1}^{d} \left(k_j \prod_{i}^{j} \lambda_{i-1} \right) \quad \text{with} \quad k_j = \lfloor x'_j \rceil \quad \text{and} \quad \lambda_0 = 1 \tag{2.6}$$

2.3 Design Considerations

We implemented the method inside the Insight Segmentation and Registration Toolkit (ITK [1] (Ibanez et al., 2005)). This toolkit is widely used in medical image analysis and uses the notion of filters to represent a process chain. A new filter was created named `BSplineInterpolateImageFunctionWithLUT` which inherits from the original `BSplineInterpolateImageFunction`. This way, users only have to change three lines inside their usual code to use B-LUTs instead of B-splines. The code and procedure are available on the following web page

`http://www.creatis.insa-lyon.fr/rio/b-lut`

under the CeCILL open source license [2].

1. `http://www.itk.org`
2. `http://www.cecill.info/index.en.html`

2.4 Experiments

In this work the performance of the proposed B-LUTs is assessed in the context of image intensity interpolation. Similar results can be expected in other application areas (see Section 2.5 for an example on deformable image registration). In addition to a quantitative accuracy evaluation, we provide an analysis of the time gain over conventional B-splines. The latter should be considered as an example as the obtained gain was found to be highly dependent on the computer architecture.

2.4.1 B-LUT Interpolation Accuracy

In order to illustrate the inherent loss of accuracy caused by the use of approximated weights, we performed the following tests, inspired from (Meijering et al., 2001). A 3D image was rotated several times around an arbitrary axis with a series of 16 different angles [3], resulting in a complete rotation of 360°. This procedure provides us with a gold standard to compare the rotated image with: the original image. Moreover, the image is used at its intrinsic resolution and the use of different rotation angles allows to avoid bias due to precomputed weight positions.

The test images were two CT images, the first of the head and the second of the lungs and heart. Their respective sizes were $512 \times 512 \times 222$ and $512 \times 512 \times 403$, and their voxel sizes $0.5 \times 0.5 \times 1$ and $0.4 \times 0.4 \times 0.3$. The used images therefore contained about 58 and 105 million voxels respectively. Experiments were performed for B-spline degrees from linear (r=1) to quintic (r=5), including the popular cubic B-splines (r=3). For each degree, we tested different LUT sampling values (λ equal to 1, 2, 4, 5, 10, 20 and 50 for each image dimension). The rotated image when using B-LUT interpolation was compared to the one obtained with B-spline interpolation and to the original reference image. Differences were quantified by computing the Root Mean Squared Error (RMSE) and the maximum difference (MAX). Pixels that go out of the image support during the rotation are discarded and thus not counted into the RMSE final values, by using a binary image mask.

Table 2.1 summarizes the results for the consecutive rotation experiment described above. In the first two tables we assess the accuracy of the B-LUT interpolation with respect to the conventional B-spline method, while in the following two tables a comparison with the original

3. Angles were 0.7, 3.2, 6.5, 9.3, 12.1, 15.2, 18.4, 21.3, 23.7, 26.6, 29.8, 32.9, 35.7, 38.5, 41.8 an 44.3 degrees.

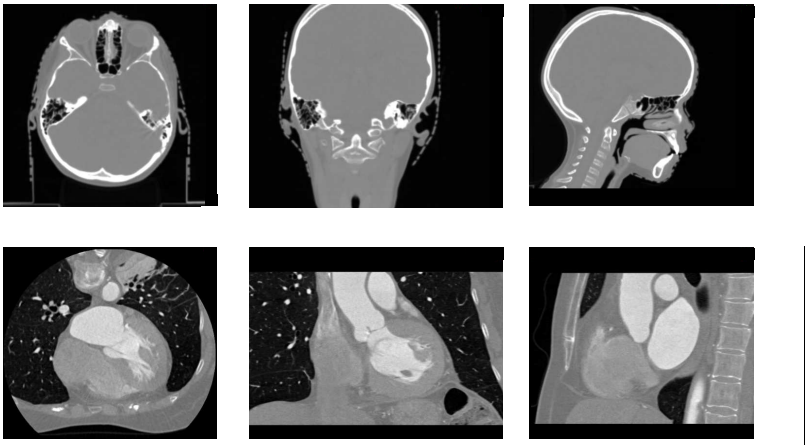

Figure 2.1: The two images used for the tests : a CT image of a head (top) and a CT image of heart/thorax (bottom).

reference image is performed. Figure 2.2 displays RMSE between the two methods (the RMSE axis is logarithmic) for the first image (similar results were obtained for the second). The figure 2.3 illustrates the resulting images with the first test image.

A sampling equal to λ means that the distance between the position used to compute the approximated weight and the position of the real weight is at maximum $\frac{1}{2\lambda}$ (half the distance between two samples). In order to illustrate the intrinsic error of the method, we compute RMSE between an image and the same image displaced by such maximum distance. The figure 2.5 displays the values for cubic B-splines computed with a 2D slice.

2.4.2 B-LUT Interpolation Efficiency

We performed time measurements for both B-LUT and B-spline interpolation. Tests were performed on the previously described 3D images for a rotation transformation. We observed computation time variations when successive interpolations were performed due to processor cache effects. Times were thus measured for ten different transformations and averaged. The figure 2.6 displays the mean computation time of image 1 test, for interpolations with different B-spline degrees (from

RMSE (and MAX) error of BLUT according to conventional Bspline

		λ=1	λ=2	λ=4	λ=5	λ=10	λ=20	λ=50
Linear	r=1	133 (3679)	23 (702)	9 (276)	7 (190)	3 (91)	1 (40)	1 (14)
Quadratic	r=2	138 (4156)	48 (1805)	21 (862)	17 (700)	8 (328)	4 (149)	2 (63)
Cubic	r=3	140 (4216)	53 (2038)	23 (944)	18 (738)	9 (369)	4 (187)	2 (69)
Quartic	r=4	142 (4351)	59 (2422)	26 (1143)	21 (882)	10 (465)	5 (232)	2 (88)
Quintic	r=5	143 (4356)	61 (2635)	28 (1219)	22 (922)	11 (503)	5 (256)	2 (96)

RMSE (and MAX) error according to original image

		λ=1	λ=2	λ=4	λ=5	λ=10	λ=20	λ=50	Ref
Linear	r=1	144 (3982)	87 (3059)	89 (3062)	89 (3077)	90 (3105)	90 (3104)	90 (3104)	90 (3102)
Quadratic	r=2	144 (3982)	57 (2933)	33 (1887)	29 (1889)	24 (1593)	23 (1616)	22 (1536)	22 (1542)
Cubic	r=3	144 (3982)	58 (3027)	30 (1840)	26 (1725)	20 (1465)	18 (1484)	17 (1386)	17 (1396)
Quartic	r=4	144 (3982)	61 (3122)	30 (1772)	25 (1600)	17 (1330)	14 (1349)	13 (1216)	13 (1252)
Quintic	r=5	144 (3982)	63 (3168)	31 (1781)	25 (1571)	16 (1281)	13 (1302)	12 (1162)	12 (1206)

RMSE (and MAX) error of BLUT according to conventional Bspline

		λ=1	λ=2	λ=4	λ=5	λ=10	λ=20	λ=50
Linear	r=1	91 (2517)	16 (382)	6 (188)	5 (120)	2 (70)	1 (28)	0 (12)
Quadratic	r=2	94 (2884)	31 (946)	15 (461)	12 (408)	5 (183)	3 (88)	1 (41)
Cubic	r=3	95 (2878)	33 (1084)	16 (474)	13 (419)	6 (196)	3 (98)	1 (44)
Quartic	r=4	96 (2872)	37 (1254)	19 (574)	15 (513)	7 (236)	4 (109)	1 (50)
Quintic	r=5	96 (2870)	39 (1330)	20 (630)	15 (562)	7 (259)	4 (115)	1 (52)

RMSE (and MAX) error according to original image

		λ=1	λ=2	λ=4	λ=5	λ=10	λ=20	λ=50	Ref
Linear	r=1	97 (2848)	55 (1154)	56 (1008)	56 (1069)	56 (1053)	56 (1051)	56 (1054)	56 (1054)
Quadratic	r=2	97 (2848)	36 (984)	23 (519)	20 (480)	17 (306)	16 (266)	16 (272)	16 (267)
Cubic	r=3	97 (2848)	37 (1087)	22 (508)	19 (471)	15 (269)	14 (224)	13 (221)	13 (213)
Quartic	r=4	97 (2848)	39 (1211)	22 (565)	18 (477)	13 (283)	11 (189)	11 (167)	11 (162)
Quintic	r=5	97 (2848)	40 (1279)	22 (620)	19 (526)	12 (288)	11 (176)	10 (146)	10 (143)

Table 2.1: (Top) RMSE and maximum error (MAX) between fast B-LUT and conventional B-spline. (Bottom) RMSE between reference image without rotation and images rotated by 360° with sampled (λ from 1 to 50) and conventional (denoted by 'Ref') B-spline interpolations.

linear to quintic), for conventional B-spline interpolation and fast B-LUT interpolation with two sampling rates ($\lambda = 10$ and $\lambda = 20$). We also indicate the time due to coefficient computation (boxes at the bottom). The machine was an Intel Core 2 Duo 2.0 GHz. Figure 2.7 illustrates the loss of efficiency when increasing the LUT size for cubic B-LUT interpolation.

2.5 Discussion

Figure 2.2 and table 2.1 show that, with a sampling rate λ greater than 10, the difference between images interpolated with conventional B-splines and B-LUT is very low (visually they are indistinguishable in all tests). The mean of absolute differences was found to be less than 3 Hounsfield units for cubic B-splines with $\lambda = 10$ or 2 with $\lambda = 20$. For lower sampling rates, the approximation became insufficient. For example, cubic B-LUT

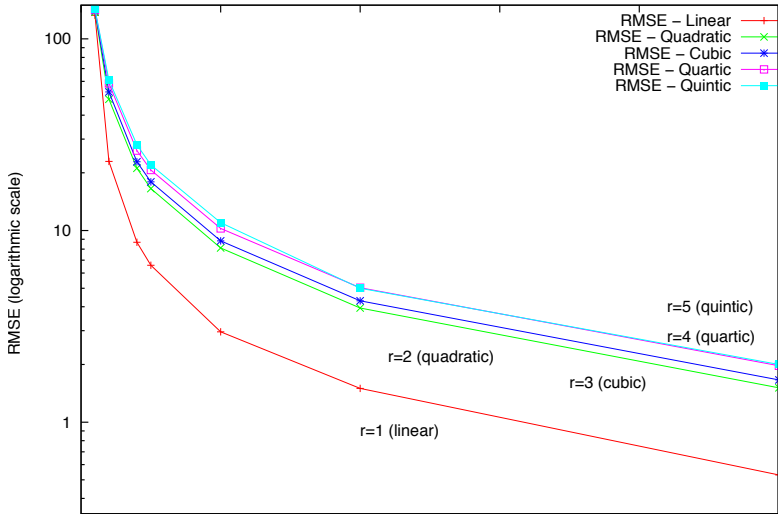

Figure 2.2: RMSE between an image rotated with fast B-LUT and image rotated with corresponding conventional B-splines, for various degrees and sampling values. The RMSE axis is logarithmic scaled.

with $\lambda = 5$ performed worse than conventional quadratic B-spline. We also observed that the differences increased with spline degree.

Figure 2.6 illustrates the important time gain that can be obtained using B-LUTs. For equivalent B-spline degrees the time is reduced by a factor between 5 (quadratic) and 6 (quintic). It can be seen that quintic B-LUT interpolation was more than twice as fast than conventional cubic B-spline interpolation. For linear interpolation, computational time was greater (factor 1.15) than conventional linear interpolation and we thus do not recommend to use the LUT method for a degree lower than 2. However, it should be mentioned that identical tests performed on a different computer architecture (AMD Athlon(tm) 64bits 2GHz) gave different results. For degrees 2 up to 5 similar though slightly lower speed-up factors between 4 to 5 were found. For linear interpolation a speed-up greater than 3 was in this case also observed. Such differences could be due to the processor cache size (2MB for Intel and 512kB for AMD), and specific handling of specific arithmetic operations. Finally we also draw the reader's attention to the time required for coefficients computation (direct transformation process using recursive filters) which is negligible compared to the time needed by the interpolation.

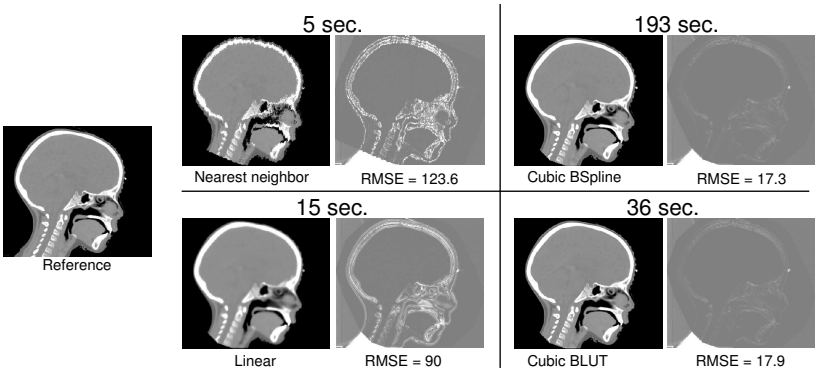

Figure 2.3: The images show the results of the application of 16 successive rotations around an arbitrary axis (360°), with different interpolation methods. Numbers are RMSE errors and computational time of one rotation in seconds (PC 2GHz). Initial image is $512 \times 512 \times 222$ pixels.

The influence of the LUT size on the computational time, controlled by the sampling factor λ is illustrated in Figure 2.7. For λ less than or equal to 20, the time is almost unchanged. For $\lambda = 10$ a light speed-up compared to lower λ values was observed, but this is probably due to processor cache effect. Raising λ to 100 increased the computational time by 30 %, but the whole computational time remains largely lower than the conventional implementation.

An important parameter when choosing an adequate value for the sampling factor λ is the relative density of pixels to be interpolated with respect to the B-spline control point grid d_r. In the presented experiments, d_r was equal to 1. When there are fewer control points than interpolated values ($d_r > 1$), the sampling rate should be increased accordingly to maintain the same level of accuracy. The results presented here should thus be interpreted as guidelines for choosing the *relative* sampling factor $\lambda_r = \frac{\lambda}{d_r}$. More explicitly, one can expect to obtain an accuracy corresponding to the measurements presented in Figure 2.2 for sampling factor λ_r, when choosing the sampling factor λ such that $\lambda = d_r \lambda_r$. The computational efficiency shown in Figure 2.7, will depend however on the actual LUT size, and so on the choice of λ.

The general application of image intensity interpolation was addressed in this work. The proposed B-LUT framework is however applicable in all areas where B-splines are used. A particular example is the case

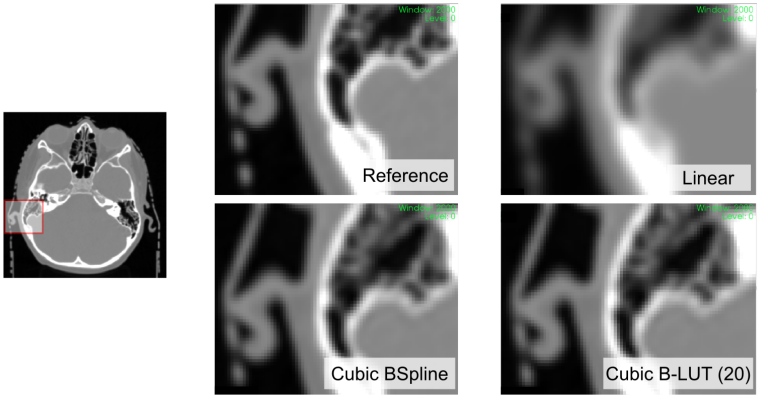

Figure 2.4: The images focus on a small area having important grey value gradients (bone, soft tissues, air) in order to compare the reference image to the interpolated ones with linear, cubic B-splines and cubic B-LUT (with 20 as sample rate) interpolations.

of deformable image registration using free form deformations (Rueckert et al., 1999) (FFD) where B-splines are used to represent the sought spatial transform. The optimization of the transform is usually done iteratively, requiring one image to be repeatedly transformed in order to evaluate the current solution. During each iteration the splines representing the transform will be evaluated at the same positions (the voxel positions of the reference image). Their corresponding tensor products can be computed once and reused in further iterations, providing considerable acceleration at run-time. Such an approach has been implemented in the optimized registration framework of the ITK toolkit (Aylward et al., 2007), available in the ITK *Review* section. The B-spline weights corresponding to *all* considered reference image voxels are precomputed and stored. The memory requirements of this approach (about $(r+1)^d$ times the image memory size in double precision) become very quickly prohibitive, rendering it impossible to run the method for reasonably sized images. To remedy this, we implemented a B-LUT FFD, in which the B-spline spatial transform was replaced by a B-LUT spatial transform. Contrary to the previous approach, the B-LUT deformable registration, requires only one n-dimensional B-spline support region to be sampled and stored. By careful choice of the sampling factor, the B-LUT FFD yields an exact B-spline representation.

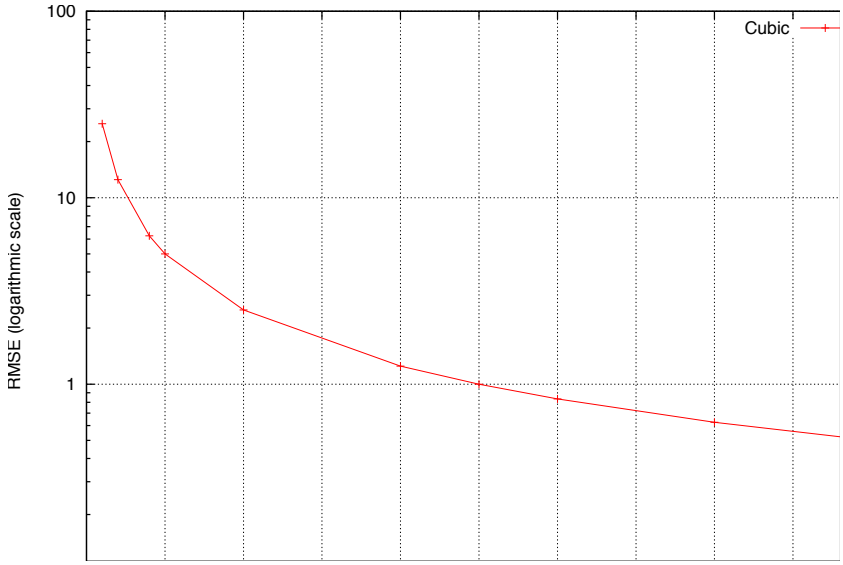

Figure 2.5: RMSE between an image and a translation of the maximum amount of error ($\frac{1}{2\lambda}$) for cubic B-spline interpolation.

We compared the optimized ITK B-spline FFD registration method to the B-LUT FFD registration method. Note however that this comparison does not just assess the impact of caching all the B-spline weights with respect to the use of a compact LUT. This because several acceleration mechanisms are included in the optimized ITK B-spline FFD, also affecting the calculation of the Jacobian of the transform and the derivative of the cost function. These mechanisms were difficult and even in some cases impossible to reproduce in the case of the B-LUT FFD.

We ran both registration methods on image pairs which have 128^3 voxels. We placed 10 control points along each dimension (7 control points inside the image region placed every 20 voxels, 3 control points for the required border of the cubic splines), making a total of 1000 control points and parameters to optimize. In case of the B-LUT FFD, we set the sampling factor to 20 along each dimension, obtaining an exact B-spline representation. We ran both methods for 50 iterations on a single thread and recorded the CPU occupation time and memory consumption. In case of the B-spline FFD the method required 30 min and occupied more than 2.7 GB, while conventional B-spline FFD, without optimization takes more

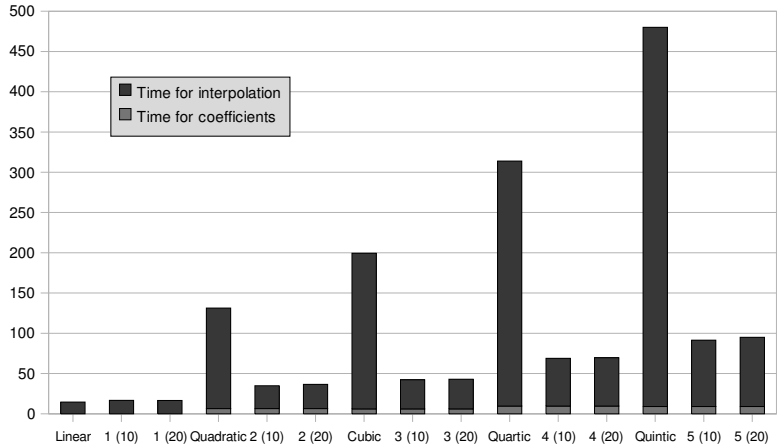

Figure 2.6: Time (in seconds) for different B-spline interpolations: from linear ($r = 1$) to quintic ($r = 5$) degree, with conventional method and fast methods ($\lambda = 10$ and $\lambda = 20$).

FFD Methods	Computation time	Memory requirement
Conv. B-Spline	73 min	578 MB
Opt. B-Spline "Opt"	30 min	2721 MB
B-LUT	17 min	597 MB

Table 2.2: Computation time and memory requirement for FFD registration with conventional B-spline, optimized B-spline and the proposed B-LUT method.

than twice the time and about 578MB. The B-LUT FFD finished in only 17 min and requiring 597MB, only 3% more memory (see table 2.2). Tests on 256^3 image pairs could not be performed as the B-spline FFD memory requirements exceeded the 8GB of RAM on the host machine. The B-LUT FFD reported a memory consumption below 2GB. As mentioned before, these measurements should be interpreted as indicators of relative performance as the obtained performance may differ on other architectures or for different parameters.

2.6 Conclusion

We proposed a method to accelerate B-spline interpolation using look-up tables of precomputed B-spline tensor products. Depending on the

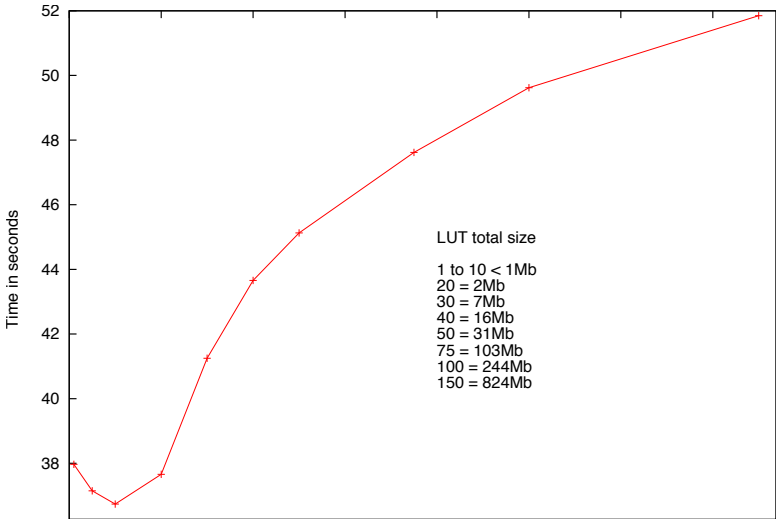

Figure 2.7: Computation time for one rotation of the 3D test image with cubic interpolation and several sampling values, from $\lambda = 1$ to $\lambda = 150$. Total sizes of the LUT for the different sampling λ are indicated in MB.

application, the resulting interpolation will be exact or approximate in which case the accuracy of the B-spline approximation is fully controllable by the user, by varying the sampling factor λ. We obtained speed-up factors between 5 to 6 compared to conventional method from quadratic to quintic interpolation, with a very low error. Attention should be given to the relative density of interpolated values with respect to the density of control points when choosing the sampling factor. For applications where the density of the samples is comparable to the density of control points, we recommend using $\lambda = 20$, offering a good compromise. For other relative densities, λ should be changed accordingly to maintain the same accuracy of approximation. In the future, this method could be used together with hardware-based acceleration with GPU (Sharp et al., 2007) to speed up the processing of time critical applications even more.

Acknowledgement

Jef Vandemeulebroucke was funded by the EC Marie Curie grant WARTHE.

References

S. Aylward, J. Jomier, S. Barre, B. Davis, and L. Ibanez. Optimizing ITK registration methods for multi-processor, shared-memory systems,. *Insight Journal*, http://hdl.handle.net/1926/566, 2007.

L. Ibanez, W. Schroeder, L. Ng, and J. Cates. *The ITK Software Guide*. Kitware, Inc. ISBN 1-930934-15-7, http://www.itk.org/ItkSoftwareGuide.pdf, second edition, 2005.

F. Inoa, K. Ooyamab, and K. Hagiharaa. A data distributed parallel algorithm for nonrigid image registration. *Parallel Computing*, 31(1):19–43, 2005,.

E. Meijering, W. Niessen, and M. Viergever. Quantitative evaluation of convolution-based methods for medical image interpolation. *Med Image Anal*, pages 111–126, 2001.

M. Modat, G. R. Ridgway, Z. A. Taylor, M. Lehmann, J. Barnes, D. J. Hawkes, N. C. Fox, and S. Ourselin. Fast free-form deformation using graphics processing units. *Comput Methods Programs Biomed*, page in press, Oct 2009.

D. Rueckert, L. I. Sonoda, C. Hayes, D. L. Hill, M. O. Leach, and D. J. Hawkes. Nonrigid registration using free-form deformations: application to breast MR images. *IEEE Trans Med Imaging*, 18(8):712–721, Aug 1999.

G. C. Sharp, N. Kandasamy, H. Singh, and M. Folkert. GPU-based streaming architectures for fast cone-beam CT image reconstruction and demons deformable registration. *Phys Med Biol*, 52(19):5771–5783, Oct 2007.

M. Unser. Splines: A perfect fit for signal and image processing. *IEEE Signal Processing Magazine*, 16(6):22–38, November 1999.

M. Unser, A. Aldroubi, and M. Eden. B-Spline signal processing: Part I—Theory. *IEEE Transactions on Signal Processing*, 41(2):821–833, February 1993a. IEEE Signal Processing Society's 1995 best paper award.

M. Unser, A. Aldroubi, and M. Eden. B-Spline signal processing: Part II—Efficient design and applications. *IEEE Transactions on Signal Processing*, 41 (2):834–848, February 1993b.

3

A motion mask to preserve sliding in deformable registration of CT images of the lungs

Jef Vandemeulebroucke[1,2,3], Olivier Bernard[1], Jan Kybic[3] and Patrick Clarysse[1] and David Sarrut[1,2]

[1]CREATIS, CNRS UMR5220, INSA-Lyon, University of Lyon, France

[2]Léon Bérard Cancer Center, University of Lyon, Lyon, France

[3]Center for Machine Perception, Czech Technical University in Prague, Czech Republic

Published in Proceedings of the XVIth ICCR, Amsterdam, June 2010

Journal manuscript under preparation

Abstract There is an increasing demand for accurate deformable registration in radiation therapy. These algorithms generally rely on the assumption that the sought spatial transformation is homogeneously smooth, which can contradict the physiology of the studied motion. An example is the sliding motion of the lung with respect to the chest wall during breathing. We propose an original method for automatically dividing the thorax into moving and less-moving regions. The method is based on the level set framework, used to track the evolution of a moving interface, constrained by previously extracted anatomical features and regularized by a strong geometric prior. We show that the obtained motion masks can facilitate deformable registration by providing an interface where sliding motion occurs. Inner and outer thoracic structures are registered separately using free-form deformations based on B-splines and compared to the result when considering the entire thorax simultaneously. By looking at the matching accuracy of a large, well-distributed set of landmarks in the lungs, we found that the mean target registration error improved for all patients and that the improvement was statistically significant for five out of six patients. By preserving the sliding motion, the complexity of the spatial transformation can be reduced considerably while maintaining matching accuracy.

Contents

3.1 Introduction

In radiation therapy, deformable image registration of computed tomography (CT) images of the thorax has been used extensively for a variety of tasks (Sarrut, 2006; Kessler, 2006), including automatic contour propagation (Lu et al., 2006), four dimensional (4D) treatment planning (Keall, 2004), quantification of residual motion in breathhold CT scans (Sarrut et al., 2005), 4D dose estimation (Guerrero et al., 2005), dynamic ventilation imaging (Guerrero et al., 2006), construction of a mid-position reference planning image (Wolthaus et al., 2008), quantification of motion and hysteresis (Boldea et al., 2008), building respiratory motion models (McClelland et al., 2006) and motion-compensated cone-beam reconstruction (Rit et al., 2009).

Medical image registration aims at finding a suitable spatial transformation such that a transformed target image becomes similar to reference image. Deformable image registration is ill-posed making a direct approach impossible (Modersitzki, 2004). Explicit parametric restrictions with respect to the spatial transformation and suitable regularization of the objective function should encode the physical understanding of the desired deformation properties and drive the optimization to solutions with such characteristics. In particular, the assumption of spatial smoothness of the transformation is widely utilized to estimate motion induced deformations. Depending on the registration method, this is accomplished by expressing the transformation with smooth basis functions, by building in smoothness constraints or including regularization in the optimization framework favouring smooth solutions. While required for solving the inverse problem, these mechanisms can contradict the physiology of the organ motion. A particular example is sliding motion, which can be observed in the case of respiratory induced lung or liver motion. Homogeneous smoothing of the transformation will in this case *blur* the estimated transformation across the sliding interface, resulting in locally reduced registration accuracy (Wu et al., 2008; Schmidt-Richberg et al., 2009).

The issue of sliding motion in deformable image registration has been addressed in a number of ways. Recently, preliminary but promising results have been reported for specifically designed regularization schemes. Wolthaus et al. (2008) used tissue dependent filtering for the deformation field, using the density measure from the CT image to differentiate between regions. Motion estimation improved for the lung region, but was still prone to error near the diaphragm and upper abdomen where density is similar to that of the thoracic wall. In (Ruan et al., 2008)

a class of discontinuity preserving regularization schemes was described. Unfortunately these may preserve other undesirable flow singularities. In response, a robust energy functional was proposed (Ruan et al., 2009) to discriminantly preserve large shear. Similarly, Chun et al. (2009) modified an invertibility penalty of the cranio-caudal deformation component to encourage large sliding along that direction.

Alternatively, sliding was addressed by masking the background, based on segmentations of the lung (Werner et al., 2009b) or liver (von Siebenthal et al., 2007), to prevent it from affecting the registration of the studied organ. Rietzel and Chen (2006) described an approach in which the thorax is manually segmented, into moving (lungs, mediastinum and abdomen) and less-moving (the remainder) subregions, and each region is registered separately. Wu et al. (2008) extended the method, introducing a boundary matching criterion that helps eliminate gaps in the deformation field between the separately registered subregions. Regions can be processed simultaneously following Schmidt-Richberg et al. (2009), who modified a diffusive regularization by restricting smoothing of the deformation field to the normal direction with respect to a given segmentation. Their method allows for discontinuities in the motion field in tangential direction (required to preserve sliding motion at the interface), while maintaining continuity in the normal direction (eliminating gaps). Joint segmentation and registration methods have been proposed in other areas (Yezzi et al., 2003; Droske and Rumpf, 2007), but the underlying assumption that motion discontinuity coincides with intensity discontinuity is a limiting factor.

Finally, the issue of sliding motion has been addressed by finite element (Werner et al., 2009a; Al-Mayah et al., 2009) and surface based methods (von Berg et al., 2007; Klinder et al., 2008). These methods allow to explicitly or implicitly incorporate suitable boundary conditions. However, internal information like the bronchial or vessel tree is greatly simplified or discarded which might affect matching accuracy of those structures.

We propose a practical method for automatically dividing the thorax into regions with homologous, respiratory-induced motion. Our main objective is to obtain an accurate interface where strong sliding motion occurs, and facilitate subsequent deformable registration. The obtained *motion mask*, is very similar to the manual segmentations used in (Wu et al., 2008). Similarly, the found interface is subanatomical, i.e. does not necessarily coincide with visible organ boundaries, making validation by comparison with manual delineations by experts difficult. Alternatively,

the suitability of the obtained masks is assessed by applying them to deformable registration of the lungs. Registration using the motion mask is compared to conventional registration of the end-exhalation and end-inhalation frames of 4D CT images of six lung cancer patients. The performance is evaluated by looking at the registration error of a set of 100 landmarks per image pair.

3.2 Method

3.2.1 Motion Mask Extraction

Anatomically (Werner et al., 2009a), each lung is located within a pleural sac which is made up of two membranes called the *pleurae*. The outer parietal pleura is adherent to the internal surface of the thoracic cavity, the diaphragm, and the mediastinum. The inner visceral pleura covers the lung and is adherent to its surface. Both inner and outer pleura join at the root of the lung which is the point of entry of bronchi, vessels, and nerves into the lung. The space enclosed between the pleurae is called the pleural cavity, which is filled with liquid.

During lung ventilation the breathing muscles–mainly the diaphragm and outer intercostal muscles–contract, which forces the thoracic cage and subsequently the lungs to expand. As the lungs expand inside the thorax, sliding can occur between the pleurae, causing a discontinuity in the motion. At the lung-to-mediastinum interface, sliding is limited due to the entry of the vessels, bronchi and nerves. These, along with the heart and other structures in the mediastinum tend to move with the lung, though usually with reduced amplitude. At the interface of the lungs with the chest wall, the pleurae are free to slide with respect to each other. During inhalation the diaphragm descends, forcing the abdomen inferiorly and anteriorly. The inferior, posterior part of the lungs near the diaphragm tends to exhibit the largest sliding. At the anterior side of the lung-to-chest interface, sliding tends to be smaller as the diaphragm is attached to the sternum limiting the extent of motion (Gray, 1918, chapter IV.6.c).

Taking into account these observations, the following considerations apply regarding the sought motion mask. To preserve sliding, an interface should separate the lung from the chest wall. At the medial lung interface, as there is a continuous and smooth transition of motion, the mediastinum can be considered as part of the same region as the lungs–as proposed by Rietzel and Chen (2006). Contrary to the manual segmentations as depicted in Wu et al. (2008, Figure 1), we choose to include the whole

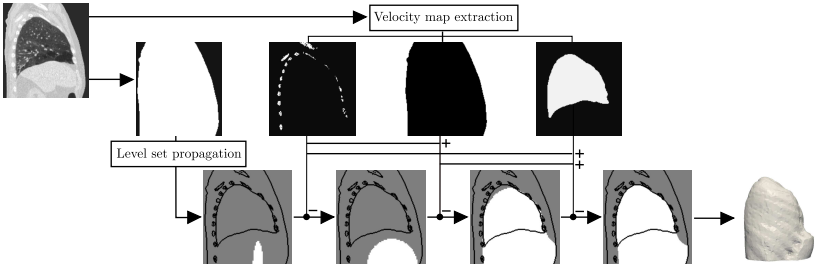

Figure 3.1: Overview of the proposed method for extracting the motion mask. Velocity maps are computed from the initial CT image by reducing them to binary images containing only the relevant features. The obtained maps are combined (+) and used to constrain (−) the evolving interface, in consecutive level set propagation steps.

of the abdomen (including the abdomen inferior to the sternum). The correlation of the motion of this region with the diaphragm and lower lungs justifies this choice. Another, more practical, argument lies in the fact that it renders the construction more reproducible.

The core of the method is based on the level set framework (Osher and Sethian, 1988). We exploit the intrinsic interface smoothing which allows to include geometric priors to guide the front propagation in regions with lack of information. The evolution of the interface is fully described by a partial differential equation in which two terms appear. The first corresponds to a propagation force, in our case based on a *velocity map* representing information on the boundaries of the object to segment. The other term corresponds to a local interface smoothing force. We can thus divide the method for obtaining the motion mask into two parts (figure 3.1). First, velocity maps are computed by reducing the original CT image to binary *label* images containing only the relevant features. The features extracted are the bony anatomy, the patient body, and the lungs. Next, the velocity maps are combined to guide the evolving interface in consecutive level set propagation steps. The algorithm is initialized with the signed distance function of a small ellipsoid, centered with respect to the patient body. By growing this initial interface, the abdomen is filled. The result is propagated further to fill the entire thoracic cavity. The found interface is then contracted to conform to the outer shape of the lungs in the upper thorax, and continue smoothly in the abdomen.

3.2.1.1 Velocity map computation

The velocity maps are obtained from the input image by extracting features through consecutive thresholding, region growing and mathematical morphology. The retained features are the outer patient body contour, the bony anatomy and the lungs. In the following we will detail the procedure followed for computing the velocity maps.

The patient body The image is binarized by thresholding at -300 Hounsfield units (HU), and the regions with lower intensity values are labelled using three dimensional (3D) connected component labelling, using a 26-voxel connectivity. The air surrounding the patient is the principal component and is removed. The remaining labels are binarized and connected component labelling will now yield the patient body as a principal label (figure 3.2, the dark grey mask).

The bony anatomy First, edge preserving smoothing is performed using anisotropic diffusion (Perona and Malik, 1990). The largest component, after binarizing with a lower threshold of 100 HU, corresponds to the connected bony structure (i.e. column, vertebrae, ribs and sternum). In some cases, parts of the ribs or sternum may be incomplete, due to locally reduced bone density. Lowering the initial threshold however will tend to include dense tissue in the liver or mediastinum, which is undesirable. Alternatively, the previously found label image is used as the seed image in a subsequent neighbourhood-controlled region growing step. The region growing is evolved as long as the visited voxel and its neighbourhood (composed of 26 voxels) all lie above the threshold of 20 HU. This approach facilitates the inclusion of additional lower density bony anatomy without leaking to the thoracic cavity. The final feature image is computed as the union of the initial connected component and the result of the region growing (figure 3.2, the light grey mask).

The lungs The lung segmentation method adopted was largely inspired by Hu et al. (2001) and the conventional segmentation method described by van Rikxoort et al. (2009, Section II.A.). First, all air in the intestine, stomach and surrounding the patient is removed by modifying their intensity to 0 HU. These regions are identified by thresholding at -300 HU and removing the second largest label, corresponding to the lungs, bronchi and trachea. Seed points in the trachea are then detected by identifying regions with intensity below -950 HU in the top

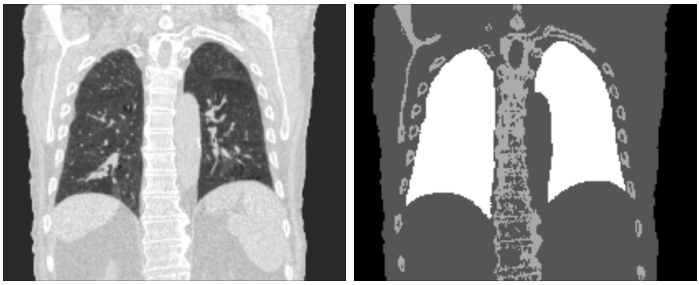

Figure 3.2: Example of an input CT image of the thorax and the corresponding extracted features: the lungs (*white*), bony anatomy (*light grey*) and patient body (*dark grey*).

5 axial slices of the scan. The trachea and large airways are extracted using explosion-controlled region growing (Mori et al., 1996). The lung region is segmented by thresholding and connected component labelling. The threshold is obtained automatically by maximizing the separability between the considered regions (Otsu, 1979). After the lung regions have been found, the trachea and bronchi are removed from the result. Finally, 3D hole filling and morphological closing using a 4 mm kernel radius is applied to include vessels and other high-density structures that were excluded by the threshold (figure 3.2, the white mask).

3.2.1.2 Level set propagation

Level sets, originally proposed by Osher and Sethian (1988), correspond to a numerical method for tracking the evolution of an interface. Let Ω be a bounded open subset of $\mathbb{R}^d$. In the level set formalism, the evolving interface $\Gamma \subset \mathbb{R}^d$ at time τ is embedded as the zero level of a Lipschitz-continuous *level set function* $\varphi : \mathbb{R}^d \mapsto \mathbb{R}$, that satisfies:

$$\begin{cases} \varphi(\boldsymbol{x}, \tau) < 0 & for \quad \boldsymbol{x} \in \Omega_{\text{in}} \\ \varphi(\boldsymbol{x}, \tau) > 0 & for \quad \boldsymbol{x} \notin \Omega_{\text{in}} \\ \varphi(\boldsymbol{x}, \tau) = 0 & for \quad \boldsymbol{x} \in \Gamma \, . \end{cases} \tag{3.1}$$

where Ω_{in} is a region in Ω bounded by $\Gamma = \partial\Omega_{\text{in}}$. In this work, the evolution of the level set is governed by the following expression (Osher

and Fedkiw, 2002):

$$\frac{\partial \varphi(\boldsymbol{x},\tau)}{\partial \tau} = \alpha\, v(\boldsymbol{x}) \|\nabla \varphi(\boldsymbol{x},\tau)\| + \beta\, v(\boldsymbol{x}) \kappa \|\nabla \varphi(\boldsymbol{x},\tau)\| \,. \tag{3.2}$$

In (3.2), κ is the curvature calculated on the zero-level, v is a scalar velocity map derived from the image, and α and β are scalar constants introduced to balance the relative influence of each of the terms. The first term provides a propagation force, favouring an expansion or contraction of the contour depending on the sign of α. The second term will penalize high curvature and serves as a spatial regularization limiting the complexity of the shape of the interface.

Note that initially, level set methods were introduced to model the front propagation of an interface (Osher and Sethian, 1988). Afterwards, they were applied to medical image segmentation to automatically detect the boundaries of structures of interest (Malladi et al., 1995; Caselles et al., 1997)–in this case obtained as the steady state solution $\frac{\partial \varphi}{\partial t} = 0$. We propose to take benefit of both uses. The level set framework is used as a high-level tool to propagate a 3D interface with a global regularization of its shape. The propagation of the interface is controlled through binary velocity maps v, defining two types of regions in Ω. One where the interface evolves with isotropic speed ($v(\boldsymbol{x}) = 1$), and one where the level set is confined to its current state ($v(\boldsymbol{x}) = 0$). For each different level set propagation step as discussed next, we will define a stopping criterion directly linked to anatomical structures.

Following the physiological considerations made in section 3.2, the sought region Ω_{in} extends beyond the field of view at the inferior end of the image, making Ω unbounded with respect to the original image size. To remedy this, all velocity maps are mirrored along the cranio-caudal axis. From the resulting mask, only the part covering the original region is retained. A strong geometric prior was established during the entire procedure by means of a high curvature scaling: $\beta = 30$.

Filling the abdomen The goal of this step is to include the abdominal region and reach the anterior patient-to-air interface. The initial contour is taken from a small ellipsoid (Figure 3.3a) centered at the first image intensity moment of the binary patient mask, i.e. the image in which the patient body has intensity 1 and the remainder 0. The level set is initialized with the signed distance map of the ellipsoid and let to evolve with $v(\boldsymbol{x}) = 1$, except at the bony anatomy where $v(\boldsymbol{x}) = 0$. A positive propagation ($\alpha = 1$) insures a growing interface. The evolution of the

contour is monitored by verifying every 50 iterations the sign of a single detection point placed 10 mm anterior to the most inferior patient-to-air interface and centered in front of the initial ellipsoid. A typical result is shown in figure 3.3b.

Filling the entire thoracic cavity Next, we wish to cover the entire thoracic cavity including the lungs and mediastinum. To this end, the previous result is propagated further ($\alpha = 1$) but the underlying velocity field is altered so that in addition to the bony anatomy, everything outside the patient body yields $v(\boldsymbol{x}) = 0$. The part of the interface which has evolved outside the patient body is now confined to its current position. The remainder of the level set is let to propagate with unit velocity inside the thoracic cavity while the coverage of the extracted lungs is monitored every 50 iterations. When the contour covers at least 95% of the lungs, the algorithm is terminated (Figure 3.3c) and the resulting mask is padded to include the full lung region. The execution is terminated at 95% rather than a 100% for reasons of efficiency, the upper part of the lungs requiring a lot of iterations while modifying very little the aspect of the contour.

Contracting to the lungs Finally, we wish to refine the previous solution to obtain a smooth contour that assumes the outer shape of the lungs, but includes the mediastinum. Only the curvature term is retained during this phase ($\beta = 30, \alpha = 0$). Note that in practice this will lead to contraction as curvature is integrated along contour length. The velocity map employed is a unit field everywhere besides outside the body, at the bony anatomy and in the lungs. The algorithm is run for 500 iterations, which was empirically found to be sufficient to smoothen the mask (figure 3.3d). In figure 3.4a the final mask is depicted in overlay with the edges of the full, *mirrored* velocity maps used during the level set propagation steps, while figure 3.4b shows two axial views (one halfway the lungs, and one corresponding to the inferior slice of the image). Figure 3.4c shows an anterior and posterior view of a 3D surface rendering of the motion mask.

3.2.2 Deformable Registration

The suitability of the obtained masks is verified by applying them to deformable registration of the lungs. The results are compared to those obtained using the same registration parameters but without making use of the motion mask. The motion field is represented by

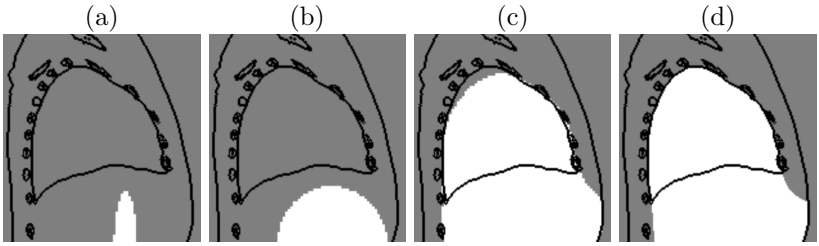

Figure 3.3: Illustration of the different level set propagation steps for obtaining the lung motion mask. Shown in a sagittal plane is the current mask (*white*) and the edges of the extracted features (*black*): (*a*) the ellipsoid used to initialize the level set, (*b*) the contour after reaching the detection point at the anterior patient-to-air interface (*c*) the contour after having covered 95% of the lung region, (*d*) the obtained motion mask.

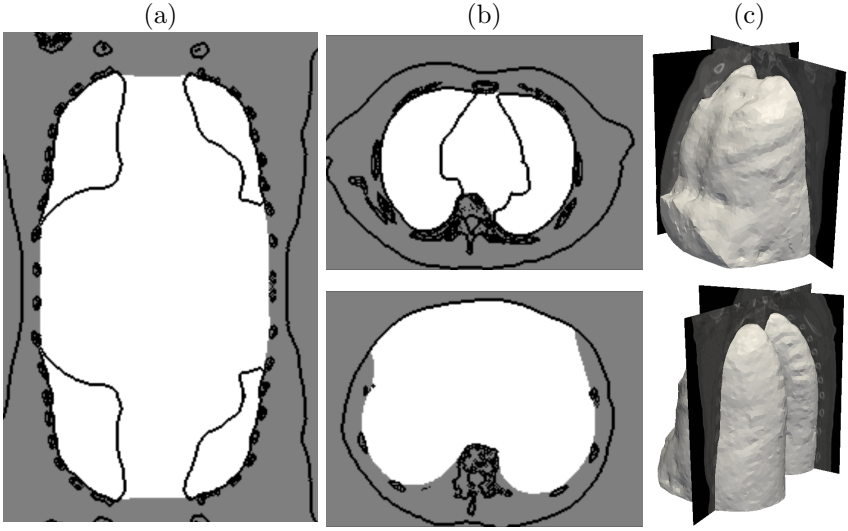

Figure 3.4: The final motion mask: (*a*) a coronal view of the final mask shown on the edges of the used *mirrored* version of the velocity maps; (*b*) two axial views of the mask: the top one taken halfway the lungs and the bottom one taken from the most inferior plane of the image; (*c*) 3D surface renderings of the anterior (*top*) and posterior (*bottom*) view of the motion mask.

a free-form deformation based on B-splines (Rueckert et al., 1999), for which we use a fast, low-memory B-LUT implementation (Sarrut and Vandemeulebroucke, 2010). A multiresolution approach with three levels is applied for the images as well as the B-spline control point grid, the final level having a 2 mm and 32 mm spacing respectively. Similarity is measured through the sum of squared differences and optimized by the limited memory BFGS algorithm (Byrd et al., 1995) starting from an initial zero deformation vector field.

3.2.2.1 Registration with motion mask

In (Rietzel and Chen, 2006), the mask corresponding to the reference image was used by excluding voxels outside the considered region from the calculation of the similarity measure. Wu et al. (2008) proposed a modified procedure to eliminate potential gaps in the motion field between the separately processed subregions. A similar procedure was adopted here for performing registrations with the help of a motion mask. First, the intensities in the reference image outside the considered region in the mask are set to -1200 HU. The target image is modified similarly, using the corresponding mask. A mask is still used to exclude voxels from the similarity measure. This time however, a slightly larger (morphologically dilated) version of the reference mask is used, so that a thin border of voxels of about 10 mm with modified intensity is included in the similarity measure. The contribution in the similarity measure of the subregion with modified intensity–and with value otherwise absent in the original image–penalizes a potential mismatch between the region borders in reference and target image, but does not constrain the sliding motion. Note however, that masks on both reference and target image are now required. As a consequence their construction should be consistent with respect to anatomical structures.

3.2.2.2 Validation based on anatomical landmarks

The registration performance for the lungs is evaluated by assessing the matching accuracy of a 100 landmarks per image pair. The landmarks were identified using a semi-automatic software tool (Murphy et al., 2008). For each end-exhalation frame, a well-distributed set of 100 landmarks in the lungs was detected fully automatically (figure 3.5). Using a custom-designed interface, trained observers identified the corresponding anatomical locations in the end-inhalation scans. The manual annotations are initially used to learn the relationship between the scans, by including

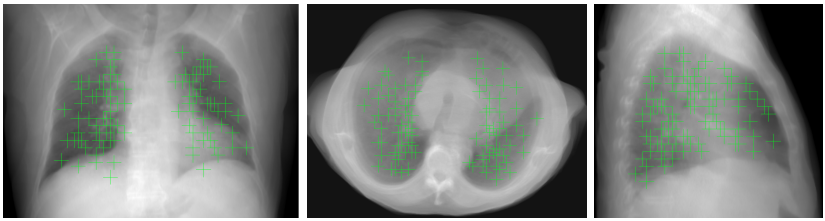

(a) (b) (c)

Figure 3.5: The 100 landmarks, automatically selected (Murphy et al., 2008) on the reference exhale frame of Patient 1, projected on the (*a*) coronal, (*b*) sagittal and the (*c*) axial planes to illustrate their location and spatial distribution.

their coordinates in a thin plate spline. The combination of the latter and local block matching is then used to suggest the positions of the remaining landmarks in the corresponding scan. Murphy et al. (2008) showed that the system is capable of automatically matching landmarks given about 20 manual annotations. In this work, all locations were manually verified, and modified if deemed necessary. The system was thus used as a software aid, greatly improving the time required for propagating the landmark set. The average of the annotations provided by two observers was used as the final landmark position and was compared with the positions estimated by the registration results.

3.3 Material

The method was applied to the exhale and inhale frames of 4D CT images of the thorax of six lung cancer patients. The patients were part of a radiotherapy planning protocol. The images were acquired on a Brilliance Big Bore 16-slice CT scanner (Philips Medical Systems, Cleveland, OH). Retrospective respiratory-correlated reconstruction into ten 3D CT images was made possible by simultaneous recording of a respiratory trace using the Pneumo Chest bellows (Lafayette Instrument, Lafayette, IN). The original resolution was approximately 1 x 1 x 2 mm. All images were resampled to a 2 mm isotropic voxel prior to processing, resulting in a typical sizes of 256 x 256 x 150 voxels.

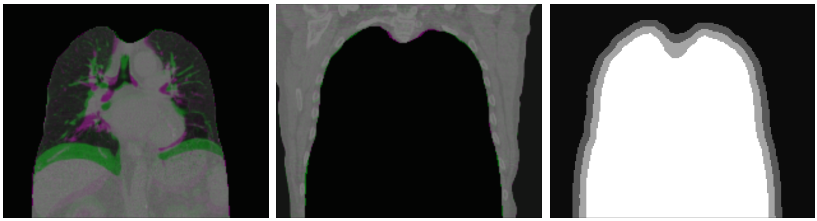

(a) (b) (c)

Figure 3.6: The images used for the registration of (a) the inner structures and (b) the outer structures. In both, the reference end-exhalation frame is shown in green-purple colour overlay with the target end-inhalation image. Purple or green indicate a difference in Hounsfield units, grey values correspond to an intensity match.(c) The mask used for calculating the similarity during the registrations. When registering the inner thoracic structures, everything but the black region is considered in the similarity measure. Inversely, for the outer structures everything but the white region is considered. The actual interface found, used for modifying the images, runs between the grey strips.

3.4 Results

The calculation of the velocity maps required less than a minute per image. The level set steps processing time, even though different for all patients, remained under 5 minutes (on a single 2.6 GHz CPU). The masks were constructed for both the end-exhalation frame and the end-inhalation frame of each 4D CT. They were then used to modify the input as described in section 3.2.2.1 , prior to registration of the inner, respectively outer thoracic regions. The modified images are show in figure 3.6, along with the mask used for the similarity measure. Very little difference between inhale and exhale can be observed for the outer thoracic structures(figure 3.6b) due to the limited motion of the ribs. Inside the thoracic cavity (figure 3.6a), large displacements can be observed. At the interface, the images overlap almost everywhere due to the predominantly diaphragmatic respiration and thanks to the consistent mask extraction. Figure 3.6c shows the mask used during the registration.

In figure 3.7 a qualitative comparison of the registration results obtained with and without use of the motion mask is given. Difference images between the reference and the warped template image are shown in a sagittal plane for Patient 1 (figure 3.7a). Inside the lung, both methods produce similar results. Strong differences can be observed near

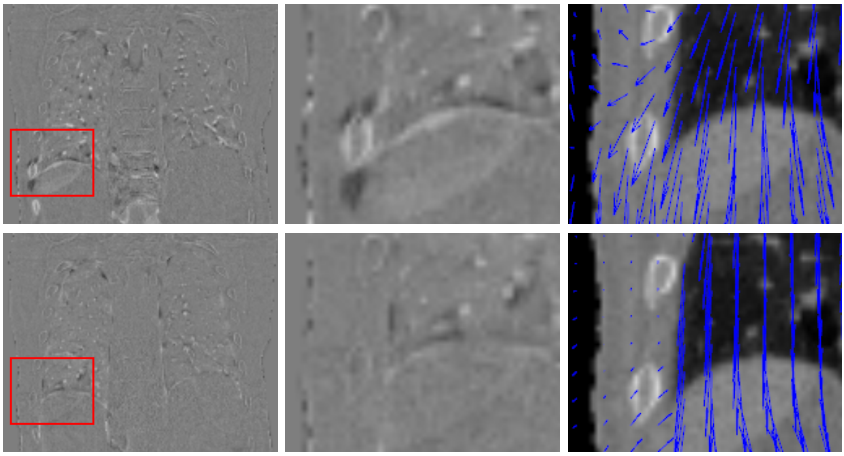

(a) (b) (c)

Figure 3.7: Comparison of the registration results for Patient 1 (*top*) without and (*bottom*) with the motion mask: (*a*) the difference of the reference and the target images compensated with obtained motion estimate, (*b*) enlarged view of the highlighted region near the right pleural interface, (*c*) deformation vector field for the same region.

the pleural interface, shown enlarged in figure 3.7b. For the same region the respective deformation vector fields are shown (figure 3.7c). Contrary to the conventional registration, a discontinuity in the deformation field can be observed when using a motion mask, resulting in an improved matching of the ribs.

The manual annotations of the two independent observers were used to verify the inter-observer variability of the anatomical landmark identification. The mean distance over all 600 points, between the annotations was 0.5 mm $\pm$ 0.9 mm. Table 3.1 contains the quantitative evaluation of the registration results. We compare the distance between the landmarks before registration, after conventional registration and after registration using the motion mask. Given are the mean distance and standard deviation, the signed average along left-right (LR), anterior-posterior (AP) and cranio-caudal (CC) directions and the maximum error. The registration results are further compared by computing a paired t-test for the landmarks distances, and considered statistically different for p-values< 0.05, as in (Sarrut et al., 2007).

Table 3.1: The distance between landmarks before registration (*before*), after conventional registration (*no mask*) and after registration using the motion mask (*mask*). Given are the mean distance (μ) and standard deviation (σ), the signed average along all directions (μ_{LR}, μ_{AP}, μ_{CC}), and the maximum distance over all points (Max). The last row lists the statistical significance of the difference between registration results, with levels $p < 5\times10^{-2}$ (+), $p < 1\times10^{-2}$ (++) and $p < 1 \times 10^{-3}$ (+++). p-values $\geq 5 \times 10^{-2}$ (=) were considered not significant.

Patient		Landmark distance (mm)					Significance
		$\mu \pm \sigma$	μ_{LR}	μ_{AP}	μ_{CC}	Max	(p-value)
1	*before*	9.36 ± 7.42	-1.71	-1.30	-8.39	32.10	
	no mask	2.39 ± 2.19	-0.22	-0.15	-1.09	11.61	++
	mask	1.83 ± 1.76	-0.29	-0.07	-0.15	12.00	(1.4×10^{-3})
2	*before*	7.33 ± 4.86	-0.82	-0.68	-6.85	24.10	
	no mask	2.84 ± 3.88	-0.54	-0.07	-1.25	22.60	+
	mask	2.57 ± 4.39	-0.43	-0.39	-0.34	19.00	(4.3×10^{-2})
3	*before*	7.09 ± 5.08	-0.90	-1.52	-5.75	19.80	
	no mask	1.84 ± 1.82	0.05	-0.28	-0.58	12.32	++
	mask	1.58 ± 1.38	0.06	-0.11	-0.11	9.68	(3.9×10^{-3})
4	*before*	6.68 ± 3.67	0.28	-0.96	-6.19	14.26	
	no mask	1.59 ± 1.50	-0.03	-0.05	-0.49	9.47	=
	mask	1.54 ± 1.24	-0.13	0.13	-0.24	8.28	(2.2×10^{-1})
5	*before*	14.00 ± 7.17	-0.68	2.50	-12.20	32.41	
	no mask	2.84 ± 2.90	-0.28	0.23	-1.45	17.30	+++
	mask	1.77 ± 1.33	-0.06	0.10	-0.12	7.32	(8.3×10^{-5})
6	*before*	6.84 ± 3.18	-1.05	0.93	-6.07	16.00	
	no mask	2.11 ± 1.53	-0.01	-0.47	-1.21	7.78	++
	mask	1.87 ± 1.24	0.06	-0.41	-0.85	6.95	(1.2×10^{-3})

3.5 Discussion

For all patients, the use of the motion mask improved the registration accuracy in terms of mean target registration error. For five out of six patients, the improvement was statistically significant. The signed average along all directions reveals that by far the largest difference between the registration results can be observed for the CC-component of the registration error. Both registration methods systematically underestimate the displacement along this component. The relatively large bias for the conventional registration, is reduced to below 1 mm when using the motion mask.

The worst registration results–both with and without using the motion mask–are obtained for Patient 2. Inspection of the largest landmark matching errors, revealed they were located near a region containing artefacts, perturbating the motion field. In fact, registration results were better using a 64 mm control point grid spacing (2.33 $\pm$ 2.42 mm and 2.81 $\pm$ 2.87 mm with and without the motion mask,respectively) then using a 32 mm (2.57 $\pm$ 4.39 mm and 2.84 $\pm$ 3.88 mm for registration with and without use of the motion mask, respectively). This observation raises another issue associated with registration of lung CT image which concerns the frequent presence of artefacts, especially in 4D CT images.

The mean landmark distance after registration when using the mask ranged from 1.54 to 2.57 mm. This is in good correspondence with previous work addressing sliding motion, reported for the lungs and performed between the inhale and exhale frames of a 4D CT acquisition (i.e. during normal tidal breathing rather than breath-hold acquisitions). Rietzel and Chen (2006) reported mean registration errors of 1.6 to 3.0 mm for five image pairs and Wu et al. (2008) obtained registration errors ranging from 2.12 to 3.48 mm for the lungs for four patients when using a B-spline based registration. Both used manual segmentations similar to the proposed motion mask. Schmidt-Richberg et al. (2009) reported between 1.04 and 2.40 mm mean landmark distance (for images with a resolution of 0.98 x 0.98 x 1.5 mm) after a diffusive registration with direction dependent regularization based on a lung segmentation. Their method significantly outperformed the conventional diffusive approach in 10 out of 12 patients. The results were similar to those obtained when limiting the regularization forces to the lungs as described by Werner et al. (2009a).

An important parameter for the used B-spline free-form deformation transformation is the spacing of the control point grid. As a finer grid is employed, the deformation space becomes larger and representation of

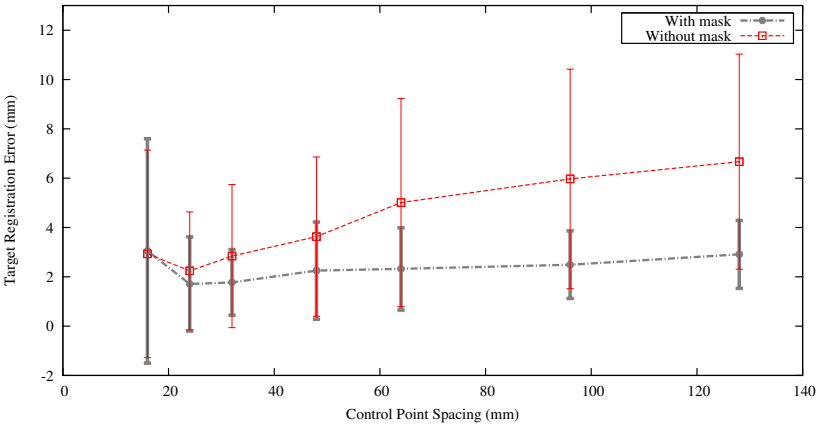

Figure 3.8: The mean target registration error with respect to the landmarks is plotted in function of the B-spline control point spacing. The error bars correspond to one standard deviation.

discontinuities such as sliding improves. However, the complexity of the optimization increases rapidly with the number of parameters, along with the computation time. Additionally, allowing more degrees of freedom increases sensitivity to noise and artefacts since the parametrization of the spatial transformation becomes less restrictive. The choice of the control point spacing is thus a trade-off between matching accuracy on one hand, and robustness and efficiency on the other. In table 3.8, the mean target registration errors (and standard deviation) obtained with and without motion mask are shown in function of the control point spacing for Patient 5, characterized by large motion amplitudes. We can note that the result obtained with mask using a control point spacing of 128 mm (2.91 ± 1.38 mm) , is comparable to that obtained without mask using a control point spacing of 32 mm (2.84 ± 2.90 mm). This indicates that, despite the large motion, the lung deformation is inherently smooth and the improved registration accuracy–obtained by increasing the number of control points– is mainly due to a better representation of the sliding motion. Considering this, the role of the motion mask can thus be viewed as *facilitating* the registration by lowering the complexity for the spatial transform, while maintaining accuracy. For a control point spacing of 16 mm, the target registration error for both registrations increases. At this spacing (and for the quality of images used), the transform seems not restrictive enough

and the registration fails. Explicit regularization in the form of an extra term in the cost function, not included here, could improve this behaviour and further reduce the matching error.

In this work registration accuracy was only evaluated in the lungs. Wu et al. (2008) reported similar improvements for the registration of the ribs. It is expected that the proposed motion mask will also result in improved matching of the ribs, as can be qualitatively assessed in figure 3.7. In the proposed method, the resulting interface below the diaphragm is the result of geometric *a priori* as there are no extracted features to constrain the evolving interface. Since the pleural interface in this region is generally not visible in the 4D CT data, the goal is rather to obtain a mask that will not perturbate registration in the upper thorax. It therefore remains to be assessed if the method can be extended for use on the liver and lower abdomen.

Particular attention was paid to making the automatic motion mask extraction robust and reliable, in order to limit the required user interaction in a clinical setting. While the described procedure produced good results for all image pairs tested, due to the large anatomical and pathological variability, it might still fail for some patients. In particular, erroneous or incomplete extraction of the lungs and ribs could result in unsatisfactory results. Often, limited manual intervention will suffice to adapt the subprocedure to the situation and produce the desired intermediate result. Alternatively, more elaborate (but costly) approaches designed to deal with the pathological lung (van Rikxoort et al., 2009), or specifically devised to label the complete ribcage (Staal et al., 2007) might reduce the user interaction even further.

The suitability of the motion mask was assessed by performing registration using B-splines on the masked images and including a boundary matching criterion. The use of the mask is however not limited to this registration method, as was demonstrated for the demons algorithm (Wu et al., 2008) and diffusive registration (Werner et al., 2009a). As discussed in section 3.1, other approaches exist to incorporating a mask in the registration algorithm. Besides preserving sliding motion, there are however some additional advantages to processing physiologically different regions separately. Most originate from the fact that registration parameters can be chosen to match each region individually. Different types of deformation in each region might lead to a different choice of control point spacing or explicit regularization. Specifically designed compressible optical flow algorithms (Castillo et al., 2009) or costly mass-preserving similarity measures (Yin et al., 2009) can be applied solely on

the inner thoracic structures. Some types of analysis, e.g. ventilation imaging (Guerrero et al., 2006), might simply only concern that region. Nonetheless, a non-negligible advantage of Schmidt-Richberg et al.'s (2009) method allowing to process the whole thorax simultaneously, lies in the fact that only the mask for the reference image is required. The construction of the mask becomes less critical as the necessity to be reproducible with respect to anatomical structures is removed.

3.6 Conclusion

We proposed a practical method for automatically dividing the upper thorax into homologously moving regions and facilitate subsequent deformable registration. The method relies on the level set framework for tracking an evolving interface and is constrained by previously extracted anatomical features and regularized by a strong geometric prior.

The suitability of the extracted motion masks was validated by applying them to deformable registration based on B-splines between exhale and inhale frames of 4D CT images. Inner and outer thoracic structures were registered separately using a boundary matching criterion and compared to conventional registration considering the whole thorax simultaneously. The target registration error was estimated from a large, well distributed set of landmarks in the lungs.

For all six patients, the mean target registration error showed improvement with respect to conventional registration. For five patients the improvement was found to be statistically significant. The use of the mask reduces the relatively large bias on the CC-component of the deformation field. The resulting target registration errors corresponded well to results reported using manual segmentations.

Qualitative evaluation showed that the proposed motion masks allow to capture discontinuities in the motion field, generating a more realistic registration near the pleural interface. In the particular case of a B-spline based free form deformation, the use of the motion mask can considerably reduce the complexity of the spatial transformation with respect to conventional registration, while maintaining registration accuracy.

Acknowledgement

This work was supported by the Région Rhône-Alpes (France) via the Simed project of the ISLE research cluster. Jef Vandemeulebroucke was

funded by the EC Marie Curie grant WARTHE. Jan Kybic was sponsored by the Czech Ministry of Education, Project MSM6840770012.

References

A. Al-Mayah, J. Moseley, M. Velec, and K. K. Brock. Sliding characteristic and material compressibility of human lung: Parametric study and verification. *Med Phys*, 36(10):4625–4633, October 2009.

V. Boldea, G. Sharp, S. B. Jiang, and D. Sarrut. 4D-CT lung motion estimation with deformable registration: Quantification of motion nonlinearity and hysteresis. *Med Phys*, 35, Issue 3:1008–1018, 2008.

Byrd, Lu, and Nocedal. A limited memory algorithm for bound-constrained optimization. *SIAM Journal of Scientifc Computing*, 16(5):1190–1208, 1995.

V. Caselles, R. Kimmel, and G. Sapiro. Geodesic active contours. *nternational Journal of Computer Vision*, 22:61–79, 1997.

R. Castillo, E. Castillo, R. Guerra, V. E. Johnson, T. McPhail, A. K. Garg, and T. Guerrero. A framework for evaluation of deformable image registration spatial accuracy using large landmark point sets. *Phys Med Biol*, 54(7):1849–1870, Apr 2009.

S. Y. Chun, J. A. Fessler, and M. L. Kessler. A simple penalty that encourages local invertibility and considers sliding effects for respiratory motion. In *Proc. SPIE 7259, Medical Imaging 2009: Image Proc., p. 72592U*, 2009.

M. Droske and M. Rumpf. Multiscale joint segmentation and registration of image morphology. *IEEE Trans Pattern Anal Mach Intell*, 29(12):2181–2194, Dec 2007.

H. Gray. *Anatomy of the Human Body.* Lea & Febiger, 20th edition, 1918.

T. Guerrero, G. Zhang, W. Segars, T. Huang, S. Bilton, G. Ibbott, L. Dong, K. Forster, and K. Ping Lin. Elastic image mapping for 4-D dose estimation in thoracic radiotherapy. *Radiat Prot Dosimetry*, 115(1-4):497–502, 2005.

T. Guerrero, K. Sanders, E. Castillo, Y. Zhang, L. Bidaut, T. Pan, and R. Komaki. Dynamic ventilation imaging from four-dimensional computed tomography. *Phys Med Biol*, 51(4):777–791, Feb 2006.

S. Hu, E. A. Hoffman, and J. M. Reinhardt. Automatic lung segmentation for accurate quantitation of volumetric X-ray CT images. *IEEE Trans Med Imaging*, 20(6):490–498, Jun 2001.

P. Keall. 4-dimensional computed tomography imaging and treatment planning. *Semin Radiat Oncol*, 14(1):81–90, Jan 2004.

M. L. Kessler. Image registration and data fusion in radiation therapy. *Br J Radiol*, 79 Spec No 1:S99–108, Sep 2006.

T. Klinder, C. Lorenz, and J. Ostermann. Respiratory motion modeling and estimation. In , *First International Workshop on Pulmonary Image Analysis*, pages 53–62, New York, 2008.

W. Lu, G. H. Olivera, Q. Chen, M.-L. Chen, and K. J. Ruchala. Automatic re-contouring in 4D radiotherapy. *Phys Med Biol*, 51(5):1077–1099, Mar 2006.

R. Malladi, J. A. Sethian, and B. C. Vemuri. Shape modeling with front propagation: A level set approach. *IEEE Transactions on Pattern Analysis and Machine Intelligence*, 17(2):158–175, 1995. ISSN 0162-8828.

J. R. McClelland, J. M. Blackall, S. Tarte, A. C. Chandler, S. Hughes, S. Ahmad, D. B. Landau, and D. J. Hawkes. A continuous 4D motion model from multiple respiratory cycles for use in lung radiotherapy. *Med Phys*, 33(9):3348–3358, Sep 2006.

J. Modersitzki. *Numerical Methods for image Registration.* Oxford University Press, 2004.

K. Mori, J. Hasegawa, J. Toriwaki, H. Anno, and K. Katada. Recognition of bronchus in three-dimensional X-ray CT images with application to virtualized bronchoscopy system. *Proceedings of the International Conference on Pattern Recognition*, 3:528532, 1996.

K. Murphy, B. van Ginneken, J. P. W. Pluim, S. Klein, and M. Staring. Semi-automatic reference standard construction for quantitative evaluation of lung CT registration. *Med Image Comput Comput Assist Interv*, 11(Pt 2):1006–1013, 2008.

S. Osher and J. Sethian. Fronts propagating with curvature dependent speed: Algorithms based on Hamilton-Jacobi formulations. *Journal of Computational Physics*, 79:12–49, 1988.

S. J. Osher and R. P. Fedkiw. *Level Set Methods and Dynamic Implicit Surfaces.* Springer, 2002.

N. Otsu. A threshold selection method from gray-level histograms. *IEEE Transactions on Systems, Man and Cybernetics*, 9(1):62–66, January 1979.

P. Perona and J. Malik. Scale-space and edge detection using anisotropic diffusion. *IEEE Transactions on Pattern Analysis and Machine Intelligence*, 12(7):629–639, 1990. ISSN 0162-8828.

E. Rietzel and G. T. Y. Chen. Deformable registration of 4D computed tomography data. *Med Phys*, 33(11):4423–4430, Nov 2006.

S. Rit, D. Sarrut, and L. Desbat. Comparison of analytic and algebraic methods for motion-compensated cone-beam CT reconstruction of the thorax. *IEEE Trans Med Imaging*, Feb 2009.

D. Ruan, J. A. Fessler, and S. Esedo. Discontinuity preserving regularization for modeling sliding effects in medical image registration. In *Proc. IEEE Nuc. Sci. Symp. Med. Im. Conf., pp. 5304-8*, 2008.

D. Ruan, S. Esedoglu, and J. A. Fessler. Discriminative sliding preserving regularization in medical image registration. In *Proc. IEEE Intl. Symp. Biomed. Imag., pp. 430-3*, 2009.

D. Rueckert, L. I. Sonoda, C. Hayes, D. L. Hill, M. O. Leach, and D. J. Hawkes. Nonrigid registration using free-form deformations: application to breast MR images. *IEEE Trans Med Imaging*, 18(8):712–721, Aug 1999.

D. Sarrut. Deformable registration for image-guided radiation therapy. *Zeitschrift fr Medizinische Physik*, 16:285–297, 2006.

D. Sarrut and J. Vandemeulebroucke. B-LUT: Fast and low memory B-spline image interpolation. *To appear in Comput Methods Programs Biomed*, June 2010.

D. Sarrut, V. Boldea, M. Ayadi, J. Badel, C. Ginestet, S. Clippe, and C. Carrie. Nonrigid registration method to assess reproducibility of breath-holding with ABC in lung cancer. *Int J Radiat Oncol Biol Phys*, 61(2):594–607, Feb 2005.

D. Sarrut, B. Delhay, P.-F. Villard, V. Boldea, M. Beuve, and P. Clarysse. A comparison framework for breathing motion estimation methods from 4-D imaging. *IEEE Trans Med Imaging*, 26(12):1636–1648, Dec 2007.

A. Schmidt-Richberg, J. Ehrhardt, R. Werner, and H. Handels. Slipping objects in image registration: improved motion field estimation with direction-dependent regularization. *Med Image Comput Comput Assist Interv*, 12(Pt 1):755–762, 2009.

J. Staal, B. van Ginneken, and M. Viergever. Automatic rib segmentation and labeling in computed tomography scans using a general framework for detection, recognition and segmentation of objects in volumetric data. *Medical Image Analysis*, 11(1):35–46, 2007.

E. M. van Rikxoort, B. de Hoop, M. A. Viergever, M. Prokop, and B. van Ginneken. Automatic lung segmentation from thoracic computed tomography scans using a hybrid approach with error detection. *Med Phys*, 36(7):2934–2947, Jul 2009.

J. von Berg, H. Barschdorf, T. Blaffert, S. Kabus, and C. Lorenz. Surface based cardiac and respiratory motion extraction for pulmonary structures from multi-phase CT. volume 6511, page 65110Y. SPIE, 2007.

M. von Siebenthal, G. Székely, U. Gamper, P. Boesiger, A. Lomax, and P. Cattin. 4D MR imaging of respiratory organ motion and its variability. *Phys Med Biol*, 52(6):1547–1564, Mar 2007.

R. Werner, J. Ehrhardt, R. Schmidt, and H. Handels. Patient-specific finite element modeling of respiratory lung motion using 4D CT image data. *Med Phys*, 36(5):1500–1511, May 2009a.

R. Werner, J. Ehrhardt, A. Schmidt-Richberg, and H. Handels. Validation and comparison of a biophysical modeling approach and non- linear registration for estimation of lung motion fields in thoracic 4D CT data. In *Proceedings of SPIE- The International Society for Optical Engineering*, volume 7259, Februari 2009b.

J. W. H. Wolthaus, J. J. Sonke, M. van Herk, and E. M. F. Damen. Reconstruction of a time-averaged midposition CT scan for radiotherapy planning of lung cancer patients using deformable registration. *Med Phys*, 35(9):3998–4011, Sep 2008.

Z. Wu, E. Rietzel, V. Boldea, D. Sarrut, and G. C. Sharp. Evaluation of deformable registration of patient lung 4DCT with subanatomical region segmentations. *Med Phys*, 35(2):775–781, Feb 2008.

A. Yezzi, L. Zllei, and T. Kapur. A variational framework for integrating segmentation and registration through active contours. *Med Image Anal*, 7 (2):171–185, Jun 2003.

Y. Yin, E. A. Hoffman, and C.-L. Lin. Mass preserving nonrigid registration of CT lung images using cubic B-spline. *Med Phys*, 36(9):4213–4222, Sep 2009.

4

Spatio-Temporal Motion Estimation for 4D Imaging of the Lungs

Jef Vandemeulebroucke[1,2,3], Simon Rit[1], Jan Kybic[3,4] and Patrick Clarysse[1] and David Sarrut[1,2]

[1]CREATIS, CNRS UMR5220, INSA-Lyon, University of Lyon, France

[2]Léon Bérard Cancer Center, University of Lyon, Lyon, France

[3]Center for Machine Perception, Czech Technical University in Prague, Czech Republic

Published in Medical Physics in January 2011

Purpose: Four-dimensional computed tomography (4D CT) provides valuable motion information for radiation therapy planning and delivery. Applying deformable registration to 4D CT is challenging due to the reduced image quality and the presence of artifacts. We aim to improve the robustness of motion estimation for respiratory-correlated imaging of the lungs, by using a global formulation of the registration problem and pursuing a restrictive parametrization for the spatio-temporal deformation model.

Methods: A spatial transformation based on free-form deformations was extended to the temporal domain. We used a cyclic trajectory model based on B-splines, allowing to consider the entire image sequence simultaneously, and enforce the temporal coherence of the deformation across the respiratory cycle. To ensure a parametrization capable of capturing the dynamics of respiratory motion, a prestudy was performed on the temporal dimension separately. The model was tuned by fitting it to diaphragm motion data acquired for a large patient group. Suitable properties were retained and applied to spatio-temporal registration of 4D CT data. Registration results were validated using large sets of landmarks and compared to consecutive spatial registrations. To illustrate the benefit of the spatio-temporal approach, we assessed the performance in the presence of motion-induced artifacts.

Results: Cubic B-splines gave better or similar fitting results as lower orders, and were selected because of their inherently stronger regularization. The fitting and registration errors increased gradually with the temporal control point spacing, representing a trade-off between achievable accuracy and sensitivity to noise and artifacts. A piecewise smooth trajectory model was found most suitable to account for the sudden changes of motion at end-inhale. Spatio-temporal modelling allowed a reduction of the number of parameters of up to 45%, while maintaining registration accuracy within 0.1 mm. The approach visibly reduced the sensitivity to artifacts.
Conclusions: Spatio-temporal registration can provide accurate motion estimation for 4D CT and improve the robustness to artifacts.

Contents

4.1 Introduction

The advent of four-dimensional (4D) computed tomography (CT) has allowed patient-specific respiratory motion information to be incorporated into radiation therapy planning and delivery. 4D CT provides multiple three-dimensional (3D) CT volumes, representing the patient at different stages of the breathing cycle (Vedam et al., 2003; Ford et al., 2003; Low et al., 2003; Pan et al., 2004). The additional patient data, implies an order of magnitude increase in the workload required to obtain a 4D treatment plan. Deformable registration is the tool that can facilitate partial automation of the planning process (Keall, 2004). It can provide the motion fields which are required for automating tasks such as re-contouring of anatomic structures (Lu et al., 2006), patient-specific margin definition (Zhang et al., 2005) or 4D treatment plan evaluation (Guerrero et al., 2005). Deformable image registration is also an enabling tool for applications that have emerged from respiratory-correlated imaging such as ventilation imaging (Guerrero et al., 2006), motion compensation (Wolthaus et al., 2008; Rit et al., 2009a) or motion modelling (McClelland et al., 2006; Zhang et al., 2007; Yang et al., 2008). Although extensive validation is required before extending the clinical use of deformable image registration, it is expected to become a standard methodology in radiotherapy (Sarrut, 2006; Kessler, 2006).

Deformable image registration can be described as the task of finding a suitable geometric transformation between corresponding image data, such that a transformed image becomes similar to another one (Modersitzki, 2004). In practice, the exact meaning of *similar* and *suitable* depends on the specifics of the application. Similarity should be measured appropriately to take into account the nature of the images, and the suitability condition suggests there exist implicit requirements with respect to the type and properties of the transformation. While the concept of image registration is easily described, the underlying numerical problem is difficult to solve. Mainly because the registration problem is *ill-posed*. Small changes of the input images may lead to very different registration results. Moreover, the solution might not be unique. Salient image information might be sparse or ambiguous, and the acquisition process might have introduced noise and artifacts. To facilitate the process, prior knowledge about the deformation should be incorporated in the registration framework in order to favour solutions with plausible physical characteristics. Explicit parametric restrictions can constrain the optimization to transformations that represent suitable

properties. This approach can offer a reduction of the search space by making the description more problem-specific, and consequently improve the robustness of the optimization process.

An example are spatio-temporal registration schemes, which consist in a global formulation of the motion estimation problem for temporal image sequences. Rather than estimating frame-to-frame displacements individually, the entire sequence is considered simultaneously, allowing to enforce the temporal coherence of the deformation across the sequence. By making assumptions about the temporal variations of the transformation, these approaches often enable a more compact and restrictive description of the full motion estimation problem. Spatio-temporal deformable registration has received considerable attention in literature, mostly in cardiac image analysis (Nastar and Ayache, 1996; Declerck et al., 1998; Huang et al., 1999; Clarysse et al., 2000; Ozturk and McVeigh, 2000; McEachen et al., 2000; Chandrashekara et al., 2004; Perperidis et al., 2005; Ledesma-Carbayo et al., 2005; Montagnat and Delingette, 2005; Delhay et al., 2006; Sundar et al., 2009; Peyrat et al., 2010; Schaerer et al., 2010), but more recently also for respiratory-correlated imaging of the thorax (Visvikis et al., 2006; Schreibmann et al., 2008; Castillo et al., 2010). Usually, a 3D-4D formulation is utilized to find a smooth time-dependent deformation field that aligns all images from a given input sequence with a reference image, which can be a frame of that same sequence (Ledesma-Carbayo et al., 2005; Delhay et al., 2006; Sundar et al., 2009; Castillo et al., 2010). Sometimes, spatial as well as temporal alignment of multiple image sequences is desirable, leading to a 4D-4D registration framework (Chandrashekara et al., 2004; Perperidis et al., 2005; Schreibmann et al., 2008; Peyrat et al., 2010).

In comparison to conventional diagnostic CT, 4D CT images tend to be acquired at lower spatial resolution and are characterized by higher noise levels because of the low radiation dose per image. In addition, an alarmingly high number of acquisitions contains motion-induced artifacts (Yamamoto et al., 2008), mainly due to irregular patient breathing during image acquisition. While the underlying image information might be considered locally invalid in the case of artifacts, clinical use of the estimated motion fields requires them to be as close to the unknown reality as possible. A restrictive parametrization of the deformation model could contribute in reducing sensitivity to local image irregularities and render the motion estimate more representative of the patient's breathing motion under these challenging circumstances.

In this study, we develop a spatio-temporal registration scheme for

lung motion quantification in respiratory-correlated sequences. Our primary objective is to obtain a low-dimensional representation of the 4D deformation model, capable of accurately representing the respiratory motion, while being more robust to artifacts and increased noise levels. The approach consists of a 3D-4D problem formulation in which temporal regularization is pursued by explicitly modelling the trajectory of moving structures. With respect to previous work on spatio-temporal registration, we specifically focus on respiratory-correlated image sequences, and develop and evaluate a cyclic trajectory model for representing the motion over an entire breathing cycle. In addition, the chosen parametrization reflects our aim of improving registration robustness by rendering the deformation model more problem-specific.

4.2 Method

The spatio-temporal transformation will be developed incrementally. We first describe a conventional spatial registration, of which the proposed method can be seen as an extension. Next, the temporal dimension is treated and the method for modelling the trajectory is detailed. The sought spatio-temporal deformation function is obtained by combining both.

4.2.1 Problem Description

Consider a 4D sequence, represented by an intensity function $f(\boldsymbol{i}, k) \in \mathbb{R}$ with $\boldsymbol{i} \in \mathbf{I} \subset \mathbb{Z}^3$ and $k \in \mathbf{K} \subset \mathbb{Z}$; $\mathbf{I}$ and $\mathbf{K}$ being the set of spatial and temporal sample indices, respectively. We wish to analyze the motion with respect to the 3D reference frame at time index $k_\mathrm{r} \in \mathbf{K}$. The task of motion estimation throughout the 4D sequence is formulated as the search for the unknown spatio-temporal transformation $\mathcal{T}_\mathrm{st}$, defined for $\mathbf{I} \times \mathbf{K} \mapsto \mathbb{R}^3$, where $\mathcal{T}_\mathrm{st}(\boldsymbol{i}, k)$ represents the location of a point at time k which was at position $\boldsymbol{i}$ at time k_r.

4.2.2 Spatial Registration

Consider the subproblem of retrieving the transformation $\mathcal{T}_\mathrm{s}$ (in which the s stands for spatial) between the reference volume and the frame at time k. A continuous representation is employed for the spatial transformation

using free-form deformations based on B-splines (Rueckert et al., 1999)

$$\mathcal{T}_{\mathrm{s}}(\boldsymbol{x}) = \boldsymbol{x} + \sum_{\boldsymbol{j}\in\mathbf{J}} \boldsymbol{a}_{\boldsymbol{j}} \phi_{\boldsymbol{j}}(\boldsymbol{x}) \tag{4.1}$$

where $\boldsymbol{x} \in \mathbf{X}$ is the continuous spatial coordinate associated with $\mathbf{I}$; $\mathbf{J} \subset \mathbb{Z}^3$ is the set of spatial parameter indices considered for basis functions $\phi_{\boldsymbol{j}}(\boldsymbol{x}) = \beta^n(\boldsymbol{x}/h - \boldsymbol{j})$ with $h \in \mathbb{R}$ the uniform spatial control point spacing, and β^n the tensor product of one-dimensional B-spline kernels of degree n. We use cubic B-splines for the spatial basis functions ($n = 3$). The parameters of $\mathcal{T}_{\mathrm{s}}$ are the B-spline coefficients $\boldsymbol{a}_{\boldsymbol{j}} \in \mathbb{R}^3$ (one for each component of the deformation), i.e. $\mathcal{T}_{\mathrm{s}}$ is fully characterized by specifying $\boldsymbol{a} = \{\boldsymbol{a}_{\boldsymbol{j}}\}_{\boldsymbol{j}\in\mathbf{J}}$.

We define a similarity criterion $\mathcal{J}_{\mathrm{s}}$, based on the mean squared intensity differences with respect to the samples of the reference volume

$$\mathcal{J}_{\mathrm{s}}(\mathcal{T}_{\mathrm{s}}; k) = \frac{1}{N_{\mathbf{I}}} \sum_{\boldsymbol{i}\in\mathbf{I}} \Big(f\big(\mathcal{T}_{\mathrm{s}}(\boldsymbol{i}), k\big) - f\big(\boldsymbol{i}, k_{\mathrm{r}}\big) \Big)^2 \tag{4.2}$$

with $N_{\mathbf{I}}$ the number of spatial samples considered. We choose this criterion because of its fast computation time and the smoothness of the resulting search space. For simplicity, no explicit regularization term was included in the criterion. For now, only the influence of the parametrization of the deformation function is explored. Evaluating f at non-grid positions, requires a continuous representation of the intensity function for which we used cubic B-spline interpolation

$$f(\boldsymbol{x}, k) = \sum_{\boldsymbol{i}\in\mathbf{I}} \boldsymbol{d}_{\boldsymbol{i}} \beta^n(\boldsymbol{x} - \boldsymbol{i}) \,. \tag{4.3}$$

Coefficients $\boldsymbol{d}_{\boldsymbol{i}}$ are found quickly using recursive filtering (Unser, 1999).

Solving the spatial registration problem for frame k comes down to estimating the optimal parameters $\boldsymbol{a}^*$ in the sense of the criterion $\mathcal{J}_{\mathrm{s}}$

$$\boldsymbol{a}^* = \arg\min_{\boldsymbol{a}} \mathcal{J}_{\mathrm{s}}(\mathcal{T}_{\mathrm{s}}; k) \,. \tag{4.4}$$

By solving (4.4) consecutively for all $k \in \mathbf{K}$ except k_{r}, a solution to the 4D motion estimation problem can be composed. Solutions obtained for previous k values, can be used to initialize subsequent registrations.

4.2.3 Trajectory Modelling

Temporal sequences enable alternative analysis of the motion, by modelling the temporal variations of the estimated deformations. Tissue

trajectories are expected to evolve smoothly and continuously over time which allows to introduce constraints which enforce the temporal coherence of the deformation across the sequence. This is similar to the approach described for the spatial dimensions. Nonetheless, the temporal dimension is handled separately as it is inherently different from the other dimensions. For instance, in the case of respiratory-correlated CT, the sequence is periodic and the number of temporal samples is low compared to spatial samples.

Trajectory Model Let $t \in \mathbf{T}$ be the continuous coordinate associated with $\mathbf{K}$ and suppose for simplicity $\mathbf{T} = [0, t_\mathrm{e})$. Let $\mathcal{T}_\mathrm{t}(\boldsymbol{x}, t)$ denote the trajectory of a point at position $\boldsymbol{x}$ at time t_r. The search for $\mathcal{T}_\mathrm{t}$ is limited to continuous and smooth functions of t, by expressing it using a suitable set of basis functions $\{\psi_l\}_{l \in \mathbf{L}}$

$$\mathcal{T}_\mathrm{t}(\boldsymbol{x}, t) = \boldsymbol{x} + \sum_{l \in \mathbf{L}} \boldsymbol{b}_l \psi_l(t) \,. \tag{4.5}$$

$\mathbf{L} \subset \mathbb{Z}$ is the set of temporal parameter indices and $\boldsymbol{b_l} \in \mathbb{R}^3$ the coefficients of the basis functions. As in (Declerck et al., 1998; Huang et al., 1999; Ozturk and McVeigh, 2000; Chandrashekara et al., 2004; Ledesma-Carbayo et al., 2005), we adopted temporal B-spline basis functions, $\psi_l(t) = \beta^m(t/s - l)$ with $s \in \mathbb{R}$ the temporal control point spacing, because of their good approximation properties, computational simplicity and implicit smoothness. In (Ledesma-Carbayo et al., 2005) temporal B-splines were found to work at least as well as harmonic functions, used in (Nastar and Ayache, 1996; Clarysse et al., 2000; McEachen et al., 2000; Delhay et al., 2006). Figure 4.1a shows a schematic, one-dimensional representation of a trajectory model based on cubic B-splines ($m = 3$), with five control points ($s = t_\mathrm{e}/5$) placed uniformly along the considered interval $[0, t_\mathrm{e})$. Evaluating $\mathcal{T}_\mathrm{t}$ near the borders of the interval, requires taking into account control points with non-zero weight just outside the interval. It can be seen that a total of eight degrees of freedom is considered.

Smooth Trajectory Model The trajectory model can be further constrained by incorporating *a priori* knowledge of the motion, leading to a more restrictive parametrization. For instance, 4D CT data is inherently periodic. In addition, trajectories can be expected to be smooth functions of time. The trajectory can be made periodic and smooth throughout the

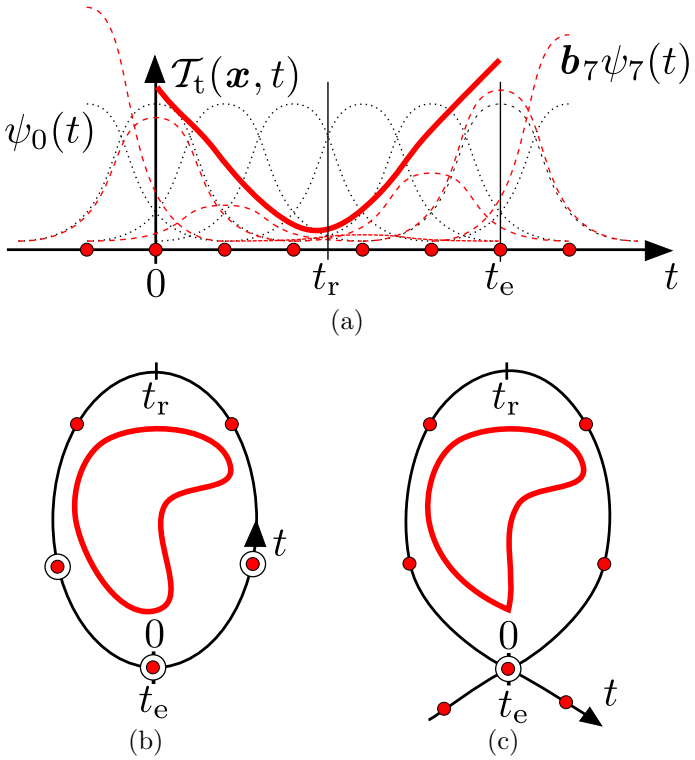

Figure 4.1: (a) Schematic representation of a trajectory model based on cubic B-splines, with eight control points (*red dots*) placed uniformly inside and just outside $[0, t_\mathrm{e})$. Each corresponds to a B-spline kernel ψ_l (*dotted line*) and $\mathcal{T}_\mathrm{t}(\boldsymbol{x},t)$ (*red solid curve*) is found by combining the scaled kernels (*dashed line*). (b, c) Alternative, 2D representation with a cyclic temporal axis wrapped around the trajectory. Large control points indicate a constraint is applied. (*b*) The smooth trajectory model $\mathcal{T}_\mathrm{t}$ and, (*c*) the piecewise smooth trajectory model $\mathcal{T}_\mathrm{t}^*$.

entire cycle by imposing the same order of smoothness to the endpoints as the rest of the trajectory, thus obtaining $\mathcal{T}_\mathrm{t} \in C^{m-1}(\mathbf{T})$. This leads to the set of m conditions

$$\frac{\partial^z \mathcal{T}_\mathrm{t}(\boldsymbol{x}, 0)}{\partial t^z} = \frac{\partial^z \mathcal{T}_\mathrm{t}(\boldsymbol{x}, t_\mathrm{e})}{\partial t^z} \quad \text{for} \quad z = [0, \ldots, m-1\,]. \tag{4.6}$$

As will be shown, each condition results in a linear equation for the model parameters, allowing to express one of the parameters in function of the others. A schematic representation of a 2D trajectory satisfying (4.6) is shown in figure 4.1b. A cyclic time axis is shown to illustrate the placement and the influence of the control points. The banded control points indicate that a constraint is applied.

Piecewise Smooth Trajectory Model Due to the limited temporal resolution of 4D CT, and depending on the degrees of freedom considered in (4.5), the smoothness constraint might be too restrictive, leading to locally reduced representation accuracy in regions where the velocity is varying rapidly. This can be the case for the end-inhale phase where fast inversion of the motion takes place. Alternatively, we can locally relax the smoothness constraints and propose a piecewise smooth trajectory representation $\mathcal{T}_\mathrm{t}^*$. A similar expansion as (4.5) is utilized for $\mathcal{T}_\mathrm{t}^*$ but, assuming end-inhale corresponds to $t = 0$, a single constraint is applied

$$\mathcal{T}_\mathrm{t}^*(\boldsymbol{x}, 0) = \mathcal{T}_\mathrm{t}^*(\boldsymbol{x}, t_\mathrm{e})\,. \tag{4.7}$$

This condition will lead to periodic trajectories, but allows a discontinuity in the velocity (figure 4.1c). In this case, the sections near end-inhale are parametrized independently which implies a local increase of control points and degrees of freedom.

Temporal Constraints Introducing the temporal constraints in the trajectory model is illustrated for a constraint useful during image registration. As deformation is estimated with respect to a reference, by definition

$$\mathcal{T}_\mathrm{t}(\boldsymbol{x}, t_\mathrm{r}) = \boldsymbol{x}\,. \tag{4.8}$$

Following (Ledesma-Carbayo et al., 2005), introducing this condition into (4.5) removes one degree of freedom and the temporal model can be expressed using a smaller set of constrained basis functions

$$\psi_l^\mathrm{c}(t) = \psi_l(t) - \frac{\psi_l(t_\mathrm{r})\psi_{l_\mathrm{r}}(t)}{\psi_{l_\mathrm{r}}(t_\mathrm{r})}\,, \tag{4.9}$$

where it was assumed that we constrained the parameter b_{l_r}. The obtained set of basis functions only generates trajectories that satisfy (4.8).

In the following, we will denote $\{\psi_l^c\}_{l\in\mathbf{L}^c}$ the set of basis functions to which constraints (4.6) and (4.8) have been applied.

4.2.4 Spatio-Temporal Registration

Estimating the motion in a 4D CT sequence by performing consecutive spatial registrations using (4.1) fails to exploit the temporal relation between the frames. This is remedied by modelling the trajectory as in (4.5). A combined approach is found by coupling the temporal and the spatial deformation model

$$\mathcal{T}_{\text{st}}(\boldsymbol{x},t) = \boldsymbol{x} + \sum_{\boldsymbol{j}\in\mathbf{J}}\sum_{l\in\mathbf{L}^c} \boldsymbol{c}_{\boldsymbol{j},l}\,\phi_{\boldsymbol{j}}(\boldsymbol{x})\psi_l^c(t)\,. \tag{4.10}$$

The result is a linear, spatio-temporal deformation function, separable in space and time. A straightforward extension to the temporal dimension of (4.2), leads to the criterion

$$\mathcal{J}_{\text{st}}(\mathcal{T}_{\text{st}}) = \frac{1}{N_{\mathbf{K}}}\sum_{k\in\mathbf{K}} \mathcal{J}_{\text{s}}(\mathcal{T}_{\text{st}};k) \tag{4.11}$$

to be optimized with respect to the parameters $\boldsymbol{c} = \{\boldsymbol{c}_{\boldsymbol{j},l}\}_{\boldsymbol{j}\in\mathbf{J},l\in\mathbf{L}^c}$. We will use $\mathcal{T}_{\text{st}}$ and $\mathcal{T}_{\text{st}}^*$ in reference to the spatio-temporal deformation models obtained when using the smooth and piecewise smooth temporal models $\mathcal{T}_{\text{t}}$ and $\mathcal{T}_{\text{t}}^*$, respectively.

4.2.5 Motion Mask Extraction

Breathing motion is characterized by sliding of the liver and lungs, resulting in a discontinuity of the motion at the pleural wall (Wu et al., 2008; Schmidt-Richberg et al., 2009). Accurate matching in these regions requires a complex spatial transformation, even though the remainder of the deformation can be considered smooth. We previously addressed this issue (Vandemeulebroucke et al., 2010) by automatically extracting a motion mask, dividing the thorax into moving (lungs, mediastinum and abdomen) and less-moving regions (the remainder).

Motion masks were computed for all frames of f. The result is the division of the thorax into two subregions $\mathbf{I}_{\text{in}}, \mathbf{I}_{\text{out}} \subset \mathbf{I}$, roughly representing the inner and outer thoracic structures. For each of

the subregions, a separate registration problem can be formulated following (Wu et al., 2008), with the advantage that the search can be limited to spatially smooth deformations.

4.2.6 Optimization

The spatio-temporal approach allows a more restrictive parametrization of the transform and reduces the total number of degrees of freedom of the 4D motion estimation problem compared to consecutively applying $\mathcal{T}_\mathrm{s}$. However, directly minimizing (4.11) considers all degrees of freedom simultaneously, increasing the dimensionality of the optimization problem with respect to one 3D-3D registration. In response, a multiresolution approach was employed, allowing to gradually increase the complexity of the problem. The resolution of the spatial dimensions of both the image sequence and the transform control point grid was doubled in each of three consecutive resolution levels. The final image resolution was set to 2 mm. We previously found that, in combination with a motion mask, a control point grid spacing $h = 32$ mm provided a good compromise between efficiency and matching accuracy. The temporal dimension, characterized by low resolution, remained unmodified throughout the optimization.

Each level was handled using a Quasi-Newton approach in the form of the limited memory BFGS method (Nocedal, 1980), because of its high precision and improved rate of convergence with respect to simple gradient descent algorithms (Klein et al., 2007). The procedure started from a zero deformation, and subsequent levels were initialized by upsampling the previous solution. The required partial derivatives can be calculated explicitly, for instance for $\mathcal{T}_\mathrm{st}$

$$\frac{\partial \mathcal{J}_\mathrm{st}(\mathcal{T}_\mathrm{st})}{\partial \boldsymbol{c}_{\boldsymbol{j},l}} = \frac{2}{N_\mathbf{K} N_\mathbf{I}} \sum_{k\in\mathbf{K}} \sum_{\boldsymbol{i}\in\mathbf{I}} \Big(f\big(\mathcal{T}_\mathrm{st}(\boldsymbol{i},k),k\big) - f\big(\boldsymbol{i},k_\mathrm{r}\big) \Big) \frac{\partial f\big(\mathcal{T}_\mathrm{st}(\boldsymbol{i},k),k\big)}{\partial \boldsymbol{x}} \frac{\partial \mathcal{T}_\mathrm{st}(\boldsymbol{i},k)}{\partial \boldsymbol{c}_{\boldsymbol{j},l}} . \tag{4.12}$$

$\partial f/\partial \boldsymbol{x}$ is found by deriving (4.3), while $\partial \mathcal{T}_\mathrm{st}/\partial \boldsymbol{c}_{\boldsymbol{j},l}$ can be calculated considering (4.10). For instance, for the q^th spatial component

$$\frac{\partial f(\boldsymbol{x},k)}{\partial x_q} = \sum_{\boldsymbol{i}\in\mathbf{I}} \boldsymbol{d}_\mathbf{i} \frac{\partial \beta^n(x_q)}{\partial x_q} \prod_{\zeta\neq q} \beta^n(x_\zeta - i_\zeta) \tag{4.13}$$

$$\frac{\partial \mathcal{T}_\mathrm{st}(\boldsymbol{i},k)}{\partial \boldsymbol{c}_{\boldsymbol{j},l,q}} = \phi_{\boldsymbol{j}}(\boldsymbol{x}) \psi_l^c(t) \, . \tag{4.14}$$

4.2.7 Implementation

The registration algorithms were implemented in C++. Evaluating $\mathcal{T}_{\text{st}}(\boldsymbol{i}, k)$ was performed using B-LUTs (Sarrut and Vandemeulebroucke, 2010): a fast, low memory B-spline implementation based on a look-up table of B-spline tensor products $\beta^n(\boldsymbol{x})$. Registration algorithms were multi-threaded and executed on an eight-core system. The execution times depended on the specifics of the 4D CT set. For ten time frames, consecutively registering all frames of f using $\mathcal{T}_{\text{s}}$, required between 5 and 10 hours, whereas T_{st} and $\mathcal{T}_{\text{st}}^*$ required about twice as much time.

In comparison, the most expensive step for the spatio-temporal approaches is the calculation of $\partial\mathcal{T}_{\text{st}}(\boldsymbol{i}, k)/\partial\boldsymbol{c}$ in (4.12). In the current implementation, this requires multiple table look-ups due to the presence of the modified basis functions ψ^{c} in (4.14), compared to only one for calculating $\partial\mathcal{T}_{\text{s}}/\partial\boldsymbol{a}$.

4.3 Experiments

Three types of experiments were performed to validate the spatio-temporal deformation model. First, we conducted a prestudy on the temporal dimension of the model separately. Breathing patterns are patient-specific and strong interpatient and intercycle variability has been reported which can affect cycle duration, motion amplitude and speed of the movement (George et al., 2005; Wu et al., 2007; Rit et al., 2009b). By fitting the trajectory models to motion data covering many cycles and measured on a large set of patients, we ensure the temporal parametrization is flexible enough to capture the dynamics of respiratory motion.

The most suitable temporal parameter values were retained and used for the spatio-temporal deformation models. The latter were applied to the registration of 4D CT images of the thorax. Extensive spatial validation of the registrations was performed using large sets of landmarks. The registration accuracy was compared to the conventional frame-to-frame approach. In a final experiment, the benefit of the spatio-temporal approach is illustrated, by assessing the performance in the presence of artifacts.

4.3.1 Temporal Fit of Diaphragm Motion Data

Data Description We used projection sequences of cone-beam computed tomography (CBCT) acquired at the Netherlands Cancer Institute (Amsterdam, the Netherlands) for image-guidance of 33 lung cancer patients treated by radiotherapy with the protocol described in (Sonke et al., 2008). Cone-beam projections consist of rectangular X-ray images, acquired from rotating views around the patient. They were acquired at 5.5 fps over 200° with a 50°/min gantry rotation speed for 4D CBCT imaging (Sonke et al., 2005). Their resolution was 512^2 pixels of 0.8^2 mm^2 (0.52^2 mm^2 at the isocenter). 257 sequences of cone-beam projection images (5 to 19 per patient) were analyzed.

The motion was analyzed by extracting the cranio-caudal position of a diaphragm dome using an adapted version (Rit et al., 2009b) of the algorithm developed to extract a respiratory signal for 4D CBCT reconstruction (Zijp et al., 2004; Sonke et al., 2005). The extraction results in a 2 min 1D+t signal per acquisition with 0.52 mm and 5.5 fps resolution, i.e. 2 of the 4 dimensions of the sought 4D model at fine resolution but for only one point of space. In addition to the size of the dataset, the projection images are advantageous because they have higher cranio-caudal and temporal resolutions than 4D CT images. As such, the diaphragm motion data provided a valuable benchmark for tuning the temporal parametrization of the deformation models.

Experiments Each signal was split in respiratory cycles by detecting the end-inhale peaks after smoothing out the local minima. Each cycle was analyzed separately by assuming periodicity, similar to 4D CT images. The temporal models described in section 4.2.3, were fitted to each cycle with the optimal solution in the least square sense. The influence of the trajectory model parameters was evaluated: we varied the B-spline order m and the control point spacing s, or equivalently the number of control points. In addition, we verified the suitability of a smoothness constraint at end-inhale by comparing $\mathcal{T}_\mathrm{t}$ and $\mathcal{T}_\mathrm{t}^*$.

The similarity between the measured and the fitted signals was evaluated using the root mean square (RMS) of their difference. Results for each patient were averaged and the group mean over all patients was computed. The results were analyzed both globally and per respiratory phase by dividing each cycle into ten equi-temporal phase bins, as it is typically done in current 4D CT scanners.

4.3.2 Spatio-Temporal Registration of 4D CT

Data Description We used 4D CT data sets of six non-small cell lung cancer patients acquired at the Léon Bérard Cancer Center (Lyon, France) for the purpose of radiotherapy planning on a Philips 16-slice Brilliance Big Bore Oncology Configuration (Phillips Medical Systems, Cleveland, OH). Acquisitions were performed in helical mode using a table pitch of 0.1, 400 mAs effective exposure (80 mA tube current) at 120 kV.

Respiratory-correlated reconstruction was facilitated by simultaneous acquisition of a respiratory surrogate signal, provided by the Pneumo Chest pressure belt (Lafayette Instrument, Lafayette, IN). We used the tags on the end-inhale positions automatically provided by the system, and each detected cycle was divided into equi-temporal phase bins. Reconstruction yielded ten 3D CT frames at approximately $1 \times 1 \times 2$ mm^3 resolution.

Experiments The spatio-temporal deformable registration approaches $\mathcal{T}_{\mathrm{st}}$ and $\mathcal{T}_{\mathrm{st}}^*$, as described in section 4.2.4, were applied to all 4D CT data sets. In addition to the normal set of constraints used for $\mathcal{T}_{\mathrm{t}}$ and $\mathcal{T}_{\mathrm{t}}^*$, constraint (4.8) is enforced for all registrations. Deformable registration was performed with respect to the middle frame ($k = 5$), which corresponded roughly to end-exhale. The position of end-exhale has been reported to be more reproducible than end-inhale (Seppenwoolde et al., 2002; Sonke et al., 2008), making it a suitable reference to analyze breathing motion.

For validation purposes, anatomical landmarks were identified in the lung region using a semi-automatic software tool (Murphy et al., 2008). The system automatically provided a set of well-distributed, distinctive points with index $\boldsymbol{p}_{\mathrm{r}} \in \mathbf{I}$ in the lung region of the exhale frame. Observers identified the corresponding positions $\boldsymbol{p}_k \in \mathbf{I}$ of the points in frame k, using a custom designed interface and aided by initial estimates provided by the system. Points coinciding with artifacts were excluded. The system initially provided 130 distinctive points and the procedure was stopped after a 100 points were successfully identified in the corresponding frames.

For all six patients, 100 point correspondences were provided between the exhale and the inhale frame, and the process was repeated by a second observer. The mean distance between the annotations was 0.5 mm (0.9 mm standard deviation). For Patients 1-3, a single observer provided 100 correspondences for each of the frames of the 4D CT, resulting in a total of 900 manually identified landmarks for each of the three data sets. The

manual annotations were compared to the corresponding point positions estimated through registration to compute the target registration error (TRE)

$$\mathrm{TRE} = \|\mathcal{T}_{\mathrm{st}}(\boldsymbol{p}_{\mathrm{r}}, k) - \boldsymbol{p}_k\| \,. \tag{4.15}$$

The registration results were also compared to those obtained when performing consecutive 3D registrations using $\mathcal{T}_{\mathrm{s}}$, described in section 4.2.2. The same multiresolution and optimization scheme is applied as in the spatio-temporal case. Since no temporal regularization is applied in the case of $\mathcal{T}_{\mathrm{s}}$, the results are considered as a reference indicating the achievable registration accuracy when allowing all temporal degrees of freedom.

4.3.3 Registration of Artifacted 4D CT

Data Description To dispose of a ground truth, we constructed an artifacted 4D CT acquisition f_{a} by introducing a simulated, motion-induced artifact in the 4D CT of patient 2, characterized by large motion. A mid-inhalation frame (k=8) was altered by modifying a series of axial slices halfway the lungs. Ten slices starting from slice index i_{a} in the end-exhale frame (k=5), were copied to the same location in the target frame, i. e.

$$f_{\mathrm{a}}(\boldsymbol{i}, k) = \begin{cases} f(\boldsymbol{i}, 5) & \text{for } k = 8, i_2 \in [i_{\mathrm{a}}, i_{\mathrm{a}} + 10) \\ f(\boldsymbol{i}, k) & \text{otherwise} \end{cases} . \tag{4.16}$$

The procedure resulted in an axial slab of 20 mm along the cranio-caudal direction, containing an inconsistent view of the patient anatomy with respect to the surrounding slices. This resembles the situation of a frame locally influenced by erroneous tagging of the respiratory phase, or irregular breathing during image acquisition.

Experiments The simulated sequence f_{a} was registered in the same way as described in the previous experiment. The registration results were compared to those obtained using consecutive 3D registrations. By comparing also to the results obtained for the original sequence, the sensitivity of the method to locally introduced artifacts was evaluated.

The registration accuracy was assessed by using the landmarks identified in the original, unmodified 4D CT acquisition. The analysis is performed at two levels. Fist, we computed a global evaluation of the TRE, taking into account all landmarks. Secondly, a local analysis was

performed by only considering landmarks located within five slices of the artifact.

4.4 Results

4.4.1 Temporal Fit of Diaphragm Motion Data

The fitting results are summarized in table 4.1 for a variety of B-spline functions. Constant B-splines ($m = 0$) gave much poorer results than other degrees. This is not surprising, since they produce piecewise constant functions which can not describe the continuity of the respiratory motion. Linear B-splines ($m = 1$) gave residuals of the same order, but were found significantly worse than quadratic ($m = 2$) and cubic splines ($m = 3$) for all tested models ($p < 3 \times 10^{-4}$). Cubic B-splines consistently gave better results than quadratic splines, although the difference was not always significant. As they also inherently impose a stronger temporal regularization, which is the purpose of the study, they were selected for the rest of the study.

The influence of the number of control points can also be seen from table 4.1. For both models, the residual of the fit was proportional to the spacing of the control points s: the Pearson's product-moment correlation coefficient was greater than 0.99. As expected, the number of control points is a trade-off between the achievable representation accuracy and the parameters of the fitted function.

We used box and whisker plots to further illustrate the distribution of fitting errors. The box extends from the lower ($p_{25\%}$) to upper quartile ($p_{75\%}$) of the data, with a red horizontal line at the median and a $*$ symbol at the mean. The whiskers extend from the box to the most extreme value below $p_{25\%} + 0.75 \times (p_{75\%} - p_{25\%})$, the remaining points are considered outliers. Outliers were not plotted for clarity.

The top plots in figure 4.2 illustrate the global fitting errors and the errors per respiratory phase bin for $\mathcal{T}_{\text{t}}$ and $\mathcal{T}_{\text{t}}^*$ (using five internal control points and $m = 3$). The overall performance of $\mathcal{T}_{\text{t}}^*$ was much better than for $\mathcal{T}_{\text{t}}$. The largest discrepancies can be observed near inhale (0%). At this phase, the change of speed was too sudden to be described by the smooth trajectory model $\mathcal{T}_{\text{t}}$ and the residual was found to be significantly higher ($p < 2 \times 10^{-3}$) than at all other phases, for all tested values of m and s. This was not the case for the piecewise smooth $\mathcal{T}_{\text{t}}^*$ model, which resulted in more homogeneous residuals per phase because the smoothness constraint is relaxed at end-inhale.

Spline Degree m	Internal Control Points						
	4	5	6	7	8	9	10
	Group mean RMS (mm) of $\mathcal{T}_t$						
0	2.65	2.25	1.95	1.72	1.53	1.39	1.27
1	1.25	0.98	0.83	0.72	0.63	0.57	0.51
2	1.17	0.89	0.77	0.67	0.60	0.54	0.49
3	1.17	0.87	0.76	0.66	0.59	0.53	0.48
	Group mean RMS (mm) of $\mathcal{T}_t^*$						
2	0.70	0.56	0.47	0.40	0.34	0.30	0.27
3	0.67	0.55	0.47	0.40	0.35	0.30	0.27

Table 4.1: Group mean of the RMS of the difference between the measured motion of the diaphragm dome in the cranio-caudal direction and fitted functions for the two temporal models with different number of control points and B-spline degrees. For degrees 0 and 1, both models are equivalent.

The difference in temporal constraints between $\mathcal{T}_t$ and $\mathcal{T}_t^*$ results in a different number of degrees of freedom at equal control point spacing. We therefore also performed a comparison between both models at equal degrees of freedom (bottom row of figure 4.2, for $\mathcal{T}_t$ and $\mathcal{T}_t^*$ using seven and five internal control points, respectively). In this case, the global performance of $\mathcal{T}_t$ was still significantly worse ($p < 4 \times 10^{-2}$) compared to the corresponding $\mathcal{T}_t^*$ model for all tested number of the control points. This can also be seen from table 4.1, comparing the results for $\mathcal{T}_t^*$ with two control points less than $\mathcal{T}_t$. Despite the *global* increase in degrees of freedom, the high fitting residual at inhale remained for $\mathcal{T}_t$ (figure 4.2b, bottom right). These results suggest that a *local* increase in control points (as is the case for the piecewise smooth model $\mathcal{T}_t^*$) is more efficient in terms of number of parameters, to obtain an accurate representation throughout the respiratory cycle.

4.4.2 Spatio-Temporal Registration of 4D CT

We retained the temporal representations with four and five internal control points for the spatio-temporal model, which corresponds to $s = 2.5$ and 2 frames, respectively. Table 4.2 summarizes the temporal characteristics of the registration methods.

Trajectories obtained for some landmarks with large displacements are plotted in figure 4.3. The manually identified positions throughout the

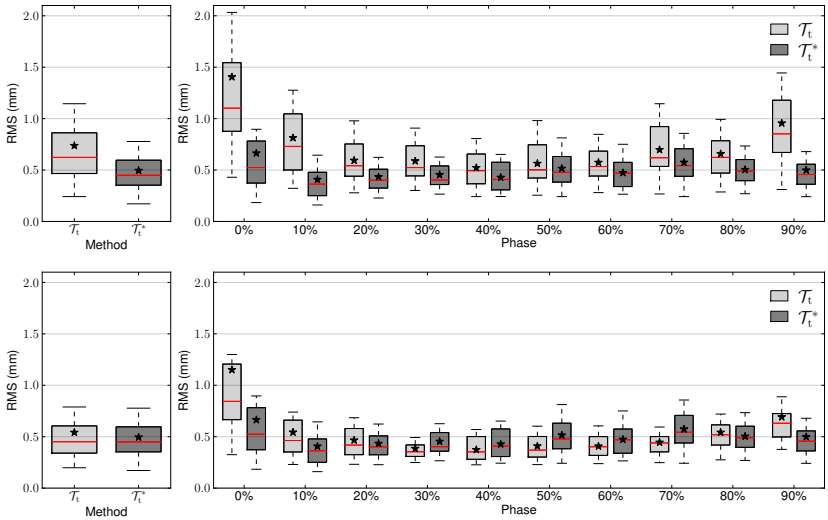

Figure 4.2: Box and whisker plots of the RMS errors per patient after fitting the models to the diaphragm motion data. (*a*) The RMS over the entire cycle; (*b*) the RMS per phase bin; (*top*) the RMS per phase bin with five internal control points for both temporal models and $m = 3$; (*bottom*) The RMS per phase bin with the same number of degrees of freedom for both models: the $\mathcal{T}_t$ model with $m = 3$ and seven internal control points, and the $\mathcal{T}_t^*$ model with $m = 3$ and five internal control points.

Properties	Representation				
	$\mathcal{T}_{\mathrm{s}}$	$\mathcal{T}_{\mathrm{st}}$		$\mathcal{T}^*_{\mathrm{st}}$	
	$s = 1$	$s = 2$	$s = 2.5$	$s = 2$	$s = 2.5$
Temporal CP	9	8	7	8	7
Continuity at $t = 0$	$\diagup$	C^2	C^2	C^0	C^0
Constraints	0	4	4	2	2
Temporal DOF	9	4	3	6	5
Parameters	63 882	28 392	21 294	42 588	35 490

Table 4.2: Summary of the temporal properties for the registration methods when using cubic splines for the spatio-temporal methods, and a control point spacing of either 2 or 2.5 frames. The amount of temporal control points (CP) includes the internal CP as well as the ones required at the border. The number of degrees of freedom (DOF) are the number of CP, reduced by the number of constraints. As an example we list the resulting number of parameters required to register the inner thoracic region ($\mathbf{I}_{\mathrm{in}}$) for Patient 1.

4D CT are also shown and were linearly interpolated for clarity. The estimates obtained using $\mathcal{T}_{\mathrm{s}}$ were interpolated using cubic splines. The trajectories of the spatio-temporal methods were directly obtained from the continuous 4D transforms. All trajectories were projected on the sagittal plane, where motion predominantly occurs. Overall, the obtained trajectories are quite similar. The spatio-temporal trajectories tend to be smoother than $\mathcal{T}_{\mathrm{s}}$. The main difference between $\mathcal{T}_{\mathrm{st}}$ and $\mathcal{T}^*_{\mathrm{st}}$ is visible at inhale (bottom of the plot). At this point, $\mathcal{T}^*_{\mathrm{st}}$ tends to be pointier and in some cases visibly closer to the corresponding landmark.

For Patients 1-3, landmarks were available for all frames of the 4D CT. The global registration accuracy in terms of the mean TRE based on 900 landmarks each, is summarized in table 4.3. For a $s = 2$ frames, the group mean TRE of both spatio-temporal methods was within 0.1 mm of $\mathcal{T}_{\mathrm{s}}$. When increasing the temporal control point spacing from 2 to 2.5, the TRE increased gradually (1.27 ± 1.17 mm for $\mathcal{T}^*_{\mathrm{st}}$ and 1.18 ± 1.03 mm for $\mathcal{T}^*_{\mathrm{st}}$), but remained comparable to $\mathcal{T}_{\mathrm{s}}$. For clarity, only results using a spacing of 2 frames will be shown in the following.

For Patients 1-3, the registration errors were also analyzed for each frame separately. Figure 4.4a corresponds to the group mean TRE of the entire 4D CT and figure 4.4b shows the group mean TRE per frame. The TRE of the entire 4D CT is comparable for all methods, though

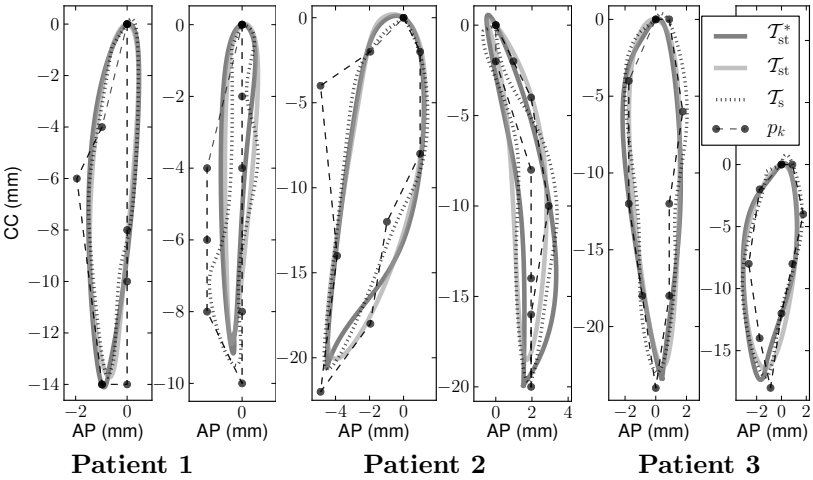

Figure 4.3: Trajectories projected on the sagittal plane, for some landmarks with large displacements of Patients 1-3. The trajectories obtained using the respective registration methods are compared with the manually identified landmark positions throughout the 4D CT. For all trajectories shown, at least two landmark positions coincided at exhale, corresponding to position (0,0).

Patient	TRE for 4D CT (mm)			
	Original	$\mathcal{T}_{\mathrm{s}}$	$\mathcal{T}_{\mathrm{st}}$	$\mathcal{T}^*_{\mathrm{st}}$
1	3.47 ± 2.14	0.96 ± 0.66	1.02 ± 0.71	1.00 ± 0.69
2	6.41 ± 3.99	1.20 ± 0.96	1.37 ± 1.13	1.27 ± 1.09
3	3.65 ± 3.04	1.11 ± 1.14	1.17 ± 1.08	1.16 ± 1.15
GM	4.51 ± 3.15	1.09 ± 0.94	1.19 ± 0.99	1.14 ± 1.00

Table 4.3: The mean TRE obtained over the nine frames for Patients 1-3 based on 900 landmarks each, and its group mean (GM). The registration error (± 1 SD) of the 3D registration is compared to the accuracy obtained for the spatio-temporal algorithms with $m = 3$ and $s = 2$ frames. The original landmark distance (*Original*) is given to illustrate illustrate the magnitude of the motion.

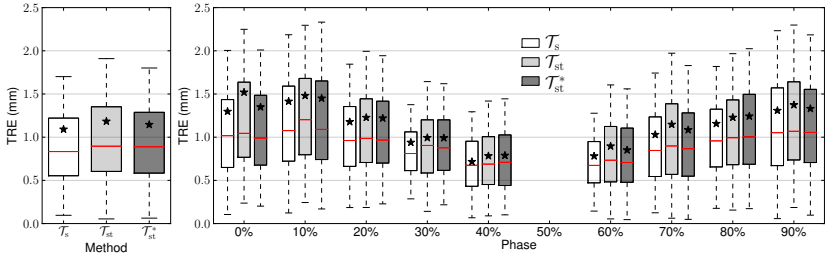

(a) (b)

Figure 4.4: Box and whisker plots of the group mean TRE for Patients 1-3 for which landmarks were available in all frames, using $m = 3$ and $s = 2$ frames. (a) The combined registration errors for the entire 4D registration. Each box is drawn based on 2700 landmarks. (b) TRE per phase bin. For each frame, the registration error is estimated from 300 landmarks. The 50% phase bin corresponds to the reference frame.

$\mathcal{T}_{\text{st}}$ performs slightly worse. The analysis per phase reveals that most discrepancies in TRE are found for phases near inhale (0%, 10% and 90 %). $\mathcal{T}_{\text{st}}^{*}$ generally obtains an accuracy closer to $\mathcal{T}_{\text{s}}$ for these phases.

A separate, more extensive evaluation of the accuracy of the end-exhale to end-inhale registration is listed in table 4.4 for Patients 1-6. $\mathcal{T}_{\text{st}}^{*}$ consistently outperforms $\mathcal{T}_{\text{st}}$ in terms of mean TRE. The performance of $\mathcal{T}_{\text{st}}^{*}$ is comparable to $\mathcal{T}_{\text{s}}$, the difference in group mean TRE was below 0.1 mm. In contrast, the difference in mean TRE between $\mathcal{T}_{\text{s}}$ and $\mathcal{T}_{\text{st}}$ was above 0.1 mm for five out of six patients, and the group mean TRE was almost 0.2 mm higher. This confirms the results reported for fitting the diaphragm motion data in section 4.4.1, where it was found that the smooth temporal model resulted in larger errors near end-inhale.

Table 4.3 shows relatively small differences in group mean TRE over the entire 4D CT, suggesting comparable performance for all registration methods. This measure was found misleading, as it tends to average out the differences due to the large numbers of measurements (2700 landmarks for each method). Further analysis showed that the performance of $\mathcal{T}_{\text{st}}$ varied considerably from patient to patient. While for Patient 1, all methods obtained very similar results, differences in mean TRE of the order of 0.5 mm were found at certain breathing phases for Patient 2 (figure 4.5, note the change in scale with respect to figure 4.4).

Patient	TRE for End-Inhale (mm)			
	Original	$\mathcal{T}_{\mathrm{s}}$	$\mathcal{T}_{\mathrm{st}}$	$\mathcal{T}^{*}_{\mathrm{st}}$
1	6.34 ± 2.94	0.94 ± 0.51	0.98 ± 0.56	0.96 ± 0.57
2	14.00 ± 7.17	1.44 ± 1.04	1.95 ± 1.88	1.56 ± 1.34
3	7.67 ± 5.03	1.51 ± 1.66	1.63 ± 1.66	1.53 ± 1.70
4	7.33 ± 4.86	1.79 ± 2.71	1.97 ± 3.00	1.96 ± 2.92
5	7.09 ± 5.08	1.43 ± 1.39	1.54 ± 1.49	1.48 ± 1.39
6	6.68 ± 3.67	1.18 ± 0.80	1.32 ± 1.13	1.25 ± 0.95
GM	8.19 ± 4.97	1.38 ± 1.53	1.57 ± 1.78	1.46 ± 1.65

Table 4.4: The mean TRE (± 1 SD) obtained by evaluating the registration only at the end-inhale for Patients 1-6 based on 100 landmarks each, and its group mean (GM). The registration error of the 3D registration ($\mathcal{T}_{\mathrm{s}}$) is compared to the accuracy obtained for the spatio-temporal algorithms ($\mathcal{T}_{\mathrm{st}}$ and $\mathcal{T}^{*}_{\mathrm{st}}$) using $m = 3$ and $s = 2$ frames. The original landmark distance (*Original*) is given to illustrate illustrate the magnitude of the motion.

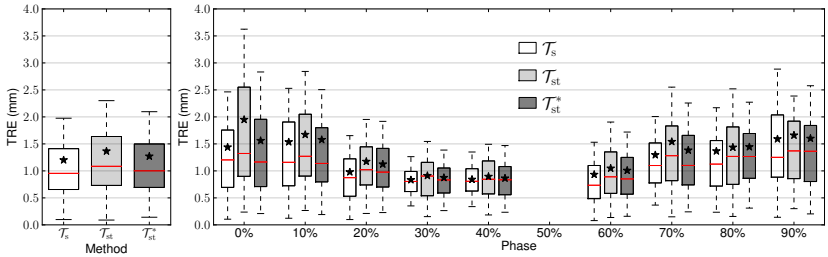

(a) (b)

Figure 4.5: Box and whisker plots of TRE for Patients 2 for which landmarks were available in all frames, using $m = 3$ and $s = 2$ frames. (*a*) The combined registration errors for the entire 4D registration. Each box is drawn based on 900 landmarks. (*b*) TRE per phase bin. For each frame, the registration error is estimated from 100 landmarks. The 50% phase bin corresponds to the reference frame.

Measure	Data	TRE (mm)		
		Original	$\mathcal{T}_{\mathrm{s}}$	$\mathcal{T}_{\mathrm{st}}^{*}$
global	f	9.00 ± 3.93	1.42 ± 1.30	1.44 ± 1.16
	f_{a}		3.17 ± 3.47	1.57 ± 1.20
local	f	11.40 ± 3.74	1.38 ± 1.44	1.46 ± 1.05
	f_{a}		6.82 ± 4.38	1.90 ± 1.22

Table 4.5: The mean TRE for the 4D CT sequence with simulated artifacts (f_{a}) and for the original, unmodified 4D CT (f) corresponding to Patient 2. The evaluation is limited to the frame where the artifact is introduced. The global TRE is based on 100 landmarks. The local TRE is based on 24 landmarks, all within 5 slices of the inserted artifact. The registration error of the 3D registration ($\mathcal{T}_{\mathrm{s}}$) is compared to the accuracy obtained for the spatio-temporal algorithm ($\mathcal{T}_{\mathrm{st}}^{*}$ using $m = 3$ and $s = 2$ frames). The original landmark distance (*Original*) is given to illustrate the magnitude of the motion.

4.4.3 Spatio-Temporal Registration of Artifacted 4D CT

The registration accuracy obtained for the artifacted sequence f_{a} is summarized in table 4.5. We only report results using the piecewise smooth spatio-temporal model $\mathcal{T}_{\mathrm{st}}^{*}$. We also list the TRE obtained for the original 4D CT, corresponding to Patient 2. With respect to the original 4D CT, the local and global TRE is within 0.1 mm for $\mathcal{T}_{\mathrm{s}}$ and $\mathcal{T}_{\mathrm{st}}^{*}$. After inserting the artifact, the global TRE more than doubles for $\mathcal{T}_{\mathrm{s}}$, while the TRE of the spatio-temporal method, increases only marginally. Locally, the influence of the artifact is even more noticeable for $\mathcal{T}_{\mathrm{s}}$. For the spatio-temporal approach however, the local TRE remains below 2 mm for $\mathcal{T}_{\mathrm{st}}^{*}$.

Figure 4.6 shows the motion fields obtained using $\mathcal{T}_{\mathrm{s}}$ and $\mathcal{T}_{\mathrm{st}}^{*}$ for the inner thoracic region. The top row corresponds to the original 4D CT acquisition of Patient 2. Both methods produce very similar motion fields. The main differences can be observed near the diaphragm. The bottom row corresponds to the artifacted sequence f_{a}. In this case, strong perturbations can be observed in the motion field obtained using $\mathcal{T}_{\mathrm{s}}$. The influence of the introduced artifact is also noticeable for $\mathcal{T}_{\mathrm{st}}^{*}$, but the changes in the motion field are less dramatic.

In figure 4.7, three examples are given of motion fields in the presence of real artifacts. The artifacts are shown in the first column and are

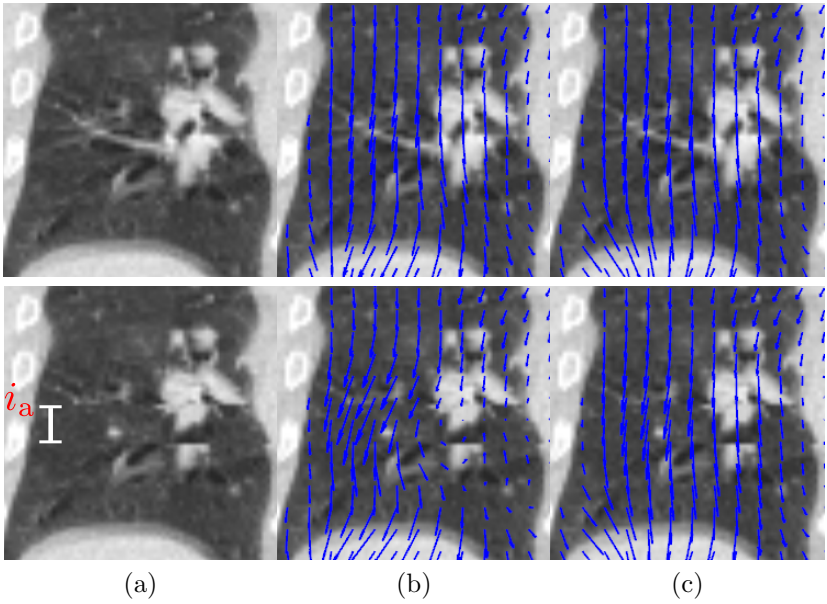

Figure 4.6: Motion fields in the presence of simulated artifacts: the top row corresponds to the original 4D CT acquisition of Patient 2, the bottom row corresponds to the modified sequence f_a in which an artifact was inserted. (*a*) Coronal view of images, i_a indicates the position of the artifact. Motion fields obtained for (*b*) $\mathcal{T}_s$ and (*c*) $\mathcal{T}_{st}^*$ using $m = 3$ and $s = 2$ frames.

generally most visible near the diaphragm. The second column shows the motion fields obtained using $\mathcal{T}_{\mathrm{s}}$. Strong perturbations can be seen, mainly in the part of the motion field that maps to artifacted region; that is, slightly above the location of the artifacts. The spatio-temporal approach tends to be less influenced by the artifacts. The resulting motion fields are noticeably smoother making them more plausible from a physiological point of view.

4.5 Discussion

Spatio-Temporal Registration The principal aim of this study was to develop a low-dimensional spatio-temporal deformation model, to improve robustness of the subsequent registration. We pursued a restrictive parametrization and strong temporal regularization, as these were expected to reduce sensitivity to noise and artifacts. The parametrization was thoroughly investigated, both spatially and temporally, to ensure an accurate representation of breathing motion was maintained.

Based on the fitting experiments of the diaphragm motion data, cubic temporal splines were found to perform best and selected for the temporal parametrization. The value of the temporal control point spacing s was found to represent a trade-off between achievable accuracy on one hand and an increase of parameters on the other, the latter likely to increase sensitivity to noise and artifacts. In practice its value should reflect the needs of the application and the quality of the images. Using $s = 2$, the spatio-temporal models obtained results comparable to the reference $\mathcal{T}_{\mathrm{s}}$ method, and was considered a suitable compromise for the 4D CT images dealt with in this study.

From a parametrization point of view, the $\mathcal{T}_{\mathrm{st}}$ model represents interesting characteristics. Minimal curvature is enforced throughout the entire cycle, and about a third less parameters are required with respect to $\mathcal{T}_{\mathrm{st}}^{*}$. Unfortunately, detailed analysis revealed larger TRE near end-inhale for $\mathcal{T}_{\mathrm{st}}$, indicating the smooth model fails to capture the full extent of the motion. Even though trajectories are expected to be smooth functions of time, a temporally smooth parametrization was found to be less efficient in terms of parameter reduction, due to the low temporal resolution of respiratory-correlated imaging. Using $\mathcal{T}_{\mathrm{st}^{*}}$ a uniform performance over the breathing cycle was obtained for all patients, and the group mean TRE was within 0.1 mm of the reference $\mathcal{T}_{\mathrm{s}}$, for both $s = 2$ and 2.5 frames.

The improved matching of $\mathcal{T}_{\mathrm{st}^{*}}$ at inhale comes at a price of two

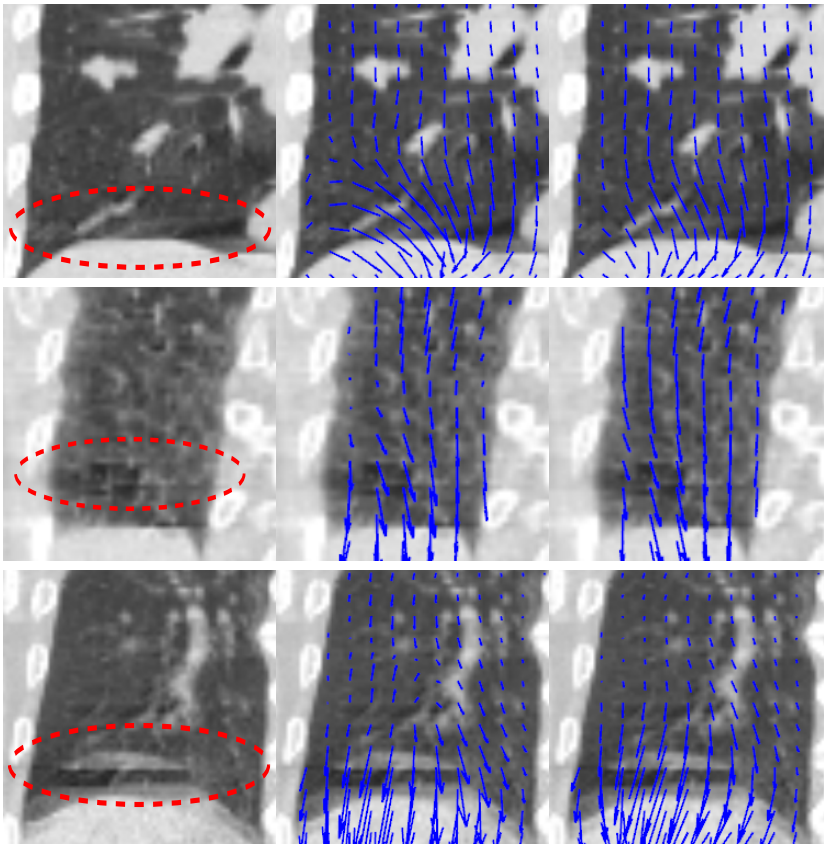

Figure 4.7: Three examples of motion fields in the presence of real artifacts (*a*) Coronal view of the images. Motion fields obtained for (*b*) $\mathcal{T}_{\mathrm{s}}$ and (*c*) $\mathcal{T}_{\mathrm{st}}^{*}$ using $m = 3$ and $s = 2$ frames.

additional temporal degrees of freedom with respect to the smooth model. Nonetheless, with respect to $\mathcal{T}_s$, this model reduces the number of parameters to be estimated during registration by 33% and 45% for $s = 2$ and 2.5 frames, respectively. The impact of the spatio-temporal parametrization was illustrated in the experiment in which a simulated motion-induced artifact was introduced in a 4D CT sequence. The motion field obtained using spatio-temporal registration was found to be considerably less influenced by the artifact, in comparison to the result obtained using $\mathcal{T}_s$.

Temporal parametrization The experiments presented here, indicate that the piecewise smooth representation was best suited to obtain a uniform matching accuracy across the breathing cycle. It should not be excluded that other piecewise models can be found, requiring less degrees of freedom, while obtaining a similar accuracy. These could consist in making sensible assumptions on the trajectory near inhale that can be translated into constraints, eliminating one or both of the additional degrees of freedom locally introduced.

From a constraints point of view, $\mathcal{T}_t^*$ is related to the trajectory model developed in (Castillo et al., 2010), where a compressible flow algorithm is extended with local trajectory modelling to perform 4D motion estimation for 4D CT. In this case however, one-way (and not cyclic) trajectories were sought between inhale and exhale, thus not requiring further attention at inhale. Cubic polynomials (equivalent to four degrees of freedom) were found to provide sufficient flexibility to parametrize the sought trajectories spanning six frames of the 4D CT. This corresponds well to the six degrees of freedom ($\mathcal{T}_{st}^*$ with a temporal control point spacing of 2) describing the trajectory over 10 frames.

The inhale phase, though also characterized with inversion of the motion, did not require further investigation of the constraints. It has been reported that respiratory motion tends to be asymmetrical (Kubo and Hill, 1996; Lujan et al., 1999; Seppenwoolde et al., 2002), spending more time near exhale then inhale. Phase bins near exhale, will represent relatively small deformation with respect to each other. Uniformly spacing control points with respect to these bins, will lead to a spatially higher control point density near exhale, allowing a more accurate representation, even in the presence of the smoothness constraints. This observation is confirmed by the trajectories depicted in figure 4.3, where two to three manually identified landmarks coincided with the exhale position.

Validity of the Spatio-Temporal Models In section 4.2, we made the assumption that the fourth image dimension was time. This allowed us to interpret $\mathcal{T}_t$ as a trajectory in function of time, and its derivatives as velocity and acceleration. In the case of 4D CT imaging, each frame is composed of data acquired at different times and different table positions. The interpretation of the fourth image dimension is closely related to the binning of acquired data, which is usually based on a surrogate signal.

The 4D CT data presented here was obtained from retrospective phase-based binning. The procedure consisted of detecting individual cycles by tagging the end-inhale position (local maximum) of the respiratory trace. For each cycle, a phase function linear with time was defined between consecutive tags from which the remainder of the phase tags are deduced. The reconstruction of each frame is performed by considering a fixed number of views around each relevant tag. Ignoring the non-periodic nature of breathing motion, and assuming a one-to-one relation between respiratory surrogate and motion, the images obtained in this fashion can be considered equivalent to a temporal sequence.

In practice, breathing motion is not periodic and the previously described approach leads to artifacts in presence of irregular breathing. In response, alternative criteria for binning (Lu et al., 2005; Abdelnour et al., 2007; Olsen et al., 2008; Zeng et al., 2008) or post-processing (Ehrhardt et al., 2007; Schreibmann et al., 2006; McClelland et al., 2006) of the acquired data have been proposed. While the framework remains applicable to the obtained sequences, the interpretation of the deformation model becomes less trivial. In addition, should the criteria become very different, the findings concerning the geometric constraints might no longer be valid. In practice, most criteria tend to be closely related to the breathing phase or processing is explicitly designed to be compatible with it (McClelland et al., 2006; Ehrhardt et al., 2007).

Influence of tagging and binning For both types of data presented, individual cycles were detected by tagging at inhale. This conveniently ensures that the end-inhale is accurately identified in the 4D CT, which is where the smoothness constraint needs to be relaxed during spatio-temporal registration. The diaphragm motion data was artificially made periodic at inhale, to allow fitting the cyclic trajectory models. This procedure can be held partly responsible for the rapid changes at inhale, and contributes to the fitting residuals. To quantify the effect, we repeated the experiments when tagging at exhale. Comparatively larger residuals were observed at exhale, indicating the influence of the tagging position.

The highest residuals were however still observed at inhale, confirming they are indeed caused by the sudden change in motion.

The experiments performed on the 4D CT sets and the diaphragm motion data, showed the same trends for the relative performances of the smooth and the piecewise smooth trajectory models. Comparatively larger discrepancies between the models were observed at inhale when fitting the diaphragm data. One reason is given by rendering the cycles periodic at inhale. Another explanation might lay in the fact that the diaphragm motion data has a considerably higher temporal resolution suggesting that, by binning the data into ten equi-temporal phase bins, the dynamics of the motion are partly averaged out over the 4D CT data.

Robustness to Artifacts Thoroughly evaluating the performance in the presence of artifacts is difficult due to the absence of a ground truth for the underlying image. The improved robustness of the spatio-temporal approach was therefore illustrated using a simple experiment based on simulated data, and through examples of motion fields for real artifacts. Further analysis of the behaviour of the spatio-temporal model in the presence of artifacts or noise is required. In particular the influence of aspects such as the temporal size and location of artifacts merits attention.

In the 3D (4.2) and 4D criterion (4.11), regularization terms penalizing undesirable properties of the deformation field were not included. The present study was limited to investigating the impact of explicit parametric restrictions. Regularization penalties will provide additional robustness and are expected to be complementary to parametric contributions. In addition, the spatio-temporal framework allows regularization schemes to be extended to the temporal dimension, as in (Brox et al., 2004).

Applications of Spatio-temporal Motion Analysis The spatio-temporal deformation model (4.10) was applied to 4D CT of the thorax in a 3D-4D registration framework. The model can also be applied to spatio-temporal motion analysis between sequences. By relaxing the condition (4.8) constraining the deformation at the reference frame, the model can be applied to a 4D-4D, frame-to-frame registration framework. By replacing criterion (4.11) with a suitable similarity measure, other modalities and even multi-modal problems can be studied.

This is similar to the 4D-4D registration method for respiratory-correlated images described in (Schreibmann et al., 2008) or the spatio-temporal alignment of cardiac sequences treated in (Perperidis et al., 2005). In comparison, our method assumes only frame-to-frame spatial

deformations without temporal shifts, and constrains deformations to a cyclic trajectory. These assumptions limit the degrees of freedom, and should be well suited to analyse motion patterns between for instance respiratory-correlated 4D CT, 4D cone-beam CT (Sonke et al., 2005) or 4D magnetic resonance (von Siebenthal et al., 2007).

4.6 Conclusion

We developed a spatio-temporal deformation model for deformable registration of respiratory-correlated images of the thorax. The model consists of an extension of spatial free-form deformations to the temporal domain, using a cyclic trajectory model based on cubic B-splines. A piecewise smooth temporal parametrization was found most suitable to account for the rapid changes in velocity at end-inhale. Spatio-temporal modelling resulted in a considerably more compact description of the deformation model. Spatio-temporal registration lead to comparable registration results and improved the robustness to artifacts.

Acknowledgement

The authors would like to thank Jan-Jakob Sonke of the Netherlands Cancer Institute-Antoni van Leeuwenhoek Hospital (Amsterdam, the Netherlands) for providing the cone-beam projection data, and Keelin Murphy of the Image Sciences Institute at the University of Utrecht (Utrecht, the Netherlands) for providing the sofware tool for landmark identification. Jef Vandemeulebroucke was funded by the EC Marie Curie grant WARTHE, Jan Kybic was sponsored by the Czech Ministry of Education, Project MSM6840770012.

References

A. F. Abdelnour, S. A. Nehmeh, T. Pan, J. L. Humm, P. Vernon, H. Schder, K. E. Rosenzweig, G. S. Mageras, E. Yorke, S. M. Larson, and Y. E. Erdi. Phase and amplitude binning for 4D-CT imaging. *Phys Med Biol*, 52(12): 3515–3529, Jun 2007.

T. Brox, A. Bruhn, N. Papenberg, and J. Weickert. High accuracy optical flow estimation based on a theory for warping. In *Computer Vision - ECCV 2004*, pages 25–36, 2004.

E. Castillo, R. Castillo, J. Martinez, M. Shenoy, and T. Guerrero. Four-dimensional deformable image registration using trajectory modeling. *Phys Med Biol*, 55(1):305–327, 2010.

R. Chandrashekara, R. H. Mohiaddin, and D. Rueckert. Analysis of 3-D myocardial motion in tagged MR images using nonrigid image registration. *IEEE Trans Med Imaging*, 23(10):1245–1250, Oct 2004.

P. Clarysse, C. Basset, L. Khouas, P. Croisille, D. Friboulet, C. Odet, and I. E. Magnin. Two-dimensional spatial and temporal displacement and deformation field fitting from cardiac magnetic resonance tagging. *Med Image Anal*, 4(3): 253–268, Sep 2000.

J. Declerck, J. Feldmar, and N. Ayache. Definition of a four-dimensional continuous planispheric transformation for the tracking and the analysis of left-ventricle motion. *Med Image Anal*, 2(2):197–213, Jun 1998.

B. Delhay, P. Clarysse, C. Pera, and I. Magnin. A spatio-temporal deformation model for dense motion estimation in periodic cardiac image sequences. In *From Statistical Atlases to Personalized Models: Understanding Complex Diseases in Populations and Individuals, Satellite Workshop MICCAI 2006*, pages in–press, Copenhagen, Denmark, October 2006.

J. Ehrhardt, R. Werner, D. Sring, T. Frenzel, W. Lu, D. Low, and H. Handels. An optical flow based method for improved reconstruction of 4D CT data sets acquired during free breathing. *Med Phys*, 34(2):711–721, Feb 2007.

E. C. Ford, G. S. Mageras, E. Yorke, and C. C. Ling. Respiration-correlated spiral CT: a method of measuring respiratory-induced anatomic motion for radiation treatment planning. *Med Phys*, 30(1):88–97, Jan 2003.

R. George, S. S. Vedam, T. D. Chung, V. Ramakrishnan, and P. J. Keall. The application of the sinusoidal model to lung cancer patient respiratory motion. *Med Phys*, 32(9):2850–2861, Sep 2005.

T. Guerrero, G. Zhang, W. Segars, T. Huang, S. Bilton, G. Ibbott, L. Dong, K. Forster, and K. Ping Lin. Elastic image mapping for 4-D dose estimation in thoracic radiotherapy. *Radiat Prot Dosimetry*, 115(1-4):497–502, 2005.

T. Guerrero, K. Sanders, E. Castillo, Y. Zhang, L. Bidaut, T. Pan, and R. Komaki. Dynamic ventilation imaging from four-dimensional computed tomography. *Phys Med Biol*, 51(4):777–791, Feb 2006.

J. Huang, D. Abendschein, V. G. Dvila-Romn, and A. A. Amini. Spatio-temporal tracking of myocardial deformations with a 4-D B-spline model from tagged MRI. *IEEE Trans Med Imaging*, 18(10):957–972, Oct 1999.

P. Keall. 4-dimensional computed tomography imaging and treatment planning. *Semin Radiat Oncol*, 14(1):81–90, Jan 2004.

M. L. Kessler. Image registration and data fusion in radiation therapy. *Br J Radiol*, 79 Spec No 1:S99–108, Sep 2006.

S. Klein, M. Staring, and J. P. W. Pluim. Evaluation of optimization methods for nonrigid medical image registration using mutual information and B-splines. *IEEE Trans Image Process*, 16(12):2879–2890, Dec 2007.

H. D. Kubo and B. C. Hill. Respiration gated radiotherapy treatment: a technical study. *Phys Med Biol*, 41(1):83–91, Jan 1996.

M. J. Ledesma-Carbayo, J. Kybic, M. Desco, A. Santos, M. Sühling, P. Hunziker, and M. Unser. Spatio-temporal nonrigid registration for ultrasound cardiac motion estimation. *IEEE Trans Med Imaging*, 24(9):1113–1126, Sep 2005.

D. A. Low, M. Nystrom, E. Kalinin, P. Parikh, J. F. Dempsey, J. D. Bradley, S. Mutic, S. H. Wahab, T. Islam, G. Christensen, D. G. Politte, and B. R. Whiting. A method for the reconstruction of four-dimensional synchronized CT scans acquired during free breathing. *Med Phys*, 30(6):1254–1263, Jun 2003.

W. Lu, P. J. Parikh, I. M. E. Naqa, M. M. Nystrom, J. P. Hubenschmidt, S. H. Wahab, S. Mutic, A. K. Singh, G. E. Christensen, J. D. Bradley, and D. A. Low. Quantitation of the reconstruction quality of a four-dimensional computed tomography process for lung cancer patients. *Med Phys*, 32(4): 890–901, Apr 2005.

W. Lu, G. H. Olivera, Q. Chen, M.-L. Chen, and K. J. Ruchala. Automatic re-contouring in 4D radiotherapy. *Phys Med Biol*, 51(5):1077–1099, Mar 2006.

A. E. Lujan, E. W. Larsen, J. M. Balter, and R. K. T. Haken. A method for incorporating organ motion due to breathing into 3D dose calculations. *Med Phys*, 26(5):715–720, May 1999.

J. R. McClelland, J. M. Blackall, S. Tarte, A. C. Chandler, S. Hughes, S. Ahmad, D. B. Landau, and D. J. Hawkes. A continuous 4D motion model from multiple respiratory cycles for use in lung radiotherapy. *Med Phys*, 33(9):3348–3358, Sep 2006.

J. C. McEachen, A. Nehorai, and J. S. Duncan. Multiframe temporal estimation of cardiac nonrigid motion. *IEEE Trans Image Process*, 9(4):651–665, 2000.

J. Modersitzki. *Numerical Methods for image Registration.* Oxford University Press, 2004.

J. Montagnat and H. Delingette. 4D deformable models with temporal constraints: application to 4D cardiac image segmentation. *Med Image Anal*, 9(1):87–100, Feb 2005.

K. Murphy, B. van Ginneken, J. P. W. Pluim, S. Klein, and M. Staring. Semi-automatic reference standard construction for quantitative evaluation of lung CT registration. *Med Image Comput Comput Assist Interv*, 11(Pt 2):1006–1013, 2008.

Nastar and Ayache. Frequency-based nonrigid motion analysis: application to four dimensional medical images. *IEEE Transactions on Pattern Analysis and Machine Intelligence*, 18(11):1067–1079, November 1996.

J. Nocedal. Updating quasi-newton matrices with limited storage. *Mathematics of computation*, 35(151):773–782, July 1980.

J. R. Olsen, W. Lu, J. P. Hubenschmidt, M. M. Nystrom, P. Klahr, J. D. Bradley, D. A. Low, and P. J. Parikh. Effect of novel amplitude/phase binning algorithm on commercial four-dimensional computed tomography quality. *Int J Radiat Oncol Biol Phys*, 70(1):243–252, Jan 2008.

C. Ozturk and E. R. McVeigh. Four-dimensional B-spline based motion analysis of tagged MR images: introduction and in vivo validation. *Phys Med Biol*, 45 (6):1683–1702, Jun 2000.

T. Pan, T.-Y. Lee, E. Rietzel, and G. T. Y. Chen. 4D-CT imaging of a volume influenced by respiratory motion on multi-slice CT. *Med Phys*, 31(2):333–340, Feb 2004.

D. Perperidis, R. H. Mohiaddin, and D. Rueckert. Spatio-temporal free-form registration of cardiac MR image sequences. *Med Image Anal*, 9(5):441–456, Oct 2005.

J. Peyrat, H. Delingette, M. Sermesant, C. Xu, and N. Ayache. Registration of 4D cardiac CT sequences under trajectory constraints with multichannel diffeomorphic demons. *IEEE Trans Med Imaging*, Mar 2010.

S. Rit, D. Sarrut, and L. Desbat. Comparison of analytic and algebraic methods for motion-compensated cone-beam CT reconstruction of the thorax. *IEEE Trans Med Imaging*, Feb 2009a.

S. Rit, M. van Herk, L. Zijp, and J.-J. Sonke. Intrafraction and interfraction variability of the respiratory motion amplitude. In *Proceedings of the 28th Annual ESTRO Meeting*, Maastricht, The Netherlands, 2009b.

D. Rueckert, L. I. Sonoda, C. Hayes, D. L. Hill, M. O. Leach, and D. J. Hawkes. Nonrigid registration using free-form deformations: application to breast MR images. *IEEE Trans Med Imaging*, 18(8):712–721, Aug 1999.

D. Sarrut. Deformable registration for image-guided radiation therapy. *Zeitschrift fr Medizinische Physik*, 16:285–297, 2006.

D. Sarrut and J. Vandemeulebroucke. B-LUT: Fast and low memory B-spline image interpolation. *To appear in Comput Methods Programs Biomed*, June 2010.

J. Schaerer, C. Casta, J. Pousin, and P. Clarysse. A dynamic elastic model for heart segmentation and motion estimation. *Submitted to Med Image Anal*, 2010.

A. Schmidt-Richberg, J. Ehrhardt, R. Werner, and H. Handels. Slipping objects in image registration: improved motion field estimation with direction-dependent regularization. *Med Image Comput Comput Assist Interv*, 12(Pt 1):755–762, 2009.

E. Schreibmann, G. T. Y. Chen, and L. Xing. Image interpolation in 4D CT using a BSpline deformable registration model. *Int J Radiat Oncol Biol Phys*, 64(5):1537–1550, Apr 2006.

E. Schreibmann, B. Thorndyke, T. Li, J. Wang, and L. Xing. Four-dimensional image registration for image-guided radiotherapy. *Int J Radiat Oncol Biol Phys*, 71(2):578–586, Jun 2008.

Y. Seppenwoolde, H. Shirato, K. Kitamura, S. Shimizu, M. van Herk, J. V. Lebesque, and K. Miyasaka. Precise and real-time measurement of 3D tumor motion in lung due to breathing and heartbeat, measured during radiotherapy. *Int J Radiat Oncol Biol Phys*, 53(4):822–834, Jul 2002.

J. Sonke, L. Zijp, P. Remeijer, and M. van Herk. Respiratory correlated cone beam CT. *Med Phys*, 32(4):1176–1186, Apr 2005.

J.-J. Sonke, J. Lebesque, and M. van Herk. Variability of four-dimensional computed tomography patient models. *Int J Radiat Oncol Biol Phys*, 70(2): 590–598, Feb 2008.

H. Sundar, H. Litt, and D. Shen. Estimating myocardial motion by 4D image warping. *Pattern Recognition*, 42(11):2514 – 2526, 2009. ISSN 0031-3203.

M. Unser. Splines: A perfect fit for signal and image processing. *IEEE Signal Processing Magazine*, 16(6):22–38, November 1999.

J. Vandemeulebroucke, O. Bernard, J. Kybic, P. Clarysse, and D. Sarrut. Automatic motion mask extraction for deformable registration of the lungs. In *XVIth International Conference on the Use of Computers in Radiation Therapy*, Amsterdam, June 2010.

S. S. Vedam, P. J. Keall, V. R. Kini, H. Mostafavi, H. P. Shukla, and R. Mohan. Acquiring a four-dimensional computed tomography dataset using an external respiratory signal. *Phys Med Biol*, 48(1):45–62, Jan 2003.

D. Visvikis, M. Ledesma-Carbayo, F. Lamare, O. Mawlawi, P. Jarritt, P. Bruyant, A. Santos, G. Kontaxakis, N. Boussion, and C. Cheze Le Rest. A spatiotemporal image registration algorithm for respiratory motion correction in PET/CT. *J Nucl Med, Meeting Abstracts*, 47(suppl 1):234P–a–, 2006.

M. von Siebenthal, G. Székely, U. Gamper, P. Boesiger, A. Lomax, and P. Cattin. 4D MR imaging of respiratory organ motion and its variability. *Phys Med Biol*, 52(6):1547–1564, Mar 2007.

J. W. H. Wolthaus, J. J. Sonke, M. van Herk, and E. M. F. Damen. Reconstruction of a time-averaged midposition CT scan for radiotherapy planning of lung cancer patients using deformable registration. *Med Phys*, 35(9):3998–4011, Sep 2008.

H. Wu, G. C. Sharp, Q. Zhao, H. Shirato, and S. B. Jiang. Statistical analysis and correlation discovery of tumor respiratory motion. *Phys Med Biol*, 52(16): 4761–4774, Aug 2007.

Z. Wu, E. Rietzel, V. Boldea, D. Sarrut, and G. C. Sharp. Evaluation of deformable registration of patient lung 4DCT with subanatomical region segmentations. *Med Phys*, 35(2):775–781, Feb 2008.

T. Yamamoto, U. Langner, B. W. Loo, J. Shen, and P. J. Keall. Retrospective analysis of artifacts in four-dimensional CT images of 50 abdominal and thoracic radiotherapy patients. *Int J Radiat Oncol Biol Phys*, 72(4):1250–1258, Nov 2008.

D. Yang, W. Lu, D. A. Low, J. O. Deasy, A. J. Hope, and I. E. Naqa. 4D-CT motion estimation using deformable image registration and 5D respiratory motion modeling. *Med Phys*, 35(10):4577–4590, Oct 2008.

R. Zeng, J. A. Fessler, J. M. Balter, and P. A. Balter. Iterative sorting for four-dimensional CT images based on internal anatomy motion. *Med Phys*, 35(3): 917–926, Mar 2008.

Q. Zhang, A. Pevsner, A. Hertanto, Y.-C. Hu, K. E. Rosenzweig, C. C. Ling, and G. S. Mageras. A patient-specific respiratory model of anatomical motion for radiation treatment planning. *Med Phys*, 34(12):4772–4781, Dec 2007.

T. Zhang, N. P. Orton, and W. A. Tom. On the automated definition of mobile target volumes from 4D-CT images for stereotactic body radiotherapy. *Med Phys*, 32(11):3493–3502, Nov 2005.

L. Zijp, J. Sonke, and M. van Herk. Extraction of the respiratory signal from sequential thorax cone-beam X-ray images. In *14th International Conference on the Use of Computers in Radiation Therapy, Seoul, Korea*, May 2004.

5

Respiratory Motion Estimation from Cone-Beam Projections Using a Prior Model

Jef Vandemeulebroucke[1,2,3], Jan Kybic[3], Patrick Clarysse[1] and David Sarrut[1,2]

[1]CREATIS, CNRS UMR5220, INSA-Lyon, University of Lyon, France

[2]Léon Bérard Cancer Center, University of Lyon, Lyon, France

[3]Center for Machine Perception, Czech Technical University in Prague, Czech Republic

Published in the proceedings of MICCAI, London, September 2009

Abstract Respiratory motion introduces uncertainties when planning and delivering radiotherapy for lung cancer patients. Cone-beam projections acquired in the treatment room could provide valuable information for building motion models, useful for gated treatment delivery or motion compensated reconstruction. We propose a method for estimating 3D+T respiratory motion from the 2D+T cone-beam projection sequence by including prior knowledge about the patient's breathing motion. Motion estimation is accomplished by maximizing the similarity of the projected view of a patient specific model to observed projections of the cone-beam sequence. This is done semi-globally, considering entire breathing cycles. Using realistic patient data, we show that the method is capable of good prediction of the internal patient motion from cone-beam data, even when confronted with interfractional changes in the breathing motion

Contents

5.1 Introduction

In radiotherapy, breathing motion causes uncertainties in the dose delivered to the tumour. The existing approaches to take respiratory motion into account include adding safety margins to ensure target coverage, breath-hold, gating, or tracking of the target (Keall et al., 2006). An important prerequisite to plan and evaluate treatment when using these techniques is a detailed knowledge of the motion. Four-dimensional (4D) computed tomography imaging (Ford et al., 2003) or cone-beam (CB) CT (Sonke et al., 2005), consisting of three dimensional (3D) frames each representing a breathing phase, can provide additional motion information. However, no intercycle variability can be measured as they represent a single respiratory cycle.

Breathing motion occurs predominantly in cranio-caudal direction and tends to be larger for the lower lobes (Keall et al., 2006). Trajectories of tumours and organs can be subject to hysteresis (Seppenwoolde et al., 2002), i.e. a different path is followed during inhalation and exhalation. Cycles can differ from one another in breathing rate and level (George et al., 2005); the latter influencing the amplitude of the motion. Variations in the mean tumour position (baseline) between and during fractions have also been reported (Seppenwoolde et al., 2002; Sonke et al., 2008).

Previously, 4D CT (Zhang et al., 2007) and cine CT volume segments covering multiple cycles (McClelland et al., 2006) have been used to model breathing motion. The small amount of acquired breathing cycles limits their ability to model intercycle variability. 4D MRI (von Siebenthal et al., 2007) covering more cycles could offer a solution to this problem. Regardless of the chosen approach, one should be able to detect and correct for interfractional changes in breathing motion that occur frequently between treatment sessions (Seppenwoolde et al., 2002; Sonke et al., 2008).

A CB projection sequence consists of a series of wide angle X-ray projections taken from rotating views around the patient. CBCT is routinely acquired for patient setup in many institutions, immediately before treatment, with the patient in the treatment position. Zijp et al. (2004) have a fast and robust method for extracting a respiratory phase signal from a CB projection sequence. By establishing a relation to a prior 4D CT, Rit et al. (2008) obtained a motion model that proved suitable for motion compensated CB reconstruction. Zeng et al. (2007) estimated motion from a projection sequence by deforming a reference CT image so that its projection views match the CB sequence. Optimization of the large number of parameters of a B-spline based deformation model

required adding aperiodicity penalties to the cost function to regularize the problem.

This article deals with *in situ* motion estimation from CB projection data for radiotherapy of lung cancer. With respect to (Zeng et al., 2007) we incorporate prior knowledge in the form of a patient-specific model, significantly reducing the number of parameters to be identified. No intercycle regularization is required and we obtain improvement in speed and robustness. Within-cycle smoothness is guaranteed automatically, through the use of a B-spline temporal model.

5.2 Method

First, a parametric patient-specific motion model with a small number of degrees of freedom is built from a 4D CT image routinely acquired preoperatively for the irradiation treatment planning of the considered patient group. The model is able to represent changes in the breathing phase in addition to small variations in breathing pattern. The model is then fitted to the CB projection sequence by optimizing the model parameters to maximize the similarity between the acquired 2D CB projections and simulated projection views of the model. Individual cycles are processed separately and a smooth motion estimate is found by simultaneously considering the whole cycle with suitable boundary conditions.

5.2.1 Motion Model

Using the demons algorithm (Thirion, 1998), which was available and well-understood in our group at the time of this study, we deformably register a manually chosen reference frame f_* to all other frames f_ϑ of the 4D CT, where $\vartheta \in [0;1)$ is the breathing phase. f_* should be chosen as to contain as little artifacts as possible. End-exhale is usually a good choice. Let $g_\vartheta(\boldsymbol{x})$ be the resulting deformation vector field, mapping f_* to f_ϑ. All deformation fields are averaged and a *mean position image* $\bar{f}$ is created by backward warping of f_* (Wolberg, 1990) (Figure 5.1a).

$$\bar{f}(\boldsymbol{x}) = f_*\left(\bar{g}^{-1}(\boldsymbol{x})\right) \quad \text{with} \quad \bar{g}(\boldsymbol{x}) = \frac{1}{b}\sum_{\theta=1}^{b} g_\theta(\boldsymbol{x}) \tag{5.1}$$

All structures appear at their time-weighted mean position in the image $\bar{f}$ (Wolthaus et al., 2008). Next, $\bar{f}$ is registered to the original frames f_ϑ.

The resulting deformation fields are represented using B-splines as

$$\begin{aligned} \mathcal{T}_{\vartheta,\alpha}(\boldsymbol{x}) &= \boldsymbol{x} + \alpha \sum_{\boldsymbol{i}} \sum_{j} a_{\boldsymbol{i}j}\, \beta^{n_{\boldsymbol{x}}}\left(\frac{\boldsymbol{x}-\boldsymbol{x_i}}{\Delta_{\boldsymbol{x}}}\right) \beta^{n_\vartheta}\left(\frac{\vartheta-\vartheta_j}{\Delta_\vartheta}\right) \\ &= \boldsymbol{x} + \alpha \mathcal{D}_\vartheta(\boldsymbol{x}) \end{aligned} \tag{5.2}$$

where $\beta^n(.)$ are B-splines placed at positions $\boldsymbol{x_i}$, ϑ_j with uniform spacing $\Delta_{\boldsymbol{x}}$, Δ_ϑ; $a_{\boldsymbol{i}j}$ are the B-spline coefficients. As ϑ varies from 0 to 1, the deformation model produces a motion corresponding to an entire breathing cycle starting from end-exhalation. Note that this allows to model hysteresis. The second parameter α is an instantaneous amplitude (it can vary with ϑ) and helps to model variations of the trajectory shape and breathing level. We chose cubic spline interpolation for phase space (n_ϑ=3). For the spatial dimension however, since dense deformation fields are available, a fast nearest neighbour ($n_{\boldsymbol{x}} = 0$) is employed. The coefficients $a_{\boldsymbol{i}j}$ are found quickly using digital filtering (Unser, 1999). Image $s_{\vartheta,\alpha}$ for a particular breathing state described by ϑ,α (Figure 5.1b) is obtained through forward warping (Wolberg, 1990) (where the subscript for $\mathcal{T}$ was omitted)

$$s_{\vartheta,\alpha}\big(\mathcal{T}(\boldsymbol{x})\big) = \bar{f}(\boldsymbol{x})\,. \tag{5.3}$$

5.2.2 Cost Function and Optimization Strategy

We propose to optimize the parameters of the model together for each breathing cycle. This renders the method more robust with respect to simply considering each projection separately (see Section 5.3), but is computationally more tractable than a truly global optimization (over many breathing cycles). Since breathing cycle extrema can usually be identified well, the accuracy is not compromised.

Given a CT volume f, an ideal cone-beam projection image p can be calculated using a linear projection operator $\mathcal{P}_\phi$ where the parameter ϕ fully describes the (known) camera position and orientation:

$$p = \mathcal{P}_\phi\, f \tag{5.4}$$

Figure 5.2a and 5.2b show a CB projection view of a mean position image $\bar{f}$ compared with a CB projection of the same patient. We measure similarity between an observed CB projection $\hat{p}$ and a modelled breathing state $s_{\vartheta,\alpha}$ by calculating the normalized correlation coefficient (NCC) in the 2D projection space:

$$J(\vartheta,\alpha;\phi) = \mathrm{NCC}(\hat{p}, \mathcal{P}_\phi s_{\vartheta,\alpha})\,. \tag{5.5}$$

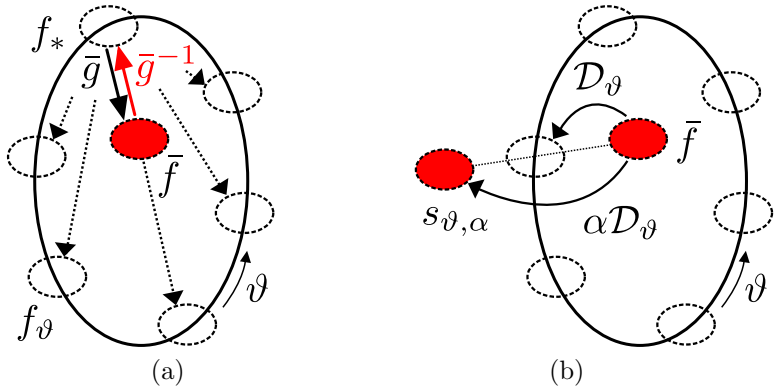

Figure 5.1: (a) The procedure for obtaining a mean position image $\bar{f}$. (b) A schematic representation of the representable space for the proposed model. Consider a point with position in $\bar{f}$ (*middle red oval*). Its position in all frames of the 4D CT (*white ovals*) is interpolated yielding the estimated breathing trajectory (*bold curve*). The amplitude parameter α allows to reach breathing states $s_{\vartheta,\alpha}$ off the trajectory.

Figure 5.2: (a) A simulated CB projection view calculated from the mean position image $\bar{f}$ and (b) a true CB projection of the same patient from the same viewpoint. Note that the images are very similar except for a horizontal reinforcement of the treatment table visible in the true CB projection. (c) Colour overlay of preregistered end-inhalation frames from the two 4D CT acquisitions of Patient 1.

In a first step, we detect the approximate time positions (projection indexes) t_e corresponding to extreme breathing phases (Zijp et al., 2004). The method is based on taking image derivatives and analyzing 1D projections of the obtained image. Second, we refine the parameters $\vartheta(t_e)$ and $\alpha(t_e)$ by minimizing

$$J\left(\vartheta(t_e), \alpha(t_e); \phi\right) + w\left(\vartheta(t_e) - \vartheta_e\right) \quad \text{with} \quad w(y) = \begin{cases} 0 & \text{for} |y| \leq h \\ \gamma |y|^2 & \text{otherwise} . \end{cases} \tag{5.6}$$

Note we are favouring solutions near the expected phase value ϑ_e. Powell-Brent (Press et al., 1992) multidimensional search was used with $h = 0.1$ and $\gamma = 20$ with initial values $\alpha(t_e) = 1$ and $\vartheta(t_e) = \vartheta_e = \vartheta_{ee}$ or ϑ_{ei} for end-exhalation and end-inhalation, respectively. The values for both ϑ_{ee} and ϑ_{ei} were determined by applying the extrema detection method (Zijp et al., 2004) to simulated projections of the model with slowly varying phase.

Let t_e and $t_{e'}$ be the two end-exhalation positions, the beginning and end of a breathing cycle. We have just shown how to get ϑ and α at t_e, $t_{e'}$, what remains is to obtain the estimates also for frames $t_{e+1}, \ldots, t_{e'-1}$. Assuming temporal smoothness, we propose to represent ϑ as

$$\vartheta(t) = \sum_{i=0}^{k} c_i \, \beta^{n_{\vartheta_t}} \left(\frac{t - t_i}{\Delta_{\vartheta_t}} \right) \quad \text{for} \quad t_e < t < t_{e'} \, , \tag{5.7}$$

where k is the number of control points, t_i are the temporal position of the knots, Δ_{ϑ_t} is the knot spacing and c_i are the B-spline coefficients. Fixing the value for $\vartheta(t_e)$ we can express the boundary coefficient c_0 as

$$c_0 = \frac{\vartheta(t_e) - \sum_{i=1}^{k} c_i \beta^{n_{\vartheta_t}} \left(\frac{t_e - t_i}{\Delta_{\vartheta_t}} \right)}{\beta^{n_{\vartheta_t}} \left(\frac{t_e - t_0}{\Delta_{\vartheta_t}} \right)} \, , \tag{5.8}$$

and similarly for c_k. A B-spline expansion with coefficients d_j is used to represent $\alpha(t)$. By summing the contributions for m different time instances within the cycle and using equations (5.5),(5.7–5.8), we obtain the following similarity measure:

$$J^t(\boldsymbol{c}, \boldsymbol{d}) = \frac{1}{m} \sum_{t=1}^{m} J\left(\vartheta(t_e + t), \alpha(t_e + t); \phi(t_e + t)\right) \, . \tag{5.9}$$

We find the coefficients $\boldsymbol{c} = [c_1, \ldots, c_k], \boldsymbol{d} = [d_1, \ldots, d_l]$ by minimizing J^t, using a Nelder-Nead downhill simplex algorithm (Press et al., 1992),

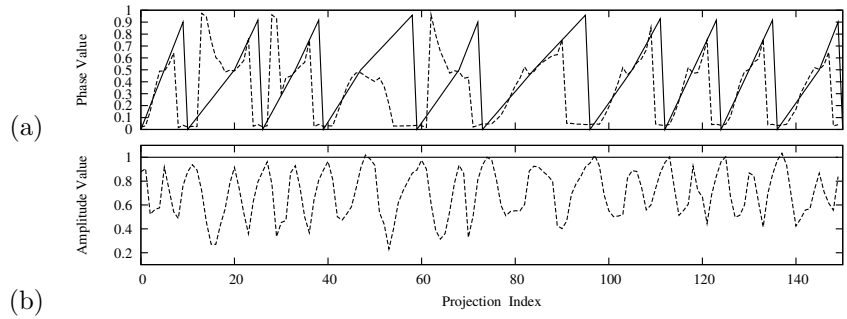

Figure 5.3: Results of sequential motion estimation for Patient 1: the recovered phase (a) and amplitude (b) (*dashed line*) together with the parameters used to generate the CB sequence (*full line*). The reference amplitude is a constant, $\alpha = 1$.

which performed well in this high dimensional search space, requiring less iterations than Powell-Brent and yielding comparable results. A linear progression is used as a starting point. We use a quadratic B-spline representation ($n_{\vartheta_t} = n_{\alpha_t} = 2$) with $k = l = 4$.

5.3 Experiments and Results

Accurately evaluating the 2D-3D motion estimation is very difficult, as no ground truth is available. In this work we use pairs of 4D CT sequences acquired for three lung cancer patients using a Philips Brilliance BigBore 16-slice CT scanner (Philips Medical Systems, Cleveland, OH). The time between acquisitions ranged from 20 minutes (Patient 1 and 2) to 3 days (Patient 3). Patients 1 and 2 were asked to stand up from the acquisition table and walk around for 10 minutes before repositioning and acquisition of the second 4D CT. In spite of the small time between the acquisitions, substantial differences can be observed between the two subsequent 4D CT acquisitions due to interfractional changes in breathing motion (see Figure 5.2c). We used the first 4D CT sequence to construct a patient model as described in Section 5.2.1. The second acquisition was first rigidly registered to the first 4D CT to align the bony structures. In order to have a ground truth available, we took the mean position image from the first sequence and the deformation fields from the second sequence to get a simulated reference 4D CT sequence. A respiratory trace was randomly

(mm)	original			residual		
	μ	σ	max	μ	σ	Max
Patient 1	3.8	2.1	17.1	1.1	0.6	8.3
Patient 2	2.8	1.7	16.1	1.6	0.8	11.0
Patient 3	3.7	1.6	13.8	1.3	0.7	5.8

Table 5.1: Results of the semi-global motion estimation. The residual misalignment (*residual*) between the found and the true motion: the mean (μ), standard deviation (σ) and maximum (*max*) is compared to the original motion with respect to $\bar{f}$ (*original*).

generated (George et al., 2005) and a piecewise linear phase signal $\vartheta(t)$ with variable breathing rate was derived. We simulated the first 90° of a CB acquisition protocol in our institute by calculating 150 projections for evenly spaced angles from the reference 4D CT with varying phase value over a period of 30 s.

When optimizing separately for each projection the criterion (5.5) with respect to ϑ and α, we obtained bad results when confronted to interfractional changes in breathing motion (see Figure 5.3, results for other patients were similar). Note that an optimal result doesn't necessarily mean recovering identical parameter values as they correspond to different deformation fields. In this case however, we can observe how intermediate phases during inhalation ($\vartheta \approx 0.2$) and exhalation ($\vartheta \approx 0.8$) are confused, due to limited hysteresis and unfavourable projection angle and are accompanied with strong variations in amplitude.

The phase and amplitude found for Patient 3 using our semi-global criterion (5.9) are shown in Figure 5.4a and 5.4b, together with the parameters used to generate the CB sequence. To evaluate the accuracy we calculate the residual geometric misalignment (i.e. the norm of the difference between deformation vector fields) between the estimated motion and the true motion. This measure is averaged over the lower lung, where the largest motion tends to occur. For comparison, the original misalignment, i.e. the motion with respect to the mean position image, is also given. Table 5.1 contains the average over all projections for each patient. Figure 5.4c shows this mean misalignment as a function of the projection index for Patient 3. Note that while displacement might locally attain 3cm, the average motion as seen from the mean position does not exceed 1cm.

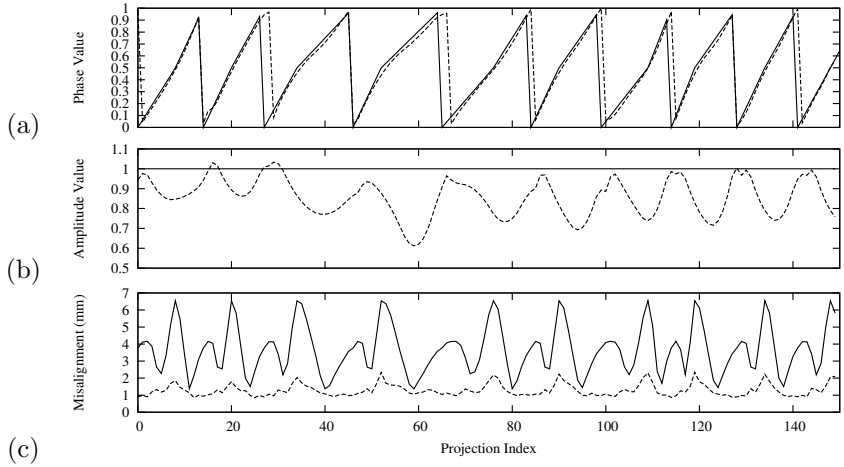

Figure 5.4: Results of the semi-global motion estimation for Patient 3: the recovered phase (a) and amplitude (b) (*dashed line*) are shown together with the parameters used to generate the CB sequence (*full line*). The reference amplitude is a constant, $\alpha = 1$. (c) The resulting residual misalignment (*dashed line*) is shown in comparison with the original misalignment with respect to the mean position image (*full line*).

5.4 Discussion and Conclusion

We achieved a smooth motion estimation from a CB projection sequence using B-splines and by considering the complete movement in a respiratory cycle and obtained a considerable reduction of the original misalignment for all patients.

To our knowledge this is the first time a respiratory motion model is tested against clinical data containing real interfractional changes in breathing motion. Some additional challenges presented by real CB data will include dealing with scatter (Zeng et al., 2007) and detecting and correcting for rigid misalignment (setup errors).

As a consequence of generating the ground truth, baseline shifts were not present in our patient data. Changes in breath rate, breathing level or trajectory shape were however present. It is expected that the method will be able to cope with small shifts ($< 20\%$ of the motion amplitude). For larger shifts, a prior shift estimation can be performed, e.g. from a 4D CBCT (Sonke et al., 2005).

In this work we exploited only acquisitions already acquired for treatment purposes. More preoperative data, such as breath hold CT scans (McClelland et al., 2006; Zeng et al., 2007) or MRI data (von Siebenthal et al., 2007), could further improve the prior model, rendering it's construction more robust to artifacts and providing prior information on the intercycle variation.

Acknowledgement

Jef Vandemeulebroucke was funded by the EC Marie Curie grant WARTHE, Jan Kybic was sponsored by the Czech Ministry of Education, Project MSM6840770012.

References

E. C. Ford, G. S. Mageras, E. Yorke, and C. C. Ling. Respiration-correlated spiral CT: a method of measuring respiratory-induced anatomic motion for radiation treatment planning. *Med Phys*, 30(1):88–97, Jan 2003.

R. George, S. S. Vedam, T. D. Chung, V. Ramakrishnan, and P. J. Keall. The application of the sinusoidal model to lung cancer patient respiratory motion. *Med Phys*, 32(9):2850–2861, Sep 2005.

P. J. Keall, G. S. Mageras, J. M. Balter, R. S. Emery, K. M. Forster, S. B. Jiang, J. M. Kapatoes, D. A. Low, M. J. Murphy, B. R. Murray, C. R. Ramsey, M. B. V. Herk, S. S. Vedam, J. W. Wong, and E. Yorke. The management of respiratory motion in radiation oncology report of AAPM task group 76. *Med Phys*, 33(10):3874–3900, Oct 2006.

J. R. McClelland, J. M. Blackall, S. Tarte, A. C. Chandler, S. Hughes, S. Ahmad, D. B. Landau, and D. J. Hawkes. A continuous 4D motion model from multiple respiratory cycles for use in lung radiotherapy. *Med Phys*, 33(9):3348–3358, Sep 2006.

W. H. Press, B. P. Flannery, S. A. Teukolsky, and W. T. Vetterling. *Numerical Recipes in C.* Cambridge University Press, second edition, 1992.

S. Rit, J. Wolthaus, M. van Herk, and J.-J. Sonke. On-the-fly motion-compensated cone-beam CT using an a priori motion model. *Med Image Comput Comput Assist Interv*, 11(Pt 1):729–736, 2008.

Y. Seppenwoolde, H. Shirato, K. Kitamura, S. Shimizu, M. van Herk, J. V. Lebesque, and K. Miyasaka. Precise and real-time measurement of 3D tumor motion in lung due to breathing and heartbeat, measured during radiotherapy. *Int J Radiat Oncol Biol Phys*, 53(4):822–834, Jul 2002.

J. Sonke, L. Zijp, P. Remeijer, and M. van Herk. Respiratory correlated cone beam CT. *Med Phys*, 32(4):1176–1186, Apr 2005.

J.-J. Sonke, J. Lebesque, and M. van Herk. Variability of four-dimensional computed tomography patient models. *Int J Radiat Oncol Biol Phys*, 70(2): 590–598, Feb 2008.

J. P. Thirion. Image matching as a diffusion process: an analogy with Maxwell's Demons. *Med Image Anal*, 2(3):243–260, Sep 1998.

M. Unser. Splines: A perfect fit for signal and image processing. *IEEE Signal Processing Magazine*, 16(6):22–38, November 1999.

M. von Siebenthal, G. Székely, U. Gamper, P. Boesiger, A. Lomax, and P. Cattin. 4D MR imaging of respiratory organ motion and its variability. *Phys Med Biol*, 52(6):1547–1564, Mar 2007.

G. Wolberg. *Digital image warping.* IEEE Computer Society Press, Los Alamitos, CA,, 1990.

J. W. H. Wolthaus, J. J. Sonke, M. van Herk, and E. M. F. Damen. Reconstruction of a time-averaged midposition CT scan for radiotherapy planning of lung cancer patients using deformable registration. *Med Phys*, 35(9):3998–4011, Sep 2008.

R. Zeng, J. A. Fessler, and J. M. Balter. Estimating 3-D respiratory motion from orbiting views by tomographic image registration. *IEEE Trans Med Imaging*, 26(2):153–163, Feb 2007.

Q. Zhang, A. Pevsner, A. Hertanto, Y.-C. Hu, K. E. Rosenzweig, C. C. Ling, and G. S. Mageras. A patient-specific respiratory model of anatomical motion for radiation treatment planning. *Med Phys*, 34(12):4772–4781, Dec 2007.

L. Zijp, J. Sonke, and M. van Herk. Extraction of the respiratory signal from sequential thorax cone-beam X-ray images. In *14th International Conference on the Use of Computers in Radiation Therapy, Seoul, Korea*, May 2004.

6

2D-3D Deformable Registration for Monitoring Baseline Variations

Abstract The advent of cone-beam computed tomography and arc therapy has made it technically feasible to acquire cone-beam projections between and during treatment beams. Baseline variations of the tumour have been reported to occur frequently, between and during treatment fractions. This type of lung motion has a potentially large dosimetric impact if not properly accounted for. We describe a method for monitoring baseline variations with respect to a reference image, from a selection of cone-beam projections acquired over a limited arc. The sought deformation is represented as a B-spline deformable transform whose dimensionality is reduced by including physiological priors.The method consists of measuring the similarity between the projections and the projection views of the reference image. An efficient computation is obtained by integrating the projection information over the image space. We perform a feasibility study using repeat CT acquisitions of the same patient, allowing to simulate a projection sequence representing real interfractional changes with respect to the reference image. Results were promising, showing a considerable reduction of initial misalignment. Further research is required to assess the utility of the method.

Contents

6.1 Introduction

Cone-beam computed tomography (CBCT) (Jaffray et al., 1999, 2002) has become widely adopted for soft tissue imaging before treatment delivery of highly conformal radiotherapy. Intensity modulated arc therapy (IMAT) (Yu, 1995; Duthoy et al., 2004) recently became commercially available, and improves conformity of the high-dose region with the target while offering a considerable speed-up of treatment delivery. These advancements have made it technically feasible to acquire projections just before treatment, between treatment beams or during arc therapy delivery. The availability of large amounts of patient data, in addition to possible future applications involving imaging during treatment delivery, has increased the interest in optimizing the use of CBCT. Research is focussed on one hand on optimizing reconstruction and use of CBCT. For many clinical applications, a full 3D image is not required. An alternative, but highly interesting path of investigation is therefore similarly being pursued in directly exploiting projections or subsets of projections from a rotational projection series. Dose methods could potentially reduce the imaging dose to the patient, or extend the use of rotational projections.

Several authors have explored the utility of cone-beam projections for tumour tracking using implanted, radiopaque markers. The markers can be detected quickly and reliably in the X-ray projection views and their motion is used as a surrogate for tumour motion. The tracking results in valuable motion data, useful for characterizing intra- and interfactional tumour motion (Marchant et al., 2008; Poulsen et al., 2008). Alternatively these approaches could enable strategies for simultaneous tracking and arc treatment delivery (Poulsen et al., 2010). Two significant drawbacks of implanted marker tracking are risks of clinical complications such as pneumothorax (Geraghty et al., 2003), and the possibility of marker migration (Nelson et al., 2007). Markerless tumour tracking from cone-beam projections has therefore also been explored, but is challenging because the tumour is hard to identify in the X-ray images. Fluoroscopic tracking generally relies on patient-specific training data to be acquired for the considered projection angle (Lin et al., 2009), which is unpractical for the 3D cone-beam geometry. Alternatively, template matching using templates previously calculated from 4D CT has been investigated (Lewis et al., 2010; Hugo et al., 2010).

A different type of studies has focussed on reconstructing volumetric images from subsets of projections acquired over short rotational arcs (typically 45-90°), termed tomosynthesis. This image modality has mostly

been applied to breast cancer screening (Niklason et al., 1997), but its utility has been illustrated for image guidance in radiotherapy as well (Tutar et al., 2003; Godfrey et al., 2006). Related to this is the work of Tomazevic et al. (2006) on reconstruction based 3D-2D registration. The problem is approached by reconstructing a 3D image from a limited number of 2D views (though generally over a larger arc than 90°). The registration is subsequently performed in 3D space by estimating the optimal spatial correspondence between the reconstructed image and the reference 3D image, and by using specific similarity measures to account for the reduced image quality (Skerl et al., 2006).

A last line of research lies in directly relating cone-beam projections to a reference CT or 4D CT. Such methods have been used for some time, mostly for rigid alignment. More recently, projections acquired during arc rotations have been used to estimate breathing motion and deformation parameters (Blondel et al., 2004; Zeng et al., 2005; Li et al., 2006; Zeng et al., 2007; Vandemeulebroucke et al., 2009; Long et al., 2010) (see also section 1.2.4.3). The potential of these methods becomes clear, when considering the low amount of information needed to estimate the position, pose or motion of a patient. Lung motion quantification from cone-beam projections, would make a large amount of patient data available for motion characterization, which is currently unexploited for these purposes. The reduced amount of data required for motion estimation, also offers a potential increase in the temporal updates of the patient state during treatment delivery. The latter is our main ambition in this study.

In this study, we explore the feasibility of updating a patient state, represented by a reference CT image, by relating it to a limited amount of cone-beam projections. More specifically we aim at estimating the 3D deformation, that is present between the reference image and the in-room projection views of the patient. The reference image could be a previous acquisition representing the patient at exhale, at its time-weighted mean position (Wolthaus et al., 2008) or could simply be the image used during treatment planning. Similarly, the set of projection sequences could be a continuous series of rotational X-ray projections, or a subset representative of the breathing state of interest. Several methods for extracting breathing phases for cone-beam projection sequences are available (Zijp et al., 2004; Rit et al., 2005), and their performance and influence on the resulting motion estimate will not be considered here. The set of projections is simply assumed to represent the patient state of interest.

Our main application is the detection of baseline variations, known to occur during and between treatment fractions (Seppenwoolde et al.,

2002; Purdie et al., 2007; Sonke et al., 2008). This type of lung motion causes a shift in mean target position, which is different from the pseudo-periodic motion of thoracic structures due to breathing motion. If not properly accounted for, the dosimetric impact of baseline variations can be substantial (Sonke et al., 2008). In the following we are assuming that periodic imaging is available during treatment, either between beams (for instance, over the arc length required to reposition the high-energy source for the next beam) or during delivery of arc treatment. The provided patient update can thus be seen as intrafraction monitoring of the patient state. Alternatively, the method could be useful to provide an initial estimate of potential baseline shifts, enabling subsequent respiratory motion estimation from the cone-beam projection sequence as described in chapter 5.

While the method presented in the following sections was fully implemented, the study was not fully completed due to time restrictions. The experiments performed were therefore inconclusive on the potential of the approach, in particular with respect to other approaches reported in literature. The full description of the method is given, mainly for future reference, and is completed by a simple feasibility study.

6.2 Method

6.2.1 Problem Description

Suppose we dispose of a 3D CT reference image of the patient $f_\mathrm{r}(\boldsymbol{i}) \in \mathbb{R}$ with $\boldsymbol{i} \in \mathbf{I} \subset \mathbb{Z}^3$ the 3D index space. Consider now a projection sequence $\boldsymbol{p}$, composed of $N_\mathbf{K}$ 2D X-ray projection views $p_k(\boldsymbol{u}) \in \mathbb{R}$ with $\boldsymbol{u} \in \mathbf{U} \subset \mathbb{Z}^2$ the 2D index space of the projection and $k \in \mathbf{K} \in \mathbb{Z}$ the set of temporal indices. For each of the projection views, the projection geometry is assumed to be fully known, providing us with the relation between the indices $\boldsymbol{i}$ and $\boldsymbol{u}$.

The goal is to estimate the 3D non-rigid transformation $\mathcal{T}_\delta(\boldsymbol{x}) \in \mathbb{R}^3$ with $\boldsymbol{x} \in \mathbf{X} \subset \mathbb{R}^3$ the continuous 3D coordinate, that is required to align f_r with the projection sequence $\boldsymbol{p}$.

6.2.2 Spatial Transformation

We express the sought transformation as the combination of the identity transform and a shift δ which is a function of $\boldsymbol{x}$

$$\mathcal{T}_\delta(\boldsymbol{x}) = \boldsymbol{x} + \delta(\boldsymbol{x}) \,. \tag{6.1}$$

Little is known about the spatial representation of baseline variations. Studies have mainly focussed on the tumour, and reported shifts in all three dimensions (Seppenwoolde et al., 2002; Sonke et al., 2008). To ensure a flexible representation, we retain a deformable transformation based on B-splines (Rueckert et al., 1999). However, baseline variations are suspected to be mainly caused unintentionally, as a result of gradual patient relaxation, changes in stomach filling or muscle tone (Shirato et al., 2004). Based on these physiological considerations we make the following two assumptions. The first is that δ is limited to spatially (very) smooth deformations. The second assumption is that this *passive* phenomenon does not affect the intercostal muscles and thoracic cage, but only the inner thoracic structures.

Making use of the method described in chapter 3, we first extract the subregion $\mathbf{I}_{\text{in}} \subset \mathbf{I}$ from f_{r}, corresponding to the lungs, mediastinum and abdomen. This allows us to propose the following piecewise smooth definition for δ, based on free-form deformations

$$\delta(\boldsymbol{x}) = \begin{cases} \sum_{\boldsymbol{j} \in \mathbf{J}} \boldsymbol{a}_{\boldsymbol{j}} \beta^n(\boldsymbol{x}/h - \boldsymbol{j}) & \text{for } \lfloor \boldsymbol{x} \rceil \in \mathbf{I}_{\text{in}} \\ 0 & \text{elsewhere} \end{cases} . \tag{6.2}$$

In this equation, $\lfloor \boldsymbol{x} \rceil$ represents the operation of rounding $\boldsymbol{x}$ to the nearest index, $\boldsymbol{j} \in \mathbf{J}$ is the set of spatial indices, $\beta^n(\boldsymbol{x})$ is tensor product of centered B-spline kernels of degree n (we used cubic B-splines, $n = 3$), $h \in \mathbb{R}$ is the uniform B-spline control point spacing, and the $\boldsymbol{a}_{\boldsymbol{j}} \in \mathbb{R}^3$ are the B-spline coefficients characterizing the transformation. $\mathcal{T}_\delta$ can be used to transform the reference image f_{r}, obtaining the deformed image f_δ

$$f_\delta(\boldsymbol{i}) = f_{\text{r}}\big(\mathcal{T}_\delta(\boldsymbol{i})\big) , \tag{6.3}$$

in which it was assumed that we can evaluate the intensity function f_{r} at non-grid positions. We used cubic B-splines to provide the required intensity interpolation.

6.2.3 Similarity Measure

What remains to be defined is the method for measuring similarity between the 3D image f_δ, and the set of 2D projections $\boldsymbol{p}$. We make use of the known projection geometries to define the projection operator $\mathcal{A}_k$ associated to the projection p_k. Using the CT imaging principle (Macovski, 1983), this allows us to calculate the 2D projection view, $g_{\delta,k}(\boldsymbol{u}) \in \mathbb{R}$, of the deformed volume f_δ

$$g_{\delta,k} = \mathcal{A}_k f_\delta . \tag{6.4}$$

We propose to measure similarity between *measured* projection p, and a *simulated* projection view g by calculating the normalized correlation coefficient $\mathcal{J}$ in the 2D projection space $\mathbf{U}$

$$\mathcal{J}(p,g) = -1 \times \frac{\sum_{\boldsymbol{u}\in\mathbf{U}} \big((p(\boldsymbol{u}) - \bar{p})(g(\boldsymbol{u}) - \bar{g})\big)}{\sqrt{\big(\sum_{\boldsymbol{u}\in\mathbf{U}}(p(\boldsymbol{u}) - \bar{p})^2\big)\big(\sum_{\boldsymbol{u}\in\mathbf{U}}(g(\boldsymbol{u}) - \bar{g})^2\big)}}\,, \tag{6.5}$$

in which $\bar{p}$ is the mean intensity, calculated over the $N_{\mathbf{U}}$ samples of the projection space $\mathbf{U}$, i.e.

$$\bar{p} = \frac{1}{N_{\mathbf{U}}} \sum_{\boldsymbol{u}\in\mathbf{U}} p(\boldsymbol{u})\,. \tag{6.6}$$

The criterion (6.5) is negated to obtain a minimization problem. Extending this principle to take into account all measured projections, similarity between the deformed image f_δ and the $N_{\mathbf{K}}$ projections of $\boldsymbol{p}$ is computed as follows

$$\mathcal{J}_{\mathrm{m}}(\boldsymbol{p}, f_\delta) = \frac{1}{N_{\mathbf{K}}} \sum_{k\in\mathbf{K}} \mathcal{J}(p_k, g_{\delta,k})\,. \tag{6.7}$$

6.2.4 Optimization

Using the definitions of the previous sections, the problem of estimating the deformation between the reference image f_{r} and the set of measured projections $\boldsymbol{p}$ comes down to estimating the set of parameters $\boldsymbol{a}^*$, optimal in the sense of the defined criterion $\mathcal{J}_{\mathrm{m}}$

$$\boldsymbol{a}^* = \arg\min_{\boldsymbol{a}} \mathcal{J}_{\mathrm{m}}(\boldsymbol{p}, f_\delta)\,. \tag{6.8}$$

A coarse to fine multiresolution approach is employed to solve problem (6.8), in which the resolution of the 2D and 3D images and of the B-spline control point grid δ, is double in each resolution level. The final image resolution for the projection images was 1×1 mm^2 and $2\times2\times2$ mm^3 for the 3D image.

Each level was handled by limited memory implementation of the BFSG (Nocedal, 1980) optimization strategy. The partial derivatives to the parameters can be found as follows

$$\frac{\partial \mathcal{J}_{\mathrm{m}}(\boldsymbol{p}, f_\delta)}{\partial \boldsymbol{a}} = \frac{1}{N_{\mathbf{K}}} \sum_{k\in\mathbf{K}} \sum_{\boldsymbol{u}\in\mathbf{U}} \frac{\partial \mathcal{J}(p_k, g_{\delta,k})}{\partial g_{\delta,k}(\boldsymbol{u})} \frac{\partial g_{\delta,k}(\boldsymbol{u})}{\partial \boldsymbol{a}} \tag{6.9}$$

with

$$\frac{\partial \mathcal{J}(p,g)}{\partial g(\boldsymbol{u})} = \frac{-1}{\sqrt{\left(\sum_{\boldsymbol{v}\in\mathbf{U}}(p(\boldsymbol{v})-\bar{p})^2\right)\left(\sum_{\boldsymbol{v}\in\mathbf{U}}(g(\boldsymbol{u})-\bar{g})^2\right)}} \left((p(\boldsymbol{u})-\bar{p}) - (g(\boldsymbol{u})-\bar{g})\frac{\sum_{\boldsymbol{v}\in\mathbf{U}}(p(\boldsymbol{v})-\bar{p})(g(\boldsymbol{v})-\bar{g})}{\sum_{\boldsymbol{v}\in\mathbf{U}}(g(\boldsymbol{v})-\bar{g})^2}\right) \quad (6.10)$$

and

$$\frac{\partial g_{\delta,k}}{\partial \boldsymbol{a}} = \mathcal{A}_k \frac{\partial f_\delta}{\partial \boldsymbol{x}} \frac{\partial \mathcal{T}_\delta}{\partial \boldsymbol{a}} \,. \quad (6.11)$$

From (6.9), it can be seen that calculating the partial derivatives initially involves $N_{\mathbf{K}}$ projections for computing $g_{\delta,k}$, required for the calculation of (6.10). The second factor in the multiplication in (6.9) is less trivial. From (6.11) it can be seen that integrating its contribution over the 2D projection space requires the projection of $\frac{\partial f_\delta}{\partial \boldsymbol{x}}\frac{\partial \mathcal{T}_\delta}{\partial \boldsymbol{a}}$ which is a vectorial image with $3N_{\mathbf{J}}$ components (i.e. the number of parameters of the transformation $\mathcal{T}_\delta$). Even when limiting δ to smooth deformations by considering only a couple of control points along each dimension, $3N_{\mathbf{J}}$ quickly amounts to hundreds of parameters, rendering the computational cost of this calculation prohibitive.

Alternatively, we can infer the contributions of both factors in (6.9), by integrating over the 3D image index space. By rearranging the summation over $\mathbf{U}$ and the projection operator $\mathcal{A}_k$, we obtain

$$\frac{\partial \mathcal{J}_{\mathrm{m}}(\boldsymbol{p}, f_\delta)}{\partial \boldsymbol{a}} = \frac{1}{N_{\mathbf{K}}} \sum_{k\in\mathbf{K}} \sum_{\boldsymbol{i}\in\mathbf{I}} \xi_{\delta,k}(\boldsymbol{i}) \frac{\partial f_\delta(\boldsymbol{i})}{\partial \boldsymbol{x}} \frac{\partial \mathcal{T}_\delta(\boldsymbol{i})}{\partial \boldsymbol{a}} \,, \quad (6.12)$$

in which

$$\xi_{\delta,k} = \mathcal{A}'_k \frac{\mathcal{J}(p_k, g_{\delta,k})}{\partial g_{\delta,k}} \quad (6.13)$$

and $\mathcal{A}'_k$ corresponds to the backprojection operator. Using this alternative procedure, computing the partial derivatives still requires the $N_{\mathbf{K}}$ projections of f_δ. However, the $3N_{\mathbf{J}}N_{\mathbf{K}}$ projections of the second part of the calculation corresponding to (6.11), are now replaced by backprojecting (6.10) for each of the $N_{\mathbf{K}}$ projection views.

An additional advantage of this calculation procedure comes from the fact that the contributions of each of the projections can be summed more efficiently. $\frac{\partial \mathcal{T}_\delta}{\partial \boldsymbol{a}}$ is 3D tensor image (with $3 \times 3N_{\mathbf{J}}$ tensor size), which cannot be stored on disk. Its pixel values have to be recalculated for each evaluation. By inverting the summations over the projection views and the pixel space in (6.12), each $\frac{\partial \mathcal{T}_\delta(\boldsymbol{i})}{\partial \boldsymbol{a}}$ is calculated only once.

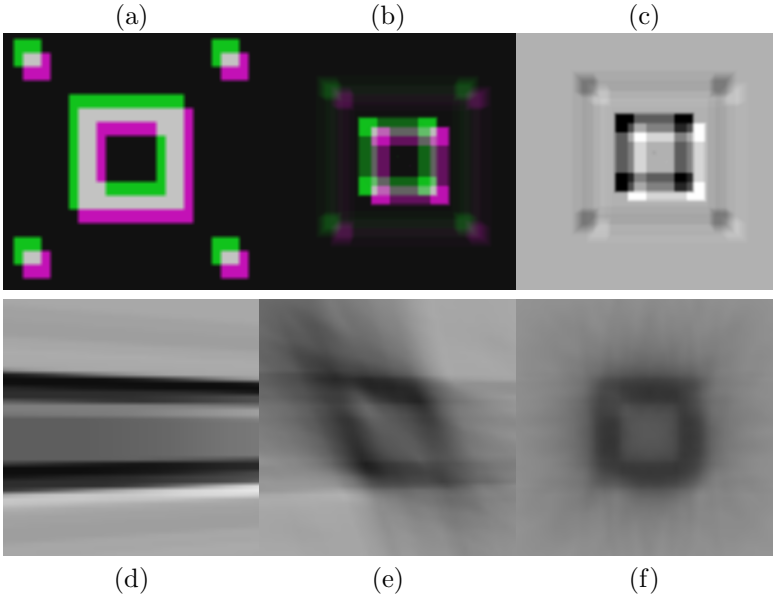

Figure 6.1: Example to illustrate the 2D-3D registration approach using a simple geometry: (*a*) axial slice of colour overlay of two images, misaligned by translation; (*b*) colour overlay of the cone-beam projection views from the lateral right side, (*c*) image corresponding to the partial derivative of the similarity between the projection views, $\partial\mathcal{J}/\partial g_{\delta,k}$ in (6.10); backprojection $\xi_{\delta,k}$ of this image for the same axial slice as in (*a*); the sum of multiple backprojections $1/N_{\mathbf{K}} \sum_{k\in\mathbf{K}} \xi_{\delta,k}$ for $N_{\mathbf{K}} = 5$ (*e*) and 30 (*f*).

The procedure is illustrated with an example using a simple geometry. Consider figure 6.1a in which an axial slice is shown of two images in colour overlay. The green one was obtained by translating the purple one in all three directions. Suppose that one corresponds to f_{r}, while the other is used to generate a projection sequence obtained from rotating views every 12°. Figure 6.1b shows the colour overlay of the projection views from the lateral right side of both images (i.e. $g_{\delta,k}$ and p_k). Figure 6.1c is the image that corresponds to the partial derivative $\partial\mathcal{J}/\partial g_{\delta,k}$ in (6.10), and figure 6.1d the backprojection $\xi_{\delta,k}$ of this image for the same axial slice as figure 6.1a. Similarly, figure 6.1e and f show $1/N_{\mathbf{K}} \sum_{k\in\mathbf{K}} \xi_{\delta,k}$ for $N_{\mathbf{K}} = 5$ and 30, respectively.

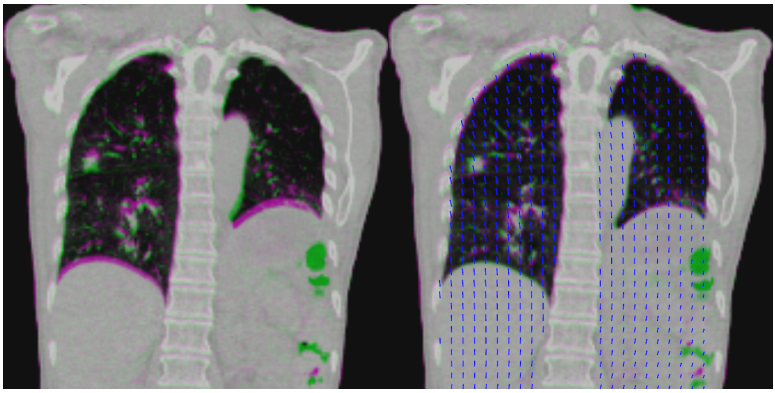

(a) (b)

Figure 6.2: (*a*) Images used for the feasibility study: coronal slice of colour overlay of the exhale frames of two 4D CT acquisitions of the same patient. Interfractional changes are visible such as changes in stomach filling, setup errors and baseline variations. One is used to generate the projection sequence $\boldsymbol{p}$, and the other will serve as reference image f_{r}. (*b*) Coronal slice of the colour overlay between the image used to generate the projection sequence $\boldsymbol{p}$, and the transformed reference image f_{δ} found as a result of the registration method. The resulting deformation field is shown in overlay.

6.3 Feasibility Study

We performed a simple experiment to illustrate the feasibility of the approach. We used the end-exhale frames of repeat 4D CT acquisitions of the same patient. The time between acquisitions was two days. The images are shown in colour overlay in figure 6.2a. Interfractional changes are noticeable between both acquisitions such as changes in stomach filling and gas in the intestine. Also visible are changes in the patient positioning due to small setup errors with respect to the ribs and apex of the lung. The inner thoracic structures seem affected by a comparatively larger misalignment, due to variations in baseline. All of these changes can be expected between planning and treatment, and the simulation setup can therefore be considered realistic from a motion point of view.

The first acquisition was used as the reference image f_{r}. The motion mask was computed for this image, following the method described in chapter 3. From the second acquisition, the projection sequence $\boldsymbol{p}$ was simulated, by calculating ten projection views from evenly spaced angles

ranging from 0° (lateral right) to 90° (anterior). These parameters roughly correspond to selecting the projections corresponding to end-exhale for a quarter of a standard CBCT acquisition. $\mathcal{T}_\delta$ was configured using a large control point spacing, we used $h = 100$ mm. The resulting rectangular control point grid required 540 parameters to cover the motion mask and the borders just outside of $\mathbf{I}_{\text{in}}$.

Execution of the algorithm required about 10 min on an eight-core system. The result of the registration, in the form of the transformed reference image f_δ and the found motion field, are shown in overlay in figure 6.2b. The initial misalignment has been visibly reduced for diaphragm and target. The found motion field is overall very smooth. The magnitude of the displacement ranges from 4 mm near the apex of the lung, to 7.5 mm near the diaphragm

Limited quantitative evaluation was also performed to asses the alignment of the treatment target. We manually identified the position of a vessel near the tumour in both images before registration. The original misalignment in all three directions was -1.1 mm (LR), -2.1 mm (AP) and -6.1 mm (CC). The vessel was reidentified in the transformed image. The residual misalignment was found to be -0.8 mm (LR), -2.6 mm (AP) and -0.6 mm (CC). The largest misalignment was present CC-direction, and was well compensated after registration. The comparatively smaller misalignments in LR and AP directions, were however hardly reduced or were even slightly larger after registration.

6.4 Discussion and Perspectives

The experiment illustrates the feasibility of the approach. Much more experiments are required however to thoroughly assess the performance of the method. In particular, the influence of the number of projections and arc length should be investigated. The use of smaller arcs would considerably extent the utility of the method. Another aspect that requires attention is the influence of the direction of the deformation with respect to the projection angle. Misalignments in the axial plane, were less effectively estimated in comparison to the CC component. Due to the 90° arc length, projections were available that allowed to estimate all components. The projection geometry however allows to estimate CC misalignment from all projections, making the method potentially more sensitive to shifts in this direction.

Baseline variations were represented using a B-spline transform, to

maintain flexibility. The dimensionality in terms of parameters, was reduced by including priors about the physiology of baseline variations. Deformation was assumed to be smooth and not to affect the outer thoracic structures defined by a motion mask. The latter allowed to parametrize the transform using a limited amount of control points. Based on the results of the feasibility study, it seems desirable to further constrain the transformation. In particular, we could demand that deformation near the edges of the motion mask be parallel to the surface of the mask. This would avoid displacement of the thoracic cage, in correspondence with the demand that deformation is zero for the outer thoracic structures. By integrating such a penalty in a small region near the surface of the motion mask, sliding motion would be favoured while other types of deformations are not excluded for the inner structures.

Assuming, the baseline can be estimated with sufficient accuracy using the method described in this chapter, we can extend the patient model proposed in chapter 5. Recall that the patient model was composed of a reference image $\bar{f}$ and a deformation model $\mathcal{T}_{\vartheta,\alpha}$. The deformation model was initially obtained by estimating the phase to phase deformations in a 4D CT acquisition, with respect to the time-weighted mean position. To allow some variability in the model, the deformation component $\mathcal{D}_\vartheta$ was scaled by an amplitude α

$$\mathcal{T}_{\vartheta,\alpha}(\boldsymbol{x}) = \boldsymbol{x} + \alpha\mathcal{D}_\vartheta(\boldsymbol{x})\,. \tag{6.14}$$

Modelled patient images for model parameter values ϑ and α can be obtained by forward warping the reference image with the deformation model (figure 6.3a)

$$s_{\vartheta,\alpha}\big(\mathcal{T}_{\vartheta,\alpha}(\boldsymbol{x})\big) = \bar{f}(\boldsymbol{x}) \tag{6.15}$$

Variations in the mean position might be too large to be accounted for adequately by varying ϑ and α. With baseline monitoring in the treatment room, a third mechanism to compensate for motion variations can be introduced, allowing to locally compensate for baseline variations using the shift δ. Assuming the shift was measured with respect to the mean position image, the full deformation model taking into account the breathing phase, amplitude and potential shifts can be denoted as

$$\mathcal{T}_{\vartheta,\alpha,\delta}(\boldsymbol{x}) = \boldsymbol{x} + \delta(\boldsymbol{x}) + \alpha\mathcal{D}_\vartheta(\boldsymbol{x})\,, \tag{6.16}$$

and patient images at the corresponding modelled state can be obtained in a similar way to (6.15), by forward warping $\bar{f}$ using $\mathcal{T}_{\vartheta,\alpha,\delta}$ (figure 6.3b).

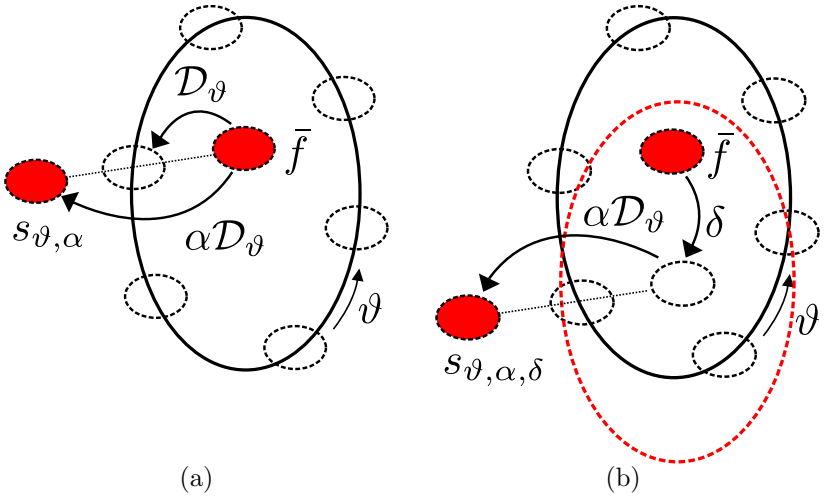

Figure 6.3: Schematic representation of the model parametrization. (*a*) Two-parameter model which is able to describe the intracycle variations that occur between breathing phases, and allows to globally modify the breathing pattern to account for intercycle variability (*b*) Three-parameter model, which in addition allows for a local periodic update to account for intra- and interfractional baseline variations.

6.5 Conclusion

We described a method for estimating a 3D deformation between a set of projections and a reference image. The approach consisted of measuring the correlation between the projections and the projection views of the reference image in 2D projection space. A computation scheme was presented in which the 2D information is integrated over 3D space, allowing to estimate non-rigid transformations requiring many parameters.

The method was applied to the case of estimating baseline variations from a selection of cone-beam projections. The transformation dimensionality was reduced by assuming the deformation was spatially smooth, and only affected the inner thoracic structures defined by a motion mask.

A preliminary feasibility study was performed in which the cone-beam projections were simulated from a second CT acquisition of the same patient. The method showed potential, compensating the majority of the misalignment. Further work is however required to assess the accuracy and utility of the approach.

References

C. Blondel, R. Vaillant, G. Malandain, and N. Ayache. 3D tomographic reconstruction of coronary arteries using a precomputed 4D motion field. *Phys Med Biol*, 49(11):2197–2208, Jun 2004.

W. Duthoy, W. D. Gersem, K. Vergote, T. Boterberg, C. Derie, P. Smeets, C. D. Wagter, and W. D. Neve. Clinical implementation of intensity-modulated arc therapy (IMAT) for rectal cancer. *Int J Radiat Oncol Biol Phys*, 60(3):794–806, Nov 2004.

P. R. Geraghty, S. T. Kee, G. McFarlane, M. K. Razavi, D. Y. Sze, and M. D. Dake. CT-guided transthoracic needle aspiration biopsy of pulmonary nodules: needle size and pneumothorax rate. *Radiology*, 229(2):475–481, Nov 2003.

D. J. Godfrey, F.-F. Yin, M. Oldham, S. Yoo, and C. Willett. Digital tomosynthesis with an on-board kilovoltage imaging device. *Int J Radiat Oncol Biol Phys*, 65(1):8–15, May 2006.

G. D. Hugo, J. Liang, and D. Yan. Marker-free lung tumor trajectory estimation from a cone beam CT sinogram. *Physics in Medicine and Biology*, 55(9):2637, 2010.

D. A. Jaffray, D. G. Drake, M. Moreau, A. A. Martinez, and J. W. Wong. A radiographic and tomographic imaging system integrated into a medical linear accelerator for localization of bone and soft-tissue targets. *Int J Radiat Oncol Biol Phys*, 45(3):773–789, Oct 1999.

D. A. Jaffray, J. H. Siewerdsen, J. W. Wong, and A. A. Martinez. Flat-panel cone-beam computed tomography for image-guided radiation therapy. *Int J Radiat Oncol Biol Phys*, 53(5):1337–1349, Aug 2002.

J. H. Lewis, R. Li, W. T. Watkins, J. D. Lawson, W. P. Segars, L. I. Cervio, W. Y. Song, and S. B. Jiang. Markerless lung tumor tracking and trajectory reconstruction using rotational cone-beam projections: a feasibility study. *Physics in Medicine and Biology*, 55(9):2505, 2010.

T. Li, E. Schreibmann, Y. Yang, and L. Xing. Motion correction for improved target localization with on-board cone-beam computed tomography. *Phys Med Biol*, 51(2):253–267, Jan 2006.

T. Lin, L. C. no, X. Tang, N. Vasconcelos, and S. Jiang. Fluoroscopic tumor tracking for image-guided lung cancer radiotherapy. *Phys Med Biol*, 54(4): 981–992, Jan 2009.

Y. Long, J. A. Fessler, and J. M. Balter. Accuracy estimation for projection-to-volume targeting during rotational therapy: A feasibility study. *Medical Physics*, 37(6):2480–2490, 2010.

A. Macovski. *Medical Imaging Systems*. Prentice Hall Professional Technical Reference, Upper Saddle River, NJ, 1983.

T. E. Marchant, A. M. Amer, and C. J. Moore. Measurement of inter and intra fraction organ motion in radiotherapy using cone beam CT projection images. *Phys Med Biol*, 53(4):1087–1098, Feb 2008.

C. Nelson, G. Starkschall, P. Balter, R. C. Morice, C. W. Stevens, and J. Y. Chang. Assessment of lung tumor motion and setup uncertainties using implanted fiducials. *Int J Radiat Oncol Biol Phys*, 67(3):915–923, Mar 2007.

L. T. Niklason, B. T. Christian, L. E. Niklason, D. B. Kopans, D. E. Castleberry, B. H. Opsahl-Ong, C. E. Landberg, P. J. Slanetz, A. A. Giardino, R. Moore, D. Albagli, M. C. DeJule, P. F. Fitzgerald, D. F. Fobare, B. W. Giambattista, R. F. Kwasnick, J. Liu, S. J. Lubowski, G. E. Possin, J. F. Richotte, C. Y. Wei, and R. F. Wirth. Digital tomosynthesis in breast imaging. *Radiology*, 205(2):399–406, Nov 1997.

J. Nocedal. Updating quasi-newton matrices with limited storage. *Mathematics of computation*, 35(151):773–782, July 1980.

P. R. Poulsen, B. Cho, and P. J. Keall. A method to estimate mean position, motion magnitude, motion correlation, and trajectory of a tumor from cone-beam CT projections for image-guided radiotherapy. *Int J Radiat Oncol Biol Phys*, 72(5):1587–1596, Dec 2008.

P. R. Poulsen, B. Cho, D. Ruan, A. Sawant, and P. J. Keall. Dynamic multileaf collimator tracking of respiratory target motion based on a single kilovoltage imager during arc radiotherapy. *Int J Radiat Oncol Biol Phys*, Feb 2010.

T. G. Purdie, J.-P. Bissonnette, K. Franks, A. Bezjak, D. Payne, F. Sie, M. B. Sharpe, and D. A. Jaffray. Cone-beam computed tomography for on-line image guidance of lung stereotactic radiotherapy: localization, verification, and intrafraction tumor position. *Int J Radiat Oncol Biol Phys*, 68(1):243–252, May 2007.

S. Rit, D. Sarrut, and C. Ginestet. Respiratory signal extraction for 4D CT imaging of the thorax from cone-beam CT projections. *Med Image Comput Comput Assist Interv*, 8(Pt 1):556–563, 2005.

D. Rueckert, L. I. Sonoda, C. Hayes, D. L. Hill, M. O. Leach, and D. J. Hawkes. Nonrigid registration using free-form deformations: application to breast MR images. *IEEE Trans Med Imaging*, 18(8):712–721, Aug 1999.

Y. Seppenwoolde, H. Shirato, K. Kitamura, S. Shimizu, M. van Herk, J. V. Lebesque, and K. Miyasaka. Precise and real-time measurement of 3D tumor motion in lung due to breathing and heartbeat, measured during radiotherapy. *Int J Radiat Oncol Biol Phys*, 53(4):822–834, Jul 2002.

H. Shirato, Y. Seppenwoolde, K. Kitamura, R. Onimura, and S. Shimizu. Intrafractional tumor motion: lung and liver. *Semin Radiat Oncol*, 14(1): 10–18, Jan 2004.

D. Skerl, D. Tomazevic, B. Likar, and F. Pernus. Evaluation of similarity measures for reconstruction-based registration in image-guided radiotherapy and surgery. *Int J Radiat Oncol Biol Phys*, 65(3):943–953, Jul 2006.

J.-J. Sonke, J. Lebesque, and M. van Herk. Variability of four-dimensional computed tomography patient models. *Int J Radiat Oncol Biol Phys*, 70(2): 590–598, Feb 2008.

D. Tomazevic, B. Likar, and F. Pernus. 3-D/2-D registration by integrating 2-D information in 3-D. *IEEE Trans Med Imaging*, 25(1):17–27, Jan 2006.

I. B. Tutar, R. Managuli, V. Shamdasani, P. S. Cho, S. D. Pathak, and Y. Kim. Tomosynthesis-based localization of radioactive seeds in prostate brachytherapy. *Med Phys*, 30(12):3135–3142, Dec 2003.

J. Vandemeulebroucke, J. Kybic, P. Clarysse, and D. Sarrut. Respiratory motion estimation from cone-beam projections using a prior model. *Med Image Comput Comput Assist Interv*, 12(Pt 2):365–372, 2009.

J. W. H. Wolthaus, J. J. Sonke, M. van Herk, and E. M. F. Damen. Reconstruction of a time-averaged midposition CT scan for radiotherapy planning of lung cancer patients using deformable registration. *Med Phys*, 35(9):3998–4011, Sep 2008.

C. X. Yu. Intensity-modulated arc therapy with dynamic multileaf collimation: an alternative to tomotherapy. *Phys Med Biol*, 40(9):1435–1449, Sep 1995.

R. Zeng, J. A. Fessler, and J. M. Balter. Respiratory motion estimation from slowly rotating X-ray projections: theory and simulation. *Med Phys*, 32(4): 984–991, Apr 2005.

R. Zeng, J. A. Fessler, and J. M. Balter. Estimating 3-D respiratory motion from orbiting views by tomographic image registration. *IEEE Trans Med Imaging*, 26(2):153–163, Feb 2007.

L. Zijp, J. Sonke, and M. van Herk. Extraction of the respiratory signal from sequential thorax cone-beam X-ray images. In *14th International Conference on the Use of Computers in Radiation Therapy, Seoul, Korea*, May 2004.

7

Conclusions and Perspectives

Abstract This chapter is dedicated to conclusions with respect to the contributions described in previous chapters. Though the chapters might not easily fit into one class, the work presented can be seen as serving three basic purposes. A first part of the contributions was conceived to facilitate establishing a prior about the patient's breathing pattern from 4D CT, and attention was given to the B-spline representation of the deformation model. In a second instance, we made efforts towards respiratory motion modelling. A registration-based modelling approach was described, in which respiratory motion was decomposed and each aspect was accounted for with adapted spatial and temporal responses. The last part concerned applying the proposed patient model to intrafraction motion estimation from cone-beam projections. We will a give brief overview of each of these parts, and detail some perspectives that were identified in retrospect, or that concern uncompleted work. Finally, a broader look on the topic is presented along with some closing remarks.

Contents

7.1 Deformable Registration of the Lungs

7.1.1 Fast B-spline Interpolation using B-LUTs

In chapter 2, we described a fast alternative to B-spline interpolation based on an approximate calculation using precomputed B-spline weights. During B-spline indirect transformation, these weights are efficiently retrieved in a nearest-neighbour fashion from a look-up table, greatly reducing overall computation time. Free-form deformations using B-LUTs were also implemented, providing a considerable speed-up compared to conventional B-splines and requiring less memory than other proposed software accelerations. In addition, for the case of deformable registration using a free-form deformations, the use based on B-LUTs results in an exact B-spline calculation. The B-LUT source code, compatible with the ITK toolkit, was made freely available.

A LUT for the Spatial Derivatives of B-Splines An interesting extension of the current B-LUT framework would consist in also providing an accelerated calculation of the spatial derivatives of B-splines. This would involve calculating additional LUTs for each of the spatial derivatives. These would be useful during image registration, for interpolating the gradient of the target image, required when using gradient-based optimizers. In addition, some regularization penalties such as bending energy (Wahba, 1990) also require evaluation of the spatial derivatives of the motion field. Extension of the B-LUTs would therefore be useful for the calculation of such penalties as well.

7.1.2 Motion Mask Extraction

In chapter 3, a method for automatically extracting a motion mask from CT images was proposed. The method provided a division between inner and outer thoracic structures, corresponding to moving and less-moving regions in the case of respiratory motion. The interface was explicitly confined between the lungs and the rib cage, and designed to coincide with the pleurae where sliding motion occurs. The suitability of the extracted masks was illustrated by performing subsequent registrations on each of obtained subregions separately, and by including a boundary matching mechanism (Wu et al., 2008). It was found that registration accuracy was improved with respect to registration performed on the original images, and using the same control point spacing. Inversely, using the motion mask should allow to obtain comparable accuracy, using a larger control point

spacing. This results in a faster, more efficient algorithm and improves robustness to noise and artifacts.

The approach of computing a mask to preserve sliding is a pragmatic one, but it has been proven effective. The proposed method is practical and particular attention was given to its robustness, with the aim of limiting user interaction and allowing an insertion into clinical practice. Nonetheless, the described procedure might still give unsatisfactory results in particular cases and require manual adaptation. Two potential improvements were identified, which could further increase the robustness of the method. The first concerns the extraction method itself, while the second is related to the way the motion mask is incorporated into the registration framework.

Spatio-Temporal Mask Extraction The proposed method comprises of two parts. The first one consists of extracting anatomical features to produce the velocity maps, while in the second part the mask is defined using level sets. The level set processing was found to be stable and reproducible. Mainly because it is applied to binary velocity maps and the progressing contours are monitored closely. However, erroneous extraction of the velocity maps will surely compromise the motion mask extraction. The described segmentation of the rib cage was found to be a difficult processing step, due to locally reduced density of the ribs for some patients. An accurate retrieval of the shape of these structures is not critical, since the bony anatomy is mainly used as a stopping structure, to constrain the growing level set from propagating outside the thoracic cage. It is desirable however, that a complete skeleton of the rib cage is obtained; that is, that partly missing segments are avoided as much as possible.

Faulty rib segmentation may influence the obtained shape of the mask, but not necessarily the obtained accuracy of the registration. In areas where the found interface does not exactly coincide with the pleurae, but no strong sliding occurs (as is the case at the anterior interface, near the sternum), registration accuracies should not be compromised as long as the motion mask extraction was consistent with respect to the anatomy for the considered image pair. To improve the stability and the consistency of rib segmentation, the extraction procedure described can be extended to the 4D image domain (using the 4D image obtained from composing the image pair, or based on the entire 4D CT data set). This approach increases the connectivity of the voxels by adding the corresponding voxels of temporally neighbouring images, and was found to give more reproducible results for the respective rib segmentations.

Taking into account the Motion Mask The easiest way of introducing the motion masks in the B-spline registration algorithm, is to only consider one of the subregions in the reference mask when calculating the registration criterion (Rietzel et al., 2005). It was found this approach occasionally led to misalignment of the edges of the masked structures, and we therefore introduced a mechanism for penalizing the misalignment of the boundary (Wu et al., 2008). The images were both modified using the respective motion masks and a slightly larger region was used to compute the similarity. As a consequence, masks were required on both the reference and target image, and motion mask extraction was required to be reproducible with respect to patient anatomy. Especially in the case of registration across 4D CT, this constitutes a considerable increase in workload and raises the requirements for the extraction method.

Schmidt-Richberg et al. (2009a) proposed a method for incorporating a segmentation into a non-parametric registration framework using a diffusive regularization scheme. The method only relies on a segmentation defined on the reference image, with respect to which the regularization of the motion field is locally modified. Regularization for the perpendicular component with respect to mask interface is maintained, avoiding gaps in the motion field. The regularization for the tangential field is relaxed, allowing discontinuities in the motion field and preserving sliding motion. This elegant approach requires only one mask, and allows to process the whole region simultaneously. A possible extension to the parametric B-spline registration could consist in lowering the B-spline control point spacing, and locally introducing explicit anisotropic regularization (Chun et al., 2009) in the objective function. Unfortunately, this would compromise the efficiency of the algorithm.

7.1.3 Spatio-Temporal Registration

In chapter 4 we investigated the feasibility of a spatio-temporal registration scheme for respiratory-correlated images of the thorax. We aimed at improving the robustness of deformable registration by using a global formulation of the 4D motion estimation problem and by pursuing an accurate, but low-dimensional and problem-specific deformation model. A spatial transformation was extended to the temporal domain by explicitly modelling the temporal variations of the deformation throughout the breathing cycle. The spatio-temporal modelling resulted in piecewise smooth temporal models based on cubic splines and allowed considerable reduction of the numbers of registration parameters with respect to

sequential spatial registration, while maintaining the registration accuracy within 0.1 mm. The approach showed an improved robustness in the presence of artifacts.

The methodological contributions we made to registration of the lung images described in chapter 3 and 4 both focussed on the parametrization of the transformation. A more efficient, compact parametrization was pursued requiring less parameters, while maintaining comparable accuracy. The principal assumption was that robustness to noise and artifacts could be improved, by augmenting the inherent smoothness of the motion field. Ironically, we found that a more efficient reduction of parameters could be found, by locally relaxing the smoothness constraints where needed. Using a motion mask allowed for a local discontinuity in the motion field, permitting to impose stronger spatial smoothness elsewhere. Similarly, we found that the spatio-temporal registration benefited from a piecewise smooth trajectory model to account for the sudden change in velocity at end-inhale.

Regularization Schemes The B-spline transformation model imposes smoothness upon the sought geometric transformation it encodes. Indeed, the continuity properties of the B-spline basis functions are adopted in the motion field. However, these parametric restrictions sometimes provide insufficient control over the properties of the transformation. Each B-spline control point is adjusted independently of all others based on local image information. In regions where salient registration features are lacking or ambiguous, this approach might provide insufficient regularization and can lead to physically or physiologically improbable solutions. In addition to providing a measure of similarity, the objective function should therefore be complemented with an explicit regularization term. The latter should penalize undesirable properties of the deformation field, therefore favouring physically plausible solutions.

Regularization in the form of explicit penalties in the objective function was not included in this work. The B-spline deformable transformation grid was limited to the control point spacing of 32 mm which was empirically found to be sufficiently large to result in a smooth deformation field for the lung region. It is however fully recognized, that including explicit regularization is required for extending the use of the developed registration framework. In addition, it constitutes an essential mechanism for improving the robustness to artifacts and noise.

Explicit regularization is expected to be complementary to the contributions concerning the parametric B-spline representations of the

transformations described in this work. In fact, the latter should allow for a customization of the regularization schemes. The use of the motion mask allows for stronger regularization terms to be imposed, since sliding is preserved explicitly. In addition, specific schemes can be selected for each of the subregions separately. For instance, it would seem sensible to assume that the outer thoracic structures (not containing any lung tissue), would deform incompressibly (Rohlfing et al., 2003), while for the inner structures (made out of lungs, mediastinum and abdomen) a more permissive bending energy could be more appropriate. Similarly, the spatio-temporal framework allows for the inclusion of specific penalties, which could provide additional temporal smoothing.

Robustness to Artifacts The benefit of the spatio-temporal approach was illustrated by means of a simulated experiment, in which a single artifact was inserted in a 4D CT sequence (in chapter 4, section 4.4.3). More elaborate experiments are required to quantitatively assess the potential of the registration approach, involving realistic data and a larger variety of artifacts. An obvious aspect that should be looked into is the influence of the temporal duration of the artifact. The additional temporal smoothing constitutes a clear advantage when confronted to an artifact in a single frame. This advantage might quickly disappear, as the artifacts affect several frames of the 4D CT, as is usually the case.

The influence of the temporal location of artifacts also deserves some attention. Near end-inhale, the deformation model is characterized by a local increase in degrees of freedom compared to other frames. This could render end-inhale more prone to perturbations in the intensity space near that frame. The proposed registration framework consisted of a single reference frame (end-exhale in this work) which was compared to all other frames. An artifact in the reference might have larger impact than elsewhere. Alternative schemes can be imagined, using multiple references (Boldea et al., 2008), which result in smaller deformations to be estimated and remove the bias caused by the choice of the reference. Alternatively, an iterative approach can be devised in which the result of an initial registration is used to construct a new image combining the intensities of all frames (e.g. a mid-position image (Wolthaus et al., 2008b)). In the next step, this new image could serve as a reference to estimate the deformations to all frames of the 4D CT (and so on), effectively reducing the influence of the initial reference image.

Validation of Deformable Registration Validation is a complicated but essential step to facilitate the translation of deformable registration research into clinical applications for image-guided therapy (Sarrut, 2006). Currently there is no standard methodology for validation of deformable registration. Synthetic images and phantoms can provide high precision and easy validation, useful for qualitative evaluation of registration performance (Kashani et al., 2008). However, they generally lack realism to provide credible validation for use in a clinical setting. The preferred method remains to derive the reference standard from the actual patient image data, by establishing expert landmark correspondences (Brock et al., 2005; Sarrut et al., 2006; Rietzel and Chen, 2006; Sarrut et al., 2007; Vandemeulebroucke et al., 2007; Wolthaus et al., 2008b; Wu et al., 2008; Boldea et al., 2008; Al-Mayah et al., 2008; Werner et al., 2009a; Schmidt-Richberg et al., 2009a; Yin et al., 2009; Castillo et al., 2010; Brock and Consortium, 2010).

There are however several drawbacks to this method. The accuracy of the established reference is limited, and influenced by the image quality. The task of establishing the reference is time consuming. In addition, the obtained landmarks are located near clearly identifiable image features where they locally establish a sufficient condition for the motion field to satisfy. The condition is however merely necessary for the entire field, and several authors have warned that the size and distribution of the set of landmarks might influence the estimated registration accuracy (Kabus et al., 2009; Castillo et al., 2009; Zhong et al., 2010). Several groups have proposed semi-automatic methods to establish the reference standard from image data (Murphy et al., 2008; Castillo et al., 2009), in order to deal with some of the mentioned drawbacks, and standardize the process of establishing a reference.

The drawbacks mentioned also stress the importance of sharing large, well-established references with the community, in order to save time and allow algorithms to be tested on the same data. We participated in the process by making publicly available a 4D CT data set, registration results and the validation data in the form of over 400 manually identified landmarks throughout the 4D sequence (Vandemeulebroucke et al., 2007). The initiative received good response and references to it were found in several studies (Ayadi et al., 2007; Wolthaus et al., 2008b; Noe et al., 2008; Rit et al., 2009; Vaman et al., 2009; Kabus et al., 2009; Su et al., 2009a; Schmidt-Richberg et al., 2009b; Su et al., 2009b; Ruppertshofen et al., 2009, 2010). We intend to extend the current available data, with the images and the 3000 landmarks described in chapter 4. We should also

mention the initiative of Castillo et al. (2009), to put at the disposal large sets of landmark correspondences between the inhale and exhale frames of 4D CT images.

Even when disposing of large set of landmarks, analysis of the registration performance is not straightforward. We found in chapter 4, that analysis should be performed locally as the global measures do not allow to distinguish between closely related registration results. Even then, we found that motion fields leading to similar TRE values, can still have quite different properties, which confirms the observations of (Kabus et al., 2009). The previous emphasizes the need for additional measures for evaluating deformable registration. In fact, it is our opinion that for the specific case of 4D CT of the lungs, landmark-based validation is no longer suitable to efficiently discriminate between most current registration algorithms. It is our believe that priority should be given to devising measures that can quantify clinically relevant characteristics of the motion field. Research on registration of 4D CT should focus on making methods more robust and plausible from a physiological point of view, rather than developing novel algorithms that can reduce the target registration error with another 0.1 mm.

Alternative (necessary) conditions can be found which the motion fields should satisfy, and by increasing the number of these measures we might be able to improve the evaluation of deformable registration. In addition to measures derived from image information (such as landmarks, contours, similarity measures and so on), evaluation should take into account the properties of the motion field itself, by verifying aspects such as the consistency and invertibility of the motion field. Related to this is the work of Zhong et al. (2007), who proposed using computational modelling and finite element methods, to identify regions in which deformable registration is mis-performing. The described method is fully automatic, and can be seen as a complementary evaluation as it can provide a measure of quality of the motion field, in regions where salient image is missing (Zhong et al., 2007, 2010). In the case of CT of the lungs, an additional measure becomes available by assessing the lung function. The change in lung volume as measured by segmentation of the lungs, can be compared to the ventilation predicted by the deformation field (Guerrero et al., 2006; Kabus, 2008; Yamamoto et al., 2009), providing another necessary condition for the registration results to satisfy.

7.2 Respiratory Motion Modelling

In chapter 5 we proposed a patient-specific model which consisted of a reference image and a deformation model. The reference image served as a density map of the patient anatomy, and allowed to generate patient images at modelled breathing states by warping it using the deformation model, for certain values of the model parameters. The deformation model was initially obtained from a 4D CT acquisition. Deformable registration was performed to provide a dense motion estimate that described the complex deformations that occur during a breathing cycle. From then on, abstraction was made of that complexity, and one model parameter was required to characterize an arbitrary breathing *phase*. In chapters 5 and 6 we provided motion estimates in the treatment room by fitting the model to cone-beam projections. Additional model parameters were introduced to account for intercycle and intra- and interfraction variability. These aspects of lung motion were represented with a scalar *amplitude* and a low-dimensional vector field *baseline*, to account for potential shifts of the inner thoracic structures.

B-splines were used to represent the motion model, providing a continuous representation over space and time. They were also found convenient for their flexibility, as they allowed to represent different levels of complexity using the same framework, and enabled straightforward extension to the temporal domain. Evolution of the model parameters over time was also represented using splines, providing temporal regularization and parameter reduction during motion estimation.

7.2.1 Reference Image

Following the initial procedure described in chapter 5, the model reference image was obtained by transforming one frame of the 4D CT to the time-weighted mean position. The deformation field used for the transformation, was obtained by averaging several deformation fields, which should reduce the influence of local irregularities. However, a single frame provides the intensity map of the reference image, rendering the model sensitive to artifacts in that frame. We previously mentioned alternative procedures for computing a reference image, which exploit all the frames of the 4D CT. These procedures were initially not adopted, as it was found they resulted in reduced spatial resolution (Wolthaus et al., 2008b).

The advantages of obtaining an improved image quality deserve to

be investigated further, as this line of research is considered highly promising for future use of 4D CT and respiratory-correlated imaging in general. Indeed, many clinical applications in essence require a high quality representation of the patient anatomy, and an estimate of the motion with respect to that representation. High image quality for all frames of the sequence is often not explicitly required. Developing registration algorithms capable of providing accurate motion estimates on low-quality images, would allow to lower the dose of 4D CT acquisitions. This in turn, would enable a more extensive use of 4D CT and even allow other pathologies to benefit from the modality, currently almost exclusively used in radiation therapy.

Several authors have proposed to obtain the high quality reference directly from the 4D CT, by compensating the motion using the deformable registration results and processing the corresponding intensities. Li et al. (2005) extended a penalized weighted least squares smoothing method (Fessler, 1994) to 4D, to account for potential registration errors. Wolthaus et al. (2008b) found that arithmetic averaging or median averaging of the corresponding intensities reduced noise and artifacts and rendered the filtered image more representative in terms of tumour shape than any other frame of the 4D CT. Alternatively, a high quality reference can be obtained by establishing the spatial correspondence with a breath-hold CT (McClelland et al., 2006), or even a contrast enhanced breath-hold CT (Nijkamp et al., 2010).

7.2.2 Deformation Model

Intracycle Variation A prior model of the intracycle variation was obtained from 4D CT. In chapter 5, we used the demons algorithm for performing deformable registration. While the concept remains identical, alternative ways of computing the deformation model were explored in chapter 4. The main goal of this approach is to reduce the influence of artifacts in the 4D CT acquisition on the motion model. Indeed, these irregularities occur randomly across the image acquisition. If not accounted for, they will result in a systematic deviation of the model from the reality, making the model less representative of the patient's breathing.

From this perspective, we pursued the same goal as the methods described in (McClelland et al., 2006; Zhang et al., 2007); that is, to capture the underlying breathing pattern while filtering out the random variations. In (Zhang et al., 2007), this is done on a single 4D CT acquisition by performing principal component analysis. The method

described by McClelland et al. (2006) goes even further. Several breathing cycles are sampled, providing limited statistics to compute an average respiratory cycle, expected to be most representative for the patient's breathing than just any (filtered) cycle. No statistics whatsoever were applied to the represented cycle in the 4D CT acquisition, increasing the uncertainty that the model provides a good patient representation. Alternatively, we explored mechanisms to adapt and update the model using intrafraction patient data.

Intercycle Variation In the proposed motion model, intercycle variability was represented by a linear inter- or extrapolation of the deformations with respect to the mean position. The amplitude parameter α, controlling the scaling of the linear model, was not a function of $\boldsymbol{x}$. It was defined as a constant for the entire thorax, for which the most suitable value should be selected, for instance based on the global similarity with cone-beam projection as in chapter 5. The reason for this simple linear model, is closely related to the limitations of the motion data used to construct the model. 4D CT does not sample any intercycle variability and does not justify proposing more complicated relationships.

Deformations were expressed and scaled with respect to the time-weighted mean position. The end-exhale position, would also have been a reasonable choice. By using the mean position, it was possible to represent variability in all directions and breathing phases. Even for the end-exhale position, which has been reported to be more reproducible than at inhale, but prone to variation nonetheless (Seppenwoolde et al., 2002; Sonke et al., 2008; Rit et al., 2010). In addition, motion estimation with respect to the mean position will produce smaller deformations. Scaling these deformations will tend to be more conservative, with respect to scaling the full exhale-inhale deformation. Motion estimation with respect to the mean position, is less likely to produce a bias (for instance, in case of a systematic underestimation of the deformation as observed in chapter 3). If motion is compensated correctly, what is obtained is the clinically relevant time-weighted mean position (Wolthaus et al., 2008a).

In (Vandemeulebroucke et al., 2008) we found that allowing for intercycle variation through the amplitude parameter of the model, rendered the motion estimation from cone-beam projections as described in chapter 5 more stable, as otherwise all variations are attributed to the breathing phase. In addition, the experiments performed on repeat 4D CT acquisitions in chapter 5, confirmed that this parametrization allows to compensate for some of the breathing variation. For some applications,

the structures of interest might only concern the tumour. In this case, describing the tumour motion based on its baseline (3 parameters fixed at the beginning of the session), a phase and amplitude (2 parameters at each instant, continuously evolving over time) constitutes a flexible model in terms of degrees of freedom. For other applications, the model might lack realism and flexibility, and more advanced methods have been proposed that provide spatially varying intercycle variability by fitting local model parameters to observed breathing states (McClelland, 2008; Yang et al., 2008).

Nonetheless, there are several arguments in favour of our approach. The first and most important one is the simplicity of the resulting model. The representation allows limited intercycle variability to be estimated under challenging circumstances, e.g. from a cone-beam projection sequence as in chapter 5. It should also be noted, that it remains to be assessed how much additional motion compensation can be obtained, for instance from locally establishing an intercycle relationship based on 15-25 s of motion data, when confronted with interfractional changes in breathing motion. A non-negligible advantage is that the model results from only exploiting acquisitions already acquired for treatment delivery and planning. By respecting these limitations, it would be feasible to insert the procedures requiring the motion model into clinical practice.

Intercycle variability is the aspect of respiratory motion that has arguably received the most attention in literature. Further research on intercycle variation is needed, and could provide insight on the physiology of respiratory motion. However, when considering potential clinical applications of motion modelling, intercycle variation often constitutes the aspect of lung motion that is not likely to have most impact. For motion compensated cone-beam reconstruction, compensation using a phase-based model has been shown to provide considerable improvement of the image quality (Rit et al., 2009), indicating that accounting for the phase to phase deformations compensated most of the motion. For treatment delivery during free breathing, baseline variations have been reported to have the greatest impact on target coverage if not corrected for (Sonke et al., 2008). The tumour motion will influence the required safety margins, but the variations of this motion only has a marginal influence on the definition of these margins (Rit et al., 2010).

Baseline Variations In chapter 6 we described our initial attempts to estimate or monitor baseline variations, from cone-beam projections. Baseline variations were represented using a smooth motion field and

assumed to only affect the inner thoracic structures, corresponding to the inner structures of the motion mask. Using the mask allowed to consider a relatively low number of parameters for the spatial transformation based on B-splines.

More data is required to characterize the spatial representation of baseline variations. Additional insight in this phenomenon might result in lower dimensional transformations for the representation, potentially of a different type. Also, the way to take into account baseline variations in the motion model, requires further attention. The most straightforward procedure is to simply add the shift to the current deformation. This implies the assumption that, although structures have moved inside the thorax, they are still characterized with the same breathing pattern; that is, they still move with the same trajectory as before, which should be verified.

7.2.3 The Benefit of Biomechanical Approaches

Biomechanical approaches have been successfully applied to the field of lung motion estimation. Usually only the initial and final outer lung geometry is extracted from the images and introduced as boundary conditions for solving a contact surface problem using finite element methods (Villard et al., 2005; Al-Mayah et al., 2008; Werner et al., 2009a). When applied to high quality images, intensity-based registration remains superior in terms of accuracy (Werner et al., 2009b). This is understandable considering that the latter considers all inner-organ image information about fissures, bronchi and vessel tree, enabling a better matching of these structures. The potential of biomechanical methods becomes clear, when considering how little information is required to obtain acceptable results. In challenging conditions, in which motion estimates should be provided based on sparse image information (such as 2D-3D motion estimation), biomechanical models may very well have the advantage as they fully exploit the physical prior knowledge of the problem.

It is our believe that deformable registration modelling, could benefit from further inspiration of the biomechanical modelling approaches. An example is given by the motion mask described in chapter 3, which facilitated registration by explicitly accounting for the physiology of respiratory motion. From this point of view, it could be viewed as the deformable registration analogue of the contact surface formulation utilized in biomechanical models. Other authors have also reported that

improvement in registration accuracy can be obtained by introducing similar biophysically inspired mechanisms (Werner et al., 2009b; Schmidt-Richberg et al., 2009a).

Further augmenting biophysical priors could consist in further differentiating the processing of the thoracic structures, and employing different regularization schemes to reflect the physical and mechanical properties of the tissue. As a consequence of the motion mask construction, approximate segmentations of the lungs and bony structures bones are available. During motion estimation, the bony structures could be constrained to rigid deformations (Loeckx et al., 2004; Ruan et al., 2006; Staring et al., 2007). For the remaining structures of the outer region, a volume preserving deformation can be favoured (Tanner et al., 2002; Rohlfing et al., 2003). For the extremely elastic lung tissue, a diffeomorphism (Vercauteren et al., 2007; Chun and Fessler, 2009) is probably the only assumption that should be made about the deformation, while a slightly more restrictive bending energy (Wahba, 1990) might be more suitable for the remaining inner thoracic structures.

Inversely, biomechanical modelling might benefit from rendering their models more patient-specific, as is commonly the case in registration-based modelling. Several authors reported deviation of the respiratory motion due to large sized lung tumours (Plathow et al., 2004; Ehrhardt et al., 2009; Werner et al., 2009a). For these cases, modelling of the lung parenchyma as a homogeneous linear-elastic medium no longer corresponds to reality. The influence of tumour (position and size) should therefore either be included in the modelling, or learned from the available patient data.

7.3 Intrafraction motion estimation

In chapter 5, we presented a method for respiratory motion estimation from a cone-beam projection sequence. A strong prior about the patient's breathing pattern was introduced in the form of a motion model built from a previously acquired 4D CT image. Motion estimation proved to be a challenging task, and a semi-global optimization approach was implemented to achieve stable estimates. Initially, end-exhale and end-inhale was detected using a feature-based method tracking the cranio-caudal displacement of the diaphragm. For each cycle, a smooth temporal parameter model was fitted to describe the evolution of the considered model parameters. Motion continuity was guaranteed by imposing suitable boundary conditions at the endpoints. Considerable motion compensation

was obtained, even when confronted with interfractional variations in breathing motion. Baseline variations were not present in the experiment data, and should be considered separately.

In chapter 6, we described our initial attempts to estimate and potentially monitor baseline variations from cone-beam projections. The method consisted of estimating the 3D deformation, that was present between a 3D reference image and a 2D projection sequence. The dimensionality of the sought spatial transformation was limited, by introducing physiological priors. Similarity was measured in 2D projection space, and an efficient calculation was found by integrating the contribution of the different projection views in the 3D image space. Initial results were promising, illustrating the feasibility of the method. More research is required to assess the advantage of the proposed method over other image guided approaches. In particular, the potential of the method will be determined by the amount of projection data and the projection arc length required to obtain acceptable motion estimations.

7.3.1 Relation to Previous Work

When using the findings described in chapter 5 to construct the prior model used in chapter 6, a modification of the optimization procedure could be made to improve the compatibility between both contributions. In the semi-global optimization strategy individual cycles were considered between consecutive end-exhale breathing stages. This choice was arbitrary, and there is no reason cycles could not be identified by extracting the end-inhale positions. The advantage of the latter is that, the method will then result in a piecewise smooth motion estimation between two end-inhale phases, which better reflects the observations made on 4D CT.

In both chapter 5 and 6, intrafraction motion estimation from cone-beam projections was illustrated by performing motion estimation for the entire field of view of the cone-beam projection, with the aim of providing a motion estimate for a large part of the thorax. Selecting a smaller region of interest could make the method more flexible and certainly more efficient. An obvious choice, is to limit the motion estimation to the immediate neighbourhood of the tumour. The result is a 2D-3D tracking method, based on a prior model very similar to the methods described in (Hugo et al., 2010; Lewis et al., 2010).

7.3.2 Clinical Applications

By combining chapters 6 and 5, we hope to achieve motion estimation from cone-beam projections, robust to interfractional motion variability. The motion estimated from a cone-beam acquisition could serve for motion compensated reconstruction (Li et al., 2007; Rit et al., 2009). Note that in this case all motion with respect to the reference image is estimated, instead of only the periodic component. Correct estimation of baseline, phase and amplitude variations should therefore make the motion-compensated cone-beam reconstruction fully align with the reference. This feature could be very convenient for clinical verification of the motion compensation. The reconstruction must then be modified to correspond to the treatment strategy. For instance, if the treatment was planned at the time-weighted mean position (Wolthaus et al., 2008a), the reconstruction should be deformed using time-weighted average of the motion estimation.

An alternative use of the motion estimate can be gated treatment delivery. If a gating surrogate was simultaneously recorded during cone-beam acquisition, the motion data could serve as training data to establish to relation with variation in tumour position and surrogate. This procedure would avoid the acquisition of fluoroscopic sequences specifically for this purpose and take advantage of the 2-4 min of motion data obtained from the cone-beam acquisition.

7.3.3 2D-3D Similarity Measures

In the studies performed in chapters 5 and 6, experiments were performed on simulated projection data, obtained from repeat 4D CT acquisitions. The simulations can therefore be considered realistic from a breathing motion point of view. The physics of X-ray imaging process was however not modelled in detail and modifications of the described procedures might be required when applying the methods on real cone-beam projections. Our main concern is the influence of noise and scatter which are expected to be present when acquiring real cone-beam projections. Additionally, projection views might contain the treatment table (see figure 5.2a and b) or interventional instruments, not accounted for in the prior patient model, and known to have an effect on the performance (Penney et al., 1998).

Several authors reported pattern intensity to be a good alternative under these circumstances (Weese et al., 1997; Penney et al., 1998; Loeckx et al., 2003; Kim et al., 2007). Others observed good performance for the currently used normalized correlation coefficient (Wu et al., 2009),

even though combination with other measures might improve robustness and accuracy (Kim et al., 2007). Alternatively, preprocessing of the projections, such as unsharp masking (Sorenson et al., 1981) followed by histogram equalization, have been shown to drastically improve the performance of a wide range of similarity measures (Dekker et al., 2003) for 2D-3D registration.

7.4 Looking Ahead

Methods developed in registration and lung motion modelling have recently been applied to assess lung function. Several have shown that by estimating the local deformation, an estimate of the local lung ventilation can be provided to the physician. This could be useful for assessing the influence of radiation on the lung tissue, by comparing ventilation before and after radiotherapy. Locally evaluating lung function would however be useful outside radiation therapy as well, and this line of research is considered highly interesting for the potential clinical applications, as well as for rendering the motion fields obtained from deformable registration physiologically consistent.

Intercycle variability is expected to receive increased attention in the future, mainly for two reasons. Dynamic MRI image quality is bound to improve. In addition, MRI data might become more available in radiotherapy (for instance if linear accelerators integrated in MRI scanners (Lagendijk et al., 2008) were to become commercially available). The absence of an imaging dose to the patient, would allow increased and longer acquisition times, allowing more elaborate approaches for modelling this type of variation.

Particle therapy is rapidly emerging as an alternative treatment modality, due to increased conformality of the treatment dose and better biological response. In brief, the depth of the deposited dose along the particle beam direction, depends on the material encountered along its path. Geometric uncertainties, including those introduced by breathing motion, are therefore expected to have an increased dosimetric impact in comparison to photon beams. Respiratory-synchronized treatment methods might become standard for this treatment modality and motion models will have to provide the required predictions of tumour and organ motion to ensure target coverage.

One of the key advancements in radiotherapy of the last decade concerned the development and availability of 3D in-room imaging,

allowing to guide the treatment based on soft-tissue imaging. It is expected that this type of image guidance will further develop. In particular, the repeated use of imaging over the course of a treatment fraction for monitoring of the patient state seems an interesting feature for future treatment delivery machines. To reduce the imaging dose to patient, creative use of previously acquired planning images and efficient motion estimation algorithms requiring little image information will become increasingly important.

References

A. Al-Mayah, J. Moseley, and K. K. Brock. Contact surface and material nonlinearity modeling of human lungs. *Phys Med Biol*, 53(1):305–317, Jan 2008.

M. Ayadi, J. Vandemeulebroucke, S. Hlavacek, V. Boldea, C. Ginestet, and D. Sarrut. Dosimetry on moving organs: static and dynamic dose distributions computed from 4DCT for lung cancer treatment. In *9th Biennial ESTRO Meeting on Physics and Radiation Technology For Clinical Radiotherapy*, volume 84, page S77, 2007.

V. Boldea, G. Sharp, S. B. Jiang, and D. Sarrut. 4D-CT lung motion estimation with deformable registration: Quantification of motion nonlinearity and hysteresis. *Med Phys*, 35, Issue 3:1008–1018, 2008.

K. K. Brock and D. R. A. Consortium. Results of a multi-institution deformable registration accuracy study (midras). *Int J Radiat Oncol Biol Phys*, 76(2): 583–596, Feb 2010.

K. K. Brock, M. B. Sharpe, L. A. Dawson, S. M. Kim, and D. A. Jaffray. Accuracy of finite element model-based multi-organ deformable image registration. *Med Phys*, 32(6):1647–1659, Jun 2005.

E. Castillo, R. Castillo, J. Martinez, M. Shenoy, and T. Guerrero. Four-dimensional deformable image registration using trajectory modeling. *Phys Med Biol*, 55(1):305–327, 2010.

R. Castillo, E. Castillo, R. Guerra, V. E. Johnson, T. McPhail, A. K. Garg, and T. Guerrero. A framework for evaluation of deformable image registration spatial accuracy using large landmark point sets. *Phys Med Biol*, 54(7):1849–1870, Apr 2009.

S. Y. Chun and J. Fessler. A simple regularizer for b-spline nonrigid image registration that encourages local invertibility. *Selected Topics in Signal Processing, IEEE Journal of*, 3:159–169, 2009.

S. Y. Chun, J. A. Fessler, and M. L. Kessler. A simple penalty that encourages local invertibility and considers sliding effects for respiratory motion. In *Proc. SPIE 7259, Medical Imaging 2009: Image Proc., p. 72592U*, 2009.

N. Dekker, L. S. Ploeger, and M. van Herk. Evaluation of cost functions for gray value matching of two-dimensional images in radiotherapy. *Med Phys*, 30(5): 778–784, May 2003.

J. Ehrhardt, A. S. Réne Werner, and H. Handels. Prediction of respiratory motion using a statistical 4D mean motion model. In , *Second International Workshop on Pulmonary Image Analysis*, London, 2009.

J. A. Fessler. Penalized weighted least-squares image reconstruction for positron emission tomography. *IEEE Trans Med Imaging*, 13(2):290–300, 1994.

T. Guerrero, K. Sanders, E. Castillo, Y. Zhang, L. Bidaut, T. Pan, and R. Komaki. Dynamic ventilation imaging from four-dimensional computed tomography. *Phys Med Biol*, 51(4):777–791, Feb 2006.

G. D. Hugo, J. Liang, and D. Yan. Marker-free lung tumor trajectory estimation from a cone beam CT sinogram. *Physics in Medicine and Biology*, 55(9):2637, 2010.

S. Kabus. Lung ventilation estimation based on 4D CT imaging. In , *First International Workshop on Pulmonary Image Analysis*, pages 73–91, New York, September 2008. Lulu.com.

S. Kabus, T. Klinder, K. Murphy, B. van Ginneken, C. Lorenz, and J. P. W. Pluim. Evaluation of 4D-CT lung registration. In *Medical Image Computing and Computer-Assisted Intervention MICCAI 2009*, pages 747–754, 2009.

R. Kashani, M. Hub, J. M. Balter, M. L. Kessler, L. Dong, L. Zhang, L. Xing, Y. Xie, D. Hawkes, J. A. Schnabel, J. McClelland, S. Joshi, Q. Chen, and W. Lu. Objective assessment of deformable image registration in radiotherapy: a multi-institution study. *Med Phys*, 35(12):5944–5953, Dec 2008.

J. Kim, S. Li, D. Pradhan, R. Hammoud, Q. Chen, F.-F. Yin, Y. Zhao, J. H. Kim, and B. Movsas. Comparison of similarity measures for rigid-body ct/dual x-ray image registrations. *Technol Cancer Res Treat*, 6(4):337–346, Aug 2007.

J. J. W. Lagendijk, B. W. Raaymakers, A. J. E. Raaijmakers, J. Overweg, K. J. Brown, E. M. Kerkhof, R. W. van der Put, B. Hrdemark, M. van Vulpen, and U. A. van der Heide. Mri/linac integration. *Radiother Oncol*, 86(1):25–29, Jan 2008.

J. H. Lewis, R. Li, W. T. Watkins, J. D. Lawson, W. P. Segars, L. I. Cervio, W. Y. Song, and S. B. Jiang. Markerless lung tumor tracking and trajectory reconstruction using rotational cone-beam projections: a feasibility study. *Physics in Medicine and Biology*, 55(9):2505, 2010.

T. Li, E. Schreibmann, B. Thorndyke, G. Tillman, A. Boyer, A. Koong, K. Goodman, and L. Xing. Radiation dose reduction in four-dimensional computed tomography. *Med Phys*, 32(12):3650–3660, Dec 2005.

T. Li, A. Koong, and L. Xing. Enhanced 4D cone-beam CT with inter-phase motion model. *Med Phys*, 34(9):3688–3695, Sep 2007.

D. Loeckx, F. Maes, D. Vandermeulen, and P. Suetens. Temporal subtraction of thorax cr images using a statistical deformation model. *IEEE Trans Med Imaging*, 22(11):1490–1504, Nov 2003.

D. Loeckx, F. Maes, D. Vandermeulen, and P. Suetens. Nonrigid image registration using free-form deformations with a local rigidity constraint. In *MICCAI (1)*, pages 639–646, 2004.

J. McClelland. *Registration Based Respiratory Motion Models for use in Lung Radiotherapy*. PhD thesis, Centre for Medical Image Computing, University College London, 2008.

J. R. McClelland, J. M. Blackall, S. Tarte, A. C. Chandler, S. Hughes, S. Ahmad, D. B. Landau, and D. J. Hawkes. A continuous 4D motion model from multiple respiratory cycles for use in lung radiotherapy. *Med Phys*, 33(9):3348–3358, Sep 2006.

K. Murphy, B. van Ginneken, J. P. W. Pluim, S. Klein, and M. Staring. Semi-automatic reference standard construction for quantitative evaluation of lung CT registration. *Med Image Comput Comput Assist Interv*, 11(Pt 2):1006–1013, 2008.

J. Nijkamp, S. Rit, J.-J. Sonke, and M. van Herk. Utilization of 4D-CT and contrast enhanced expiration breath-hold CT for 3D treatment planning of lung tumors. In *XVIth International Conference on the Use of Computers in Radiation Therapy*, Amsterdam, June 2010.

K. Ø. Noe, B. D. D. Senneville, U. V. Elstrøm, K. Tanderup, and T. S. Sørensen. Acceleration and validation of optical flow based deformable registration for image-guided radiotherapy. *Acta Oncol*, 47(7):1286–1293, 2008.

G. P. Penney, J. Weese, J. A. Little, P. Desmedt, D. L. Hill, and D. J. Hawkes. A comparison of similarity measures for use in 2-D-3-D medical image registration. *IEEE Trans Med Imaging*, 17(4):586–595, Aug 1998.

C. Plathow, S. Ley, C. Fink, M. Puderbach, W. Hosch, A. Schmhl, J. Debus, and H.-U. Kauczor. Analysis of intrathoracic tumor mobility during whole breathing cycle by dynamic MRI. *Int J Radiat Oncol Biol Phys*, 59(4):952–959, Jul 2004.

E. Rietzel and G. T. Y. Chen. Deformable registration of 4D computed tomography data. *Med Phys*, 33(11):4423–4430, Nov 2006.

E. Rietzel, T. Pan, and G. T. Y. Chen. Four-dimensional computed tomography: image formation and clinical protocol. *Med Phys*, 32(4):874–889, Apr 2005.

S. Rit, D. Sarrut, and L. Desbat. Comparison of analytic and algebraic methods for motion-compensated cone-beam CT reconstruction of the thorax. *IEEE Trans Med Imaging*, Feb 2009.

S. Rit, M. van Herk, L. Zijp, and J.-J. Sonke. Quantification and impact of the variability of the respiratory motion during radiotherapy. *Submitted to Int J Radiat Oncol Biol Phys*, 2010.

T. Rohlfing, C. R. Maurer, D. A. Bluemke, and M. A. Jacobs. Volume-preserving nonrigid registration of MR breast images using free-form deformation with an incompressibility constraint. *IEEE Trans Med Imaging*, 22(6):730–741, Jun 2003.

D. Ruan, J. A. Fessler, J. M. Balter, and J.-J. Sonke. Exploring breathing pattern irregularity with projection-based method. *Med Phys*, 33(7):2491–2499, Jul 2006.

H. Ruppertshofen, S. Kabus, and B. Fischer. Image registration using tensor grids for lung ventilation studies. In *Bildverarbeitung fr die Medizin 2009*, 2009.

H. Ruppertshofen, S. Kabus, and B. Fischer. Tensor grid based image registration with application to ventilation estimation on 4D CT lung data. *Int J Comput Assist Radiol Surg*, Apr 2010.

D. Sarrut. Deformable registration for image-guided radiation therapy. *Zeitschrift fr Medizinische Physik*, 16:285–297, 2006.

D. Sarrut, V. Boldea, S. Miguet, and C. Ginestet. Simulation of four-dimensional CT images from deformable registration between inhale and exhale breath-hold CT scans. *Med Phys*, 33(3):605–617, Mar 2006.

D. Sarrut, B. Delhay, P.-F. Villard, V. Boldea, M. Beuve, and P. Clarysse. A comparison framework for breathing motion estimation methods from 4-D imaging. *IEEE Trans Med Imaging*, 26(12):1636–1648, Dec 2007.

A. Schmidt-Richberg, J. Ehrhardt, R. Werner, and H. Handels. Slipping objects in image registration: improved motion field estimation with direction-dependent regularization. *Med Image Comput Comput Assist Interv*, 12(Pt 1):755–762, 2009a.

A. Schmidt-Richberg, J. Ehrhardt, R. Werner, and H. Handels. Evaluation and comparison of force terms for the estimation of lung motion by non-linear registration of 4D-CT image data. In *World Congress on Medical Physics and Biomedical Engineering*, volume 12, pages 2128– 2131, Munich, Germany, September 2009b.

Y. Seppenwoolde, H. Shirato, K. Kitamura, S. Shimizu, M. van Herk, J. V. Lebesque, and K. Miyasaka. Precise and real-time measurement of 3D tumor motion in lung due to breathing and heartbeat, measured during radiotherapy. *Int J Radiat Oncol Biol Phys*, 53(4):822–834, Jul 2002.

J.-J. Sonke, J. Lebesque, and M. van Herk. Variability of four-dimensional computed tomography patient models. *Int J Radiat Oncol Biol Phys*, 70(2): 590–598, Feb 2008.

J. A. Sorenson, L. T. Niklason, and J. A. Nelson. Photographic unsharp masking in chest radiography. *Invest Radiol*, 16(4):281–288, 1981.

M. Staring, S. Klein, and J. P. W. Pluim. A rigidity penalty term for nonrigid registration. *Med Phys*, 34(11):4098–4108, Nov 2007.

F.-C. Su, C. Shi, P. Mavroidis, V. Goytia, R. Crownover, P. Rassiah-Szegedi, and N. Papanikolaou. Assessing four-dimensional radiotherapy planning and respiratory motion-induced dose difference based on biologically effective uniform dose. *Technol Cancer Res Treat*, 8(3):187–200, Jun 2009a.

F.-C. Su, C. Shi, P. Mavroidis, P. Rassiah-Szegedi, and N. Papanikolaou. Evaluation on lung cancer patients' adaptive planning of tomotherapy utilising radiobiological measures and planned adaptive module. *J Radiother Pract*, 8: 185–194, Jan 2009b.

C. Tanner, J. A. Schnabel, A. Degenhard, A. D. Castellano-Smith, C. Hayes, M. O. Leach, D. R. Hose, D. L. G. Hill, and D. J. Hawkes. Validation of volume-preserving non-rigid registration: Application to contrast-enhanced mr-mammography. In *MICCAI (1)*, pages 307–314, 2002.

C. Vaman, D. Staub, J. Williamson, and M. Murphy. A method to estimate 4DCT deformable registration errors via principal components analysis. In *Medical Physics suppl*, volume 36 of *6*, pages 2821–2821. AAPM, 2009.

J. Vandemeulebroucke, D. Sarrut, and P. Clarysse. The POPI-model, a point-validated pixel-based breathing thorax model. In *XVth International Conference on the Use of Computers in Radiation Therapy, ICCR*, 2007.

J. Vandemeulebroucke, P. Clarysse, J. Kybic, and D. Sarrut. Estimating respiratory motion from cone-beam projections. In , *Proceedings of the First International Workshop on Pulmonary Image Analysis of the MICCAI Conference*, pages 83–92, MorrisVille, USA, September 2008. Lulu.com.

T. Vercauteren, X. Pennec, A. Perchant, and N. Ayache. Non-parametric diffeomorphic image registration with the demons algorithm. *Med Image Comput Comput Assist Interv*, 10(Pt 2):319–326, 2007.

P.-F. Villard, M. Beuve, B. Shariat, V. Baudet, and F. Jaillet. Simulation of lung behaviour with finite elements: Influence of bio-mechanical parameters. In *Proceedings of the Third International Conference on Medical Information VisualisationBiomedical Visualisation, MediVis*, page 914, 2005.

G. Wahba. Spline models for observational data. *Soc. Industr. Applied Math.*, 59, 1990.

J. Weese, G. P. Penney, P. Desmedt, T. M. Buzug, D. L. Hill, and D. J. Hawkes. Voxel-based 2-d/3-d registration of fluoroscopy images and ct scans for image-guided surgery. *IEEE Trans Inf Technol Biomed*, 1(4):284–293, Dec 1997.

R. Werner, J. Ehrhardt, R. Schmidt, and H. Handels. Patient-specific finite element modeling of respiratory lung motion using 4D CT image data. *Med Phys*, 36(5):1500–1511, May 2009a.

R. Werner, J. Ehrhardt, A. Schmidt-Richberg, and H. Handels. Validation and comparison of a biophysical modeling approach and non- linear registration for estimation of lung motion fields in thoracic 4D CT data. In *Proceedings of SPIE- The International Society for Optical Engineering*, volume 7259, Februari 2009b.

J. W. Wolthaus, J.-J. Sonke, M. van Herk, J. S. Belderbos, M. M. Rossi, J. V. Lebesque, and E. M. Damen. Comparison of different strategies to use four-dimensional computed tomography in treatment planning for lung cancer patients. *Int J Radiat Oncol Biol Phys*, Volume 70(Issue 4, 15):Pages 1229–1238, March 2008a.

J. W. H. Wolthaus, J. J. Sonke, M. van Herk, and E. M. F. Damen. Reconstruction of a time-averaged midposition CT scan for radiotherapy planning of lung cancer patients using deformable registration. *Med Phys*, 35(9):3998–4011, Sep 2008b.

J. Wu, M. Kim, J. Peters, H. Chung, and S. S. Samant. Evaluation of similarity measures for use in the intensity-based rigid 2D-3D registration for patient positioning in radiotherapy. *Medical Physics*, 36(12):5391–5403, 2009.

Z. Wu, E. Rietzel, V. Boldea, D. Sarrut, and G. C. Sharp. Evaluation of deformable registration of patient lung 4DCT with subanatomical region segmentations. *Med Phys*, 35(2):775–781, Feb 2008.

T. Yamamoto, S. Kabus, J. von Berg, T. Klinder, T. Blaffert, C. Lorenz, and P. Keall. Physiological validation of 4D-CT-Based ventilation imaging in patients with chronic obstructive pulmonary disease (COPD). In *Medical Physics suppl*, volume 36 of *6*, pages 2821–2821. AAPM, 2009.

D. Yang, W. Lu, D. A. Low, J. O. Deasy, A. J. Hope, and I. E. Naqa. 4D-CT motion estimation using deformable image registration and 5D respiratory motion modeling. *Med Phys*, 35(10):4577–4590, Oct 2008.

Y. Yin, E. A. Hoffman, and C.-L. Lin. Mass preserving nonrigid registration of CT lung images using cubic B-spline. *Med Phys*, 36(9):4213–4222, Sep 2009.

Q. Zhang, A. Pevsner, A. Hertanto, Y.-C. Hu, K. E. Rosenzweig, C. C. Ling, and G. S. Mageras. A patient-specific respiratory model of anatomical motion for radiation treatment planning. *Med Phys*, 34(12):4772–4781, Dec 2007.

H. Zhong, T. Peters, and J. V. Siebers. FEM-based evaluation of deformable image registration for radiation therapy. *Phys Med Biol*, 52(16):4721–4738, Aug 2007.

H. Zhong, J. Kim, and I. J. Chetty. Analysis of deformable image registration accuracy using computational modeling. *Med Phys*, 37(3):970–979, Mar 2010.

Relevant Publications by the Author

Book Chapter

D. Sarrut, J. Vandemeulebroucke and S. Rit. Intensity-based deformable registration for radiation therapy: introduction and overview. Jan Ehrhardt and Christian Lorenz (ed.) *To appear in 4D Motion Modeling and Estimation*, 2011.

Articles in International Journals

D. Sarrut and J. Vandemeulebroucke. B-LUT: Fast and low memory B-spline image interpolation. *Comput Methods Programs Biomed*, 2010, 99, 172-178.

J. Vandemeulebroucke, S. Rit, J. Kybic, P. Clarysse, and D. Sarrut. Spatio-temporal motion estimation for respiratory-correlated imaging of the lungs. *Med Phys*, 2011, 38(1), 166-178.

J. Vandemeulebroucke, O. Bernard, S. Rit, J. Kybic, P. Clarysse, and D. Sarrut. Automated Segmentation of a Motion Mask to Preserve Sliding Motion in Deformable Registration of Thoracic CT. *To be submitted*, 2011.

Articles in International Conferences with Review Commitee

J. Vandemeulebroucke, D. Sarrut, and P. Clarysse. The POPI-model, a point-validated pixel-based breathing thorax model. In *XVth International Conference on the Use of Computers in Radiation Therapy, ICCR*, 2007.

J. Vandemeulebroucke, P. Clarysse, J. Kybic, and D. Sarrut. Estimating respiratory motion from cone-beam projections. In *Proceedings of the First International Workshop on Pulmonary Image Analysis of the MICCAI Conference*, pages 83–92, MorrisVille, USA, September 2008. Lulu.com.

J. Vandemeulebroucke, J. Kybic, P. Clarysse, and D. Sarrut. Respiratory motion estimation from cone-beam projections using a prior model. In *Med Image Comput Comput Assist Interv*, 12(Pt 2):365–372, 2009.

L. Grezes-Besset, J. Vandemeulebroucke, P. Clarysse, and D. Sarrut. Respiratory motion tracking from different viewing angles during lung cancer treatment in radiotherapy. In *IEEE Nuclear Science Symposium and Medical Imaging Conference*, 2009.

J. Vandemeulebroucke, O. Bernard, J. Kybic, P. Clarysse, and D. Sarrut. Automatic motion mask extraction for deformable registration of the lungs. In *XVIth International Conference on the Use of Computers in Radiation Therapy*, Amsterdam, June 2010.

J. Vandemeulebroucke, S. Rit, J. Schaerer and D. Sarrut. Deformable image registration with automated motion-mask extraction. In *Medical Image Analysis for the Clinic: A Grand Challenge 2010 of the MICCAI Conference*, Beijing, September 2010.

Abstracts in International Conferences

M. Ayadi, J. Vandemeulebroucke, S. Hlavacek, V. Boldea, C. Ginestet, and D. Sarrut. Dosimetry on moving organs: static and dynamic dose distributions computed from 4DCT for lung cancer treatment. In *9th Biennial ESTRO Meeting on Physics and Radiation Technology For Clinical Radiotherapy*, volume 84, page S77, 2007.

J. Vandemeulebroucke, J. Kybic, P. Clarysse, and D. Sarrut. Estimating breathing motion from cone-beam projections using a prior patient model. In *10th Biennial ESTRO Meeting on Physics and Radiation Technology For Clinical Radiotherapy*, 92, page S185. Elsevier, 2009.

S. Rit, J. Vandemeulebroucke, D. Sarrut, and J.-J. Sonke. B-spline parametrization of the temporal dimension for respiratory motion estimation. In *Proceedings of the 29th Annual ESTRO Meeting*, Barcelona, Spain, 2010.

Articles in French Conferences with Review Commitee

L. Grezes-Besset, J. Vandemeulebroucke, P. Clarysse, and D. Sarrut. Extraction du signal respiratoire au cours d'un traitement par radiothérapie du cancer du poumon. In *La recherche en imagerie et technologie de la santé*, 2009.

Jef Vandemeulebroucke was born in Vilvoorde, Belgium, on 18 July 1981. He studied electronic engineering at the university of Ghent, Belgium, during which he pursued a master in artificial intelligence at the university of Granada, Spain, in 2003. His master thesis, in collaboration with the Erasmus MC in Rotterdam, the Netherlands, was on medical image registration. He graduated with honours in 2005. The following year he performed a post-graduate training course on numerical optimization methods at the university of Florianópolis in Brazil.

Jef joined the Creatis laboratory in Lyon, France, in November 2006 after obtaining an EU Marie-Curie PhD Fellowship in the WARTHE project. During his doctorate he was mainly based at the Léon Bérard Cancer Center in Lyon, though the program also included a stay of 8 months at the Center for Machine Perception in Prague, Czech Republic in 2008. He defended his PhD before the INSA of Lyon in July 2010.